Statics and Dynamics of Mechanical Lattices

Green, Steven

Award date:
2009

Awarding institution:
University of Bath

Statics and Dynamics of Mechanical Lattices

submitted by

Steven Christopher Green

for the degree of Doctor of Philosophy

of the

University of Bath

Department of Mathematical Sciences

June 2009

Abstract

This thesis contributes to the understanding of one dimensional mechanical lattice structures. Structures formed from freely pin jointed rigid links with either vertical or torsional springs at the pivots, or both, are studied under the influence of an axial load. These studies fall into three parts: static behaviour of a 'simple' mechanical system with only vertical springs, dynamic behaviour of this 'simple' system, and static behaviour of a compound mechanical lattice with both vertical and torsional springs.

The first part uses ideas from the field of discrete mechanics to derive several discrete boundary value problems that model the static equilibrium states of the 'simple' mechanical lattice. This application of discrete mechanics allows us to better understand the relationships between the mechanical system and the discrete boundary value problem used to model it. The resulting discrete boundary value problem is studied in detail and interesting complex behaviour is observed.

The study of the dynamic behaviour of the 'simple' mechanical lattice concentrates on the existence and stability of time periodic spatially localised solutions called discrete breathers. Discrete breathers are found to exist and to be stable. Also, related solutions called phonobreathers are found to exist and, although the exact phonobreather solutions are unstable, interesting nonlinear dynamic behaviour is observed close to the unstable solutions.

Finally, the static behaviour of a new compound mechanical lattice, a discrete version of the strut on a linear foundation, is studied in Chapter 6. We see how the behaviour of two simpler mechanical lattices is manifested in this compound lattice, before presenting analytic and numerical results on the primary, static, bifurcations of this compound lattice. The localised behaviour of the most physically relevant static equilibrium states is also investigated. Extensions to the discrete boundary value problem methods of the earlier chapters are also discussed.

Contents

Chapter 1

Introduction

Materials and structures which have regions of high stiffness and regions of low stiffness often exhibit remarkably complex behaviour when subjected to forces of compression. A crumpling piece of paper, for example, has creases leading to regions of high stiffness and flat planes which are relatively bendy. The final crumpled shape of the paper, and its pattern of creases, is extremely complicated. Similarly, proteins which consist of chains of amino acids, some with high stiffness bonds and others with lower stiffness bonds, fold into very complex structures as they buckle and fold under the intra-protein molecular forces. Complex behaviour has also been observed, by Domokos & Holmes (1993), in the discrete mechanical system of Figure 1.1 (a) which consists of an axially loaded chain of rigid links connected by low stiffness friction free pivots. The continuous relative of this mechanical system is the linear elastica or Euler strut, the relatively simple behaviour of which was determined, essentially completely, by Euler. Whilst the static behaviour of Euler's strut was determined by one of the new topics of mathematical research at the time, elliptic integrals, the complex structure observed in the mechanical lattice of Figure 1.1 (a) is determined by the relatively new mathematical area of chaos theory for area preserving iterated maps.

The observation of a complex set of static equilibrium states in mechanical lattice (a) of Figure 1.1 motivates the study of mechanical lattices (b) and (c) (Figure 1.1) in this thesis. Lattice (b) consists of an axially loaded chain of freely pivoted rigid links supported by vertical, linearly elastic springs that slide horizontally at their top end to stay vertical. This system's static equilibrium equations are a set of second order difference equations and so in this thesis this system is referred to as the second order mechanical system. Lattice (c) consists of lattice (b) with the addition of the rotational springs seen in lattice (a); the equilibrium equations for this lattice are a set of fourth

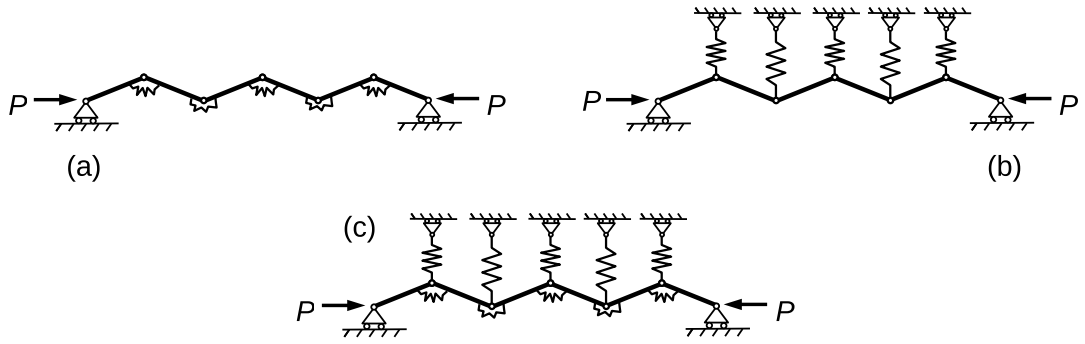

Figure 1.1: *Mechanical lattices (b) and (c) are the subjects of this thesis, (a) has been previously studied in detail by Domokos & Holmes (1993). These three lattices are composed of N freely pin jointed rigid links and are loaded axially by the load P. The springs are all linear and the nonlinearities arise purely through the geometry of the systems.*

order difference equations and so this lattice is termed the fourth order mechanical system. Neglecting the behaviour at the ends of the lattice for the time being, and taking only the small displacement approximation to the behaviour of lattice (c), these difference equations are given by

$$(a)\;\; 0 = (\theta_{n+1} - 2\theta_n + \theta_{n-1}) + p\sin\theta_n \tag{1.1}$$

$$(b)\;\; 0 = \frac{p}{4}\left(\frac{U_{n+1}-U_n}{\sqrt{1-(U_{n+1}-U_n)^2}} - \frac{U_n - U_{n-1}}{\sqrt{1-(U_n-U_{n-1})^2}}\right) + U_n \tag{1.2}$$

$$(c)\;\; 0 = (U_{n+2} - 4U_{n+1} + 6U_n - 4U_{n-1} + U_{n-2}) + p(U_{n+1} - 2U_n + U_{n-1}) + k_f U_n, \tag{1.3}$$

where θ_n is the angle the nth link makes with the horizontal, U_n is the vertical displacement of the nth pivot, p is the nondimensional load applied to the systems and k_f is the nondimensional foundation spring stiffness in lattice (c). The previous study of lattice (a), by Domokos & Holmes (1993), rewrites the second order difference equation (1.1) as two first order equations, thus defining a map $\phi\colon \mathbb{R}^2 \to \mathbb{R}^2$. Iterating this map ϕ defines a discrete initial value problem and the equilibrium states of the mechanical lattice can be found by using this to define a discrete boundary value problem.

In a mechanical lattice with a finite number of links there are two types of behaviour for the vertical displacements of the pivots at each end of the lattice. These pivots can be either vertically free or vertically fixed. Previous work has either not considered the boundaries (Hunt et al. (1997)) or picked one specific type of boundary behaviour (Domokos & Holmes (1993), Kocsis & Kaárolyi (2006)). Also, in previous work (Domokos & Holmes (1993)) it was noticed that there is a certain amount of

choice in choosing the specific iterated map used to determine the static equilibrium states of the mechanical lattice. Thus the first topic considered in this thesis, in Section 3.1, is a general method for modelling these mechanical systems using iterated maps. This work uses results from numerical analysis (Marsden & West (2001)) to better understand the relation between the lattices' boundary constraints and the iterated maps used to determine the static equilibrium states of these systems. These more general results are then applied to the specific mechanical lattice system, studied first by Thompson & Hunt (1973), shown in Figure 1.1 (b). This mechanical lattice has previously shown glimpses of the complex static behaviour observed in lattice (a) of Figure 1.1 (Hunt et al. (1997)), and indeed in Chapter 4 we see that a multitude of static equilibrium states exist.

With such rich behaviour shown by the static equilibrium states of mechanical system (b) of Figure 1.1 we expect the dynamic behaviour to be equally interesting and we are not disappointed. Modelling the dynamic behaviour of lattice (b) using a first order approximation to the time dependence leads to the set of ordinary differential equations (ODEs)

$$\ddot{U}_n = -U_n - \frac{p}{4}\left(\frac{U_{n+1}-U_n}{\sqrt{1-(U_{n+1}-U_n)^2}} - \frac{U_n-U_{n-1}}{\sqrt{1-(U_n-U_{n-1})^2}}\right).$$

This thesis searches for, and finds, discrete breathers and phonobreathers in this set of ODEs. Discrete breathers, discovered by Sievers & Takeno (1988), are exact, time periodic solutions to nonlinear lattice differential equations with (usually exponential) spatial localisation. Since their discovery, a large amount of research (the recent review by Flach & Gorbach (2008) has 412 references) has been performed into their behaviour both mathematical and, more recently, experimental. Despite this volume of literature very little attention has been paid to their existence in macroscopic mechanical systems. This is surprising since localisation of oscillation in systems such as turbine blades can lead to excessive fatigue and premature failure; clearly important behaviour to understand. Thus in Chapter 5 we search for and find linearly stable breather solutions in this mechanical lattice. There also exist exact time periodic solutions, phonobreathers, which look like a breather solution superimposed on a background that oscillates sinusoidally in both space and time, and similarly these have seen little attention in the context of macroscopic mechanical systems. The nonlinear dynamics close to exact breather and phonobreather solutions is an ongoing topic of research and the last part of Chapter 5 presents some interesting nonlinear dynamic behaviour close to the trajectory of an exact but unstable phonobreather solution.

The start, in this thesis, of the analysis of the static behaviour of mechanical lattice (c) of Figure 1.1 is motivated, partly, by the wealth of interesting mathematical behaviour that has been observed in the spatially continuous cousins of this mechanical lattice. One example of such a continuous mechanical lattice is the strut on a nonlinear foundation. This model is a small displacement approximation to the Euler strut sandwiched between two supporting foundations with nonlinear material behaviour. This leads to the following nonlinear fourth order differential equation for the vertical displacement of the strut u as a function of the horizontal spatial variable x (equivalently arc length in the small displacement approximation)

$$u'''' + pu'' + f(u) = 0, \tag{1.4}$$

where f is a nonlinear function of its argument such as $f(u) = u - u^2 + bu^3$, p is the nondimensional applied load and b is a parameter of the nonlinearity. (We can already see the similarity between this and (1.3).) There has been much analysis performed on this equation and its variants that has given insight into the mathematical behaviour of the Hamiltonian-Hopf bifurcation and homoclinic snaking (e.g. see the work of Champneys & Toland (1993), Woods & Champneys (1999), Hunt et al. (2000)). A related model, that has seen less analysis due to the complexity of the mathematical formulation, is the nonlinear strut on the linear foundation (Hunt et al. (1993)). This model retains the nonlinearity due to the geometry of large material displacements while keeping the foundation linear. The resulting differential equation that gives the vertical displacement of the strut u as a function of the arc length along the strut x is

$$u'''' + \frac{u'''u''u'}{1-u'^2} + \frac{u''^3(1+3u'^2)}{(1-u'^2)^2} + p\frac{u''}{\sqrt{1-u'^2}} + ku(1-u'^2) = 0, \tag{1.5}$$

where p is the nondimensional applied load and k is the foundation stiffness. The discrete mechanical system of Figure 1.1 (c) has not been previously studied and is a discrete version of this nonlinear strut on a linear foundation model.

The two discrete models shown in Figure 1.1 (a) and (b) are simpler limits of the compound fourth order mechanical system, and understanding their behaviour and how it relates to the more complex system is an important first step in understanding the more complex model. It has been suggested that fourth order mechanical models similar to the one in Figure 1.1 (c) model the buckling of force chains in granular media (Hunt et al. (2009), Tordesillas & Muthuswamy (2009)). Thus to start a search for new and interesting behaviour in this discrete mechanical system and to motivate further work on the link between granular media and buckling of discrete mechanical systems

in Chapter 6 we begin to see how the complex behaviour of the two, now well studied, simpler limits of this system persists in the more complex lattice. Also, we note some interesting behaviour of this mechanical lattice which is not inherited from the two simpler systems.

1.1 Thesis structure

Chapter 1: This chapter gives a brief overview of the thesis, its motivations and the original contributions it makes to the literature.

Chapter 2: The relation of this thesis to research that has gone before is laid out in detail in Chapter 2. After a description of how the mechanical lattices of Figure 1.1 relate to other physical and mathematical lattices in the literature, existing knowledge about the three mechanical lattices shown in Figure 1.1 is summarised. Also discussed is the relation of the work in Chapter 4 to the numerical analysis literature on spurious solutions to discretised boundary value problems and the applicability of existing breather and phonobreather existence proofs to mechanical lattice (b) of Figure 1.1.

Chapter 3: The first half of this chapter generalises the idea that the static equilibrium states of mechanical lattices can be found by solving a discrete boundary value problem (discrete BVP). This generalisation considers the effect that choosing fixed or free end constraints has on the discrete BVP that models the lattice by using the theory of discrete mechanics (Marsden & West (2001)). The second half of this chapter introduces the mathematical model used to analyse the statics and dynamics of mechanical system (b) in Figure 1.1.

Chapter 4: This chapter applies the general results of Chapter 3 to mechanical system (b) of Figure 1.1. The bifurcation structure, branch behaviour and symmetry properties of the solutions to the resulting discrete boundary value problem are studied in detail. The continuum limit of this discrete BVP is also studied and the behaviour compared to that of the discrete BVP.

Chapter 5: Some aspects of the dynamic behaviour of the lattice (b) of Figure 1.1 are considered herein. Specifically, the stability of the static equilibrium states found in Chapter 4 under controlled (or dead) loading conditions is investigated numerically, before it is demonstrated that linearly stable breather solutions can exist in this mechanical lattice. Finally, some phonobreather solutions are located

in this lattice and interesting nonlinear dynamics close to one of these unstable phonobreather solutions is presented.

Chapter 6: This chapter studies aspects of the static equilibrium behaviour of lattice (c) of Figure 1.1, which requires a more general mathematical formulation than that of Chapter 4. The formulation introduced in this chapter allows the links to attain angles with the left-to-right horizontal line of greater than $\pi/2$. The consequences of this generalisation for the two limits of this system, $k_f = 0$ giving lattice (a) of Figure 1.1, and $k_b = 0$ giving lattice (b) of Figure 1.1, is considered. This chapter finishes with a description of some behaviour of the static equilibrium states of this more complex lattice that is seen in neither of the simpler mechanical systems.

Chapter 7: This brief chapter summarises the work of this thesis.

1.2 Main contributions

The first part of Chapter 3 of this thesis contributes to the understanding of how the static equilibrium states of general lattices with potential energies of the form

$$V(Q_0, \ldots, Q_N) = h \sum_{n=0}^{N} v(Q_n) + h \sum_{n=0}^{N-1} w\left(\frac{Q_{n+1} - Q_n}{h}\right), \tag{1.6}$$

where h is a parameter of the system and v & w are real functions of a real variable, can be determined using a discrete boundary value problem. This work uses the ideas of discrete mechanics and variational integration (Marsden & West (2001)) to see, more clearly, the relation between lattices with the above form and the map that forms the discrete boundary value problem. Work is also presented that allows free or fixed boundary constraints to be applied to either end of the lattice whilst retaining the ability to model the lattice's equilibrium states using a discrete BVP.

Chapter 4 applies the general results derived in Chapter 3 to mechanical system (b) of Figure 1.1. This extends the work of Hunt et al. (1997) to analyse, in detail, the full bifurcation diagram for the static equilibrium states of this mechanical system.

Chapter 5, after an investigation of the dynamic stability of the static equilibrium states found in Chapter 4, presents the first numerical observation of stable breather solutions in a purely macroscopic mechanical lattice system (mechanical lattice (b) of Figure 1.1). This is followed by the observation of new and interesting nonlinear

dynamic behaviour about an, exact, unstable phonobreather solution. This behaviour consists of the slow growth of the disturbed phonobreather core, gradually enveloping the spatially and temporally oscillatory background.

Chapter 6 brings together the behaviour of the two simpler mechanical systems, shown in Figure 1.1 (a) and (b), to start an analysis into the more complex mechanical system of Figure 1.1 (c). This mechanical lattice has not been studied before and provides a good context for discussing possible extensions to the discrete boundary value problem methods of Chapter 3. This chapter also presents analytic and numerical results that demonstrate how the behaviour of this lattice is different to that of the simpler lattices (a) and (b) of Figure 1.1. These results have helped to motivate further study into the link between fourth order mechanical lattices and force chain buckling in granular media.

Chapter 2

Background

2.1 Lattices

According to Brillouin (1946), Newton (1687) was the first person to investigate a one dimensional lattice structure. Newton used the, now popular, one dimensional mass-spring lattice, shown in Figure 2.1, to derive a formula for the velocity of sound. More recently, since the discovery of atomic lattices the mass-spring model shown in Figure 2.1 has been used as a simple model of a one dimensional atomic lattice, or crystal. The standard mathematical formulation of this mass-spring chain is to write it as a Hamiltonian dynamical system with Hamiltonian

$$H(\boldsymbol{P},\boldsymbol{Q}) = \sum_n \frac{P_n^2}{2m} + \sum_n v(Q_n) + \sum_n w(Q_{n+1} - Q_n) \tag{2.1}$$

where v & w are real functions of a real variable and the variables P_n are the momenta conjugate to the displacements Q_n. As shown in Figure 2.1 the variables Q_n measure the displacement of each mass from its equilibrium position. The specific form of the functions v and w leads to a diverse range of behaviour and analysis techniques. Several

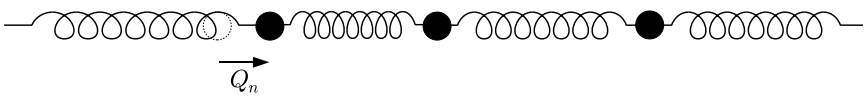

Figure 2.1: *Standard mass and spring lattice, first used by Newton to model sound propagation through air, more recently used as a basic model of a one dimensional chain of atoms.*

examples of the functions v and w that give well known lattices, and the names we shall give these choices in this thesis, are:

$$\text{Fermi-Pasta-Ulam (FPU) lattice:} \quad v(x) = 0 \qquad w(x) = x^2/2 + \alpha x^3/3 + \beta x^4/4,$$

where $\beta = 0$ gives the α-FPU model and $\alpha = 0$ gives the β-FPU model,

$$\begin{aligned} \text{Klein Gordon (KG) lattice:} \quad & v(x) = \sum_{n=2}^{\infty} a_n x^n \qquad w(x) = cx^2/2 \\ \text{Toda lattice:} \quad & v(x) = 0 \qquad w(x) = ce^{-bx} + ax \\ \text{Frenkel–Kontorova lattice:} \quad & v(x) = 1 - \cos(x) \quad w(x) = c(x-d)^2. \end{aligned}$$

For comparison, mechanical system (b) of Figure 1.1 has the form

$$v(x) = x^2 \qquad w(x) = \frac{p}{4}\sqrt{1-x^2}. \tag{2.2}$$

In the above, the coefficients a_n in the KG lattice are the coefficients in the Taylor expansion of an arbitrary function v, whilst a, b, c, d and p are parameters of the lattices. We can see that the mechanical lattice studied in detail in Chapters 3–5 ((b) of Figure 1.1) shares features with the FPU lattice, in that the coupling function w is nonlinear, but also shares some common ground with the Klein Gordon class of lattices in that there is an on-site potential v. Also, the Taylor expansions of mechanical system (b) and the Frenkel–Kontorova lattice model agree to $\mathcal{O}(x^2)$, however, the nonlinearities do differ.

In the literature little consideration has been given to the static behaviour of the above lattices as they are primarily studied for their dynamic behaviour[1]. The FPU lattice became famous through one of the first computer simulations of a nonlinear lattice performed by Fermi et al. (1955). This experiment sought to demonstrate that energy in a nonlinear lattice will eventually equidistribute throughout the linear modes of the lattice, but quite the opposite was observed; after a certain time period all the energy returned to the initially excited mode. The explanation for this behaviour is still an active area of research and the observation of breathers in the FPU lattice (e.g. Marin & Aubry (1996)) has helped explain this phenomenon. The very first mathematical proof of the existence of breathers in a nonlinear lattice applied to the Klein Gordon lattice shown above. The above lattices have been studied, primarily, for

[1]The static equilibrium states of the Frenkel–Kontorova lattice coincide with those of mechanical system (a) of Figure 1.1 and so have been determined, in detail, by Domokos & Holmes (1993).

their interesting dynamic behaviour; in the next section we discuss previous research on the mechanical lattices of Figure 1.1 which have, until now, been studied primarily for their interesting static behaviour.

2.2 Discrete mechanical systems

The literature on the mechanical systems of Figure 1.1 is not large and we believe that this is the first study of the more complex system (c). Mechanical systems (a) (with three links) and (b) (with N links) first appeared in the book by Thompson & Hunt (1973), where the linear primary buckling bifurcations were determined and the stability of the postbuckling branches found in the case of system (a) with three links. System (b) (the system studied in Chapter 4) was further studied in Hunt et al. (1997) where the problem of finding the static equilibrium states of the indefinitely sized lattice was reduced to studying the iterates of an area preserving map. This map was studied as an initial value problem (IVP) and was found to exhibit chaotic behaviour. Specifically, this chaotic behaviour was found to be due to a homoclinic tangle that exists in the iterates of the map for pre-buckling loads. The work of Chapter 4 of this thesis extends the results of Hunt et al. (1997) to consider the entire global bifurcation diagram for these static equilibrium states formulated as an N link boundary value problem.

The Mechanical lattice (a) of Figure 1.1 has seen study in several different contexts. It is a natural extension to the realm of discrete mechanical systems of the classical Euler strut, and several different end constraint and load situations have been studied. Kocsis & Kaárolyi (2006) studied a clamped left boundary and free and generally loaded right boundary and, as with lattice (b), it was seen that the resulting static equilibrium states could be found using an iterated area preserving map. The limitations of this iterated map as a numerical approximation to the continuum model was studied by Beyn & Lorenz (1982) (see also Section 2.3 below). The main work done on this lattice was performed by Domokos & Holmes (1993) and is summarised later in this section.

In this thesis fixed and zero constraints on the end of the lattice have been chosen to match with the previous work of Thompson & Hunt (1973), Domokos & Holmes (1993) and the many continuum buckling studies mentioned in the introduction. For future work it is an interesting point to note that Rink (2003) proves that for systems with certain discrete symmetries (which these lattices have) the static and dynamic behaviour of the fixed and zero boundary lattice with N links is embedded in an invariant manifold of the same system with $2N$ links and periodic boundary conditions.

This is useful as periodic boundary conditions occasionally simplify the analysis of these systems.

The two mechanical systems (a) and (b) of Figure 1.1 are simpler limits of the more complex system (c). If the vertical foundation springs of system (c) are removed we arrive at system (a) which is termed the $k_f = 0$ limit. Removing the torsional springs that add bending stiffness to the pivots of system (c) leads to system (b), termed the $k_b = 0$ limit. Because of this, and the interest in comparing the behaviour of the two simpler systems (a) and (b), some behaviour of lattice (a) from the work of Domokos & Holmes (1993) is now presented.

The energy of system (b) of Figure 1.1 can be written in terms of the angles θ and the non-dimensional load p by subtracting the work done by the load from the energy stored in the springs, giving

$$E = \sum_{n=2}^{N} \frac{1}{2}(\theta_n - \theta_{n-1})^2 + p \sum_{n=1}^{N} \cos\theta_n.$$

The condition for the lattice to be in static equilibrium is that this energy is stationary with respect to variations in the θ variables. This condition, $\partial E/\partial\theta_i = 0$ for $i = 1, \ldots, N$, leads to the equilibrium equations

$$\begin{aligned} 0 &= -(\theta_2 - \theta_1) - p\sin\theta_1 && \text{(2.3a)} \\ 0 &= -(\theta_{n+1} - 2\theta_n + \theta_{n-1}) - p\sin\theta_n && \text{(2.3b)} \\ 0 &= (\theta_N - \theta_{N-1}) - p\sin\theta_N, && \text{(2.3c)} \end{aligned}$$

for $n = 2, \ldots, N-1$. In Domokos & Holmes (1993) these equilibrium equations are solved by assuming that $\sum_{i=1}^{N} \cos\theta_i \neq 0$, and writing the second order difference equation (2.3b) as two first order difference equations to define a map $\phi : \mathbb{R}^2 \to \mathbb{R}^2$. The reason for this assumption and an investigation of the solutions to equations (2.3) that do not satisfy it is presented in Section 6.2.1 of Chapter 6. Once this map ϕ has been derived it is then used to define a discrete boundary value problem, the solutions to which are exactly the solutions to (2.3) above. This formulation allows many properties of the solutions to these equations to be proved and a slightly generalised (see Chapter 3) version of this method is used in Chapter 4 of this thesis to investigate mechanical system (b) of Figure 1.1.

An example of the bifurcation diagram, which plots each static equilibrium state for structure (a) of Figure 1.1 as a dot in parameter-state space, is shown in Figure 2.2. The left pane of Figure 2.2 shows the parameter-state space in terms of the load p and

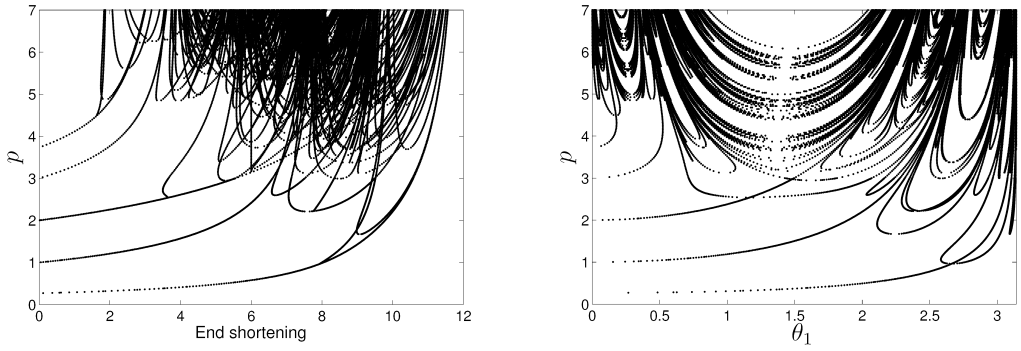

Figure 2.2: *This shows the bifurcation diagrams for system (a) of Figure 1.1 with torsional springs only and six links ($N = 6$). On the left we see how the non-dimensional load varies with the overall end-shortening of the system, whilst the right plot shows how the solutions, uniquely represented by the nondimensional load p and the angle of link one, bifurcate. This system was studied in detail in Domokos & Holmes (1993).*

the end shortening of the solution, whilst the right pane of Figure 2.2 shows the load p and the angle of the first link θ_1. The end shortening $\mathcal{E}$ of a static equilibrium state in this lattice is defined as

$$\mathcal{E} = N - \sum_{n=1}^{N} \cos\theta_n$$

and the angle of the first link θ_1 and the nondimensional load p uniquely represent the solutions to (2.3). To understand these bifurcation diagrams consider first the unloaded ($p = 0$) flat equilibrium state ($\theta_1 = 0$ and end shortening $= 0$). As the load is increased from zero we see that several, in fact $N - 1$, branches of non-zero equilibrium states intersect with the zero solution at $\theta_1 = 0$. These intersections, or bifurcations, occur at the at the p values

$$p_k = 2\left(1 - \cos\frac{k\pi}{N}\right) \quad \text{for} \quad k = 1, \ldots, N-1,$$

and the non-zero solutions on these non-zero branches can be represented by sinusoidal shapes given by

$$U_n^{(k)} = \epsilon \sin\frac{kn\pi}{N} \quad \text{for} \quad n = 1, \ldots, N,$$

where $U_n^{(k)}$ is the vertical displacement of the nth pivot. An example of such a solution is shown in the top pane of Figure 2.3. This expression, along with the loads p_k above, tells us that the branch that bifurcates at the lowest load has the longest spatial wavelength. We can also see, in Figure 2.2, that all of the branches can support a load that increases as we move along the branch, indicating a positive post buckling

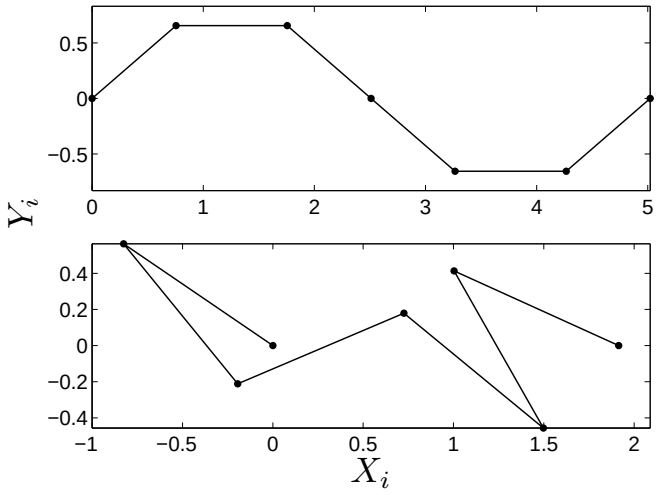

Figure 2.3: *Examples of a regular sinusoidal equilibrium state in lattice (a) of Figure 1.1 (top) and a less regular chaotic equilibrium state (bottom). The parameter values for these states are: top,* $p \approx 1.09$*,* $\theta_1 \approx 0.71$ *and end shortening* ≈ 0.98*; bottom,* $p \approx 6.09$*,* $\theta_1 \approx 2.54$ *and end shortening* ≈ 4.09*. The coordinates* Y_i *and* X_i *are given by* $Y_i = U_i = \sum_{n=1}^{i} \sin\theta_n$ *and* $X_i = \sum_{n=1}^{i} \cos\theta_n$ *for* $i = 1, \ldots, N$ *and* $Y_0 = X_0 = 0$*.*

stiffness. As the end shortening increases on the primary branches the behaviour is regular for a while, but eventually further bifurcations occur leading to an explosion of branches of irregular solutions. Some these branches are connected to the primary branches and some are not. An example of one of these irregular solutions is given in the bottom pane of Figure 2.3.

2.3 Numerical integration

Physically, if we imagine taking system (a) of Figure 1.1 and increasing the number of links whilst keeping the overall length of the system (and spring energy per unit length) constant we might expect that at some point the system will start to behave like the continuous Euler strut. From a mathematical point of view we expect the mathematical model for the discrete system, a discrete boundary value problem, to approach the differential equation modelling the continuous system in some mathematical sense. This mathematical sense is that of numerical integrators for ordinary differential equations; the map that defines the discrete BVP modelling the discrete mechanical system is also a numerical integrator for the differential equation modelling the Euler strut. In Section 3.1 we see that this relation holds for more general discrete lattice systems

before Chapter 4 discusses another specific example, that of system (b) of Figure 1.1.

This realisation, that some numerical integrators actually model the equilibrium states of certain mechanical systems, is interesting because it gives physical motivation to the idea of studying these integrators away from their 'useful' limit. People have been studying numerical integrators with large step-size for many years with a view to avoiding the spurious solutions that appear. Papers such as those of Beyn & Lorenz (1982), Peitgen et al. (1981), Allgower (1975), Reinhall et al. (1989) are some of the first to study numerical integrators for large step sizes and it is found that much of the behaviour of these different systems is qualitatively similar to the behaviour analysed in Chapter 4 also seen in Figure 2.2. As the step size (equivalently the nondimensional load p) is increased more and more 'spurious' solutions appear either bifurcating from branches that exist in the continuum limit and or appearing at fold bifurcations on branches that appear to originate in the bifurcation diagram 'at infinity'. These phenomena are generally caused by the same phenomenon, the onset of chaos in the underlying map.

2.3.1 Discrete Mechanics

Using classical continuum mechanics, one can determine the equations of motion for a system, where the dependent variable or 'time' is continuous, from a functional of the time dependent state variables called the action (or Hamilton's first principle function). Discrete mechanics, on the other hand, allows one to derive discrete equations of motion for a system where time is discrete. It might not be immediately obvious how the structures in Figure 1.1 lead to a dynamical system where 'time' is discrete, but the idea described by Hunt et al. (1989) is to let the spatial variable that evolves along the length of the structure take the role of 'time'. We can see now, in the case of the mechanical systems of Figure 1.1, how the dependent variable, now a spatial variable, is discrete. Each step in the dependent variable corresponds to moving one link down (or up) the mechanical chain. As background to Section 3.1 the analogy between continuum classical mechanics and discrete mechanics (Marsden & West (2001)) is now briefly presented.

One of the main axioms in classical (continuum) mechanics is Hamilton's principle of least action (Arnold (1980), Feynman et al. (1963)). This states that if we form the function $\mathcal{L}(\boldsymbol{q}, \dot{\boldsymbol{q}})$ (where $\boldsymbol{q} = (q^{(1)}, \ldots, q^{(N-1)})^{\mathrm{T}}$) from the difference of the kinetic energy of the system $T(\boldsymbol{q}, \dot{\boldsymbol{q}})$ and potential energy $V(\boldsymbol{q}, \dot{\boldsymbol{q}})$ the system follows paths in

the space of the generalised coordinates $(\boldsymbol{q}, \dot{\boldsymbol{q}})$ such that the action functional

$$\mathcal{S} = \int_{t_1}^{t_2} \mathcal{L}(\boldsymbol{q}(t), \dot{\boldsymbol{q}}(t))\, \mathrm{d}t$$

is stationary. The condition of stationary action leads directly to the Euler-Lagrange equations for this Lagrangian

$$\frac{\mathrm{d}}{\mathrm{d}t}\left(\frac{\partial \mathcal{L}}{\partial \dot{\boldsymbol{q}}}\right) = \frac{\partial \mathcal{L}}{\partial \boldsymbol{q}} \tag{2.4}$$

with the boundary conditions

$$\boldsymbol{q}(t_1) = \boldsymbol{q_1} \quad \text{or} \quad \left.\frac{\partial \mathcal{L}}{\partial \dot{\boldsymbol{q}}}\right|_{t=t_1} = 0 \quad \text{and} \quad \boldsymbol{q}(t_2) = \boldsymbol{q_2} \quad \text{or} \quad \left.\frac{\partial \mathcal{L}}{\partial \dot{\boldsymbol{q}}}\right|_{t=t_2} = 0.$$

Additionally, if the Lagrangian $\mathcal{L}(\boldsymbol{q}, \dot{\boldsymbol{q}})$ does not depend explicitly on time t we can find a conserved function of the motion, the Hamiltonian function,

$$H(\boldsymbol{p}, \boldsymbol{q}) = \boldsymbol{p} \cdot \dot{\boldsymbol{q}} - \mathcal{L}(\boldsymbol{q}, \dot{\boldsymbol{q}})$$

where $\boldsymbol{p} = \mathrm{d}\mathcal{L}/\mathrm{d}\dot{\boldsymbol{q}}$ such that the equations of motion, Hamilton's equations, are given by

$$\dot{\boldsymbol{q}} = \frac{\partial H}{\partial \boldsymbol{p}} \quad \text{and} \quad \dot{\boldsymbol{p}} = -\frac{\partial H}{\partial \boldsymbol{q}}.$$

An important property of these equations is that the time T flow map

$$\phi(\boldsymbol{p}(t), \boldsymbol{q}(t), T) \colon (\boldsymbol{p}(t), \boldsymbol{q}(t)) \to (\boldsymbol{p}(t+T), \boldsymbol{q}(t+T))$$

they define is symplectic, or area preserving if $\boldsymbol{p}(t), \boldsymbol{q}(t) \in \mathbb{R}$. This means that the matrix

$$\Psi = \begin{pmatrix} \frac{\partial \boldsymbol{q}(t+T)}{\partial \boldsymbol{q}(t)} & \frac{\partial \boldsymbol{q}(t+T)}{\partial \boldsymbol{p}(t)} \\ \frac{\partial \boldsymbol{p}(t+T)}{\partial \boldsymbol{q}(t)} & \frac{\partial \boldsymbol{p}(t+T)}{\partial \boldsymbol{p}(t)} \end{pmatrix}$$

satisfies $\Psi^{\mathrm{T}} J \Psi = J$ where J is the Poisson matrix given by

$$J = \begin{pmatrix} 0 & I_n \\ -I_n & 0 \end{pmatrix}$$

and I_n is the n dimensional identity matrix.

Discrete mechanics (see for example Marsden & West (2001)) is the theory analogous

to the above for systems where time is discrete. Thus the action becomes

$$\mathcal{S}_d = \sum_{n=0}^{N} L_d(\boldsymbol{Q_n}, \boldsymbol{Q_{n+1}}), \tag{2.5}$$

where $\boldsymbol{Q_n} = (Q_n^{(1)}, \ldots, Q_n^{(N)})^{\mathrm{T}}$ and the discrete Euler-Lagrange equations corresponding to the Lagrangian L_d are

$$\frac{\mathrm{d}}{\mathrm{d}\boldsymbol{Q_n}}\big(L_d(\boldsymbol{Q_{n-1}}, \boldsymbol{Q_n}) + L_d(\boldsymbol{Q_n}, \boldsymbol{Q_{n+1}})\big) = 0$$

with the boundary conditions

$$\boldsymbol{Q}_0 = \boldsymbol{q_0} \quad \text{or} \quad \frac{\mathrm{d}}{\mathrm{d}\boldsymbol{Q_0}} L_d(\boldsymbol{Q}_0, \boldsymbol{Q}_1) = 0 \quad \text{and} \quad \boldsymbol{Q}_N = \boldsymbol{q_N} \quad \text{or} \quad \frac{\mathrm{d}}{\mathrm{d}\boldsymbol{Q_N}} L_d(\boldsymbol{Q}_{N-1}, \boldsymbol{Q}_N) = 0.$$

If the discrete Lagrangian is non-degenerate, i.e. the matrix A given by

$$[A]_{ij} = \frac{\mathrm{d}^2 L_d(\boldsymbol{Q_n}, \boldsymbol{Q_{n+1}})}{\mathrm{d}Q_n^{(i)}\,\mathrm{d}Q_{n+1}^{(j)}}$$

satisfies $\det(A) \neq 0$, then it is a Lagrangian generating function for the symplectic map $\phi\colon (\boldsymbol{P_n}, \boldsymbol{Q_n}) \to (\boldsymbol{P_{n+1}}, \boldsymbol{Q_{n+1}})$ defined implicitly by

$$\begin{aligned} \boldsymbol{P_n} &= -\frac{\mathrm{d}}{\mathrm{d}\boldsymbol{Q_n}} L_d(\boldsymbol{Q_n}, \boldsymbol{Q_{n+1}}) \\ \boldsymbol{P_{n+1}} &= \frac{\mathrm{d}}{\mathrm{d}\boldsymbol{Q_{n+1}}} L_d(\boldsymbol{Q_n}, \boldsymbol{Q_{n+1}}). \end{aligned}$$

These are the ideas that are used in Section 3.1 to model the different end constraints that one might want to impose on a general lattice equation when studying its static equilibrium states. Specifically, we write the potential for the mechanical system in the form (2.5) and then use the above theory to derive the corresponding discrete BVP. This is an improvement over previous ad-hoc methods of deriving maps and discrete BVPs to model discrete mechanical systems as it has allowed us to model all types of lattice end constraints, and also allows any freedom in the choice of map ϕ to be removed in such a way that ϕ shares as many symmetries with the whole mechanical system as possible.

2.4 Dynamics: breathers and phonobreathers

Discrete breathers are time periodic and spatially localised solutions to the equations of motion for coupled, lattice ODEs. Solutions such as these were first observed in complex variable ODEs such as the discrete self trapping equation (equivalently the discrete nonlinear Schrödinger equation, DNLS) by Scott & Macneil (1983), Eilbeck et al. (1984, 1985), Carr & Eilbeck (1985).[2] Their existance in a real valued ODE system was subsequently predicted by Sievers & Takeno (1988) in the context of crystal lattices and the first mathematical proof their of existence in Hamiltonian lattices was by MacKay & Aubry (1994). Since this early work there has been a huge amount of mathematical, and more recently experimental, work in determining their properties. To get an idea of the amount of work in this area the recent review of Flach & Gorbach (2008) contains over 400 references, other reviews include those of Flach & Willis (1998), Aubry (1997, 2006). Despite this large volume of work nearly all of the applications have been in microscopic systems from physics such as nonlinear optical waveguides, antiferromagnetic layered structures, and driven micromechanical cantilever arrays to name a few listed in Flach & Gorbach (2008). This lack of work on breathers in macroscopic systems is, however, not due to the non-existence of breathers on these scales as Russell et al. (1997) have located moving breathers experimentally and numerically in a chain of magnetic pendulums. Consequently, the concerns of Section 5.3 of this thesis are the existence and stability of discrete breathers in the structural mechanical lattice (b) of Figure 1.1.

At around the time that interest in discrete breathers was burgeoning time periodic solutions called phonobreathers, which appear to be a superposition of a nonlinear phonon with a breather solution, were discovered by Marin & Aubry (1996) in lattices with nonlinear on-site terms. Since then there has been little interest in these specific solutions and only more recently have they been investigated further (Morgante et al. (2002)). In Chapter 5 we demonstrate further that the mechanical lattice (with coupling nonlinearity only) can also support phonobreather solutions. Moreover, we demonstrate that the nonlinear dynamics close to a phonobreather solution is sufficiently recurrent to enable the experimental observation of this behaviour. This recurrent behaviour takes the form of a slowly growing phonobreather core that expands at a constant velocity slowly enveloping the nonlinear phonon tails.

Discrete breathers and phonobreathers have been found numerically in lattices of both

[2] See also Eilbeck & Johansson (2003) for a review of time periodic and spatially localised solutions in the DNLS equation.

the FPU and KG types (Marin & Aubry (1996)). There are also rigorous proofs of the existence of breather solutions in quite general lattice equations. These proofs fall into two broad categories, the first (such as that of MacKay & Aubry (1994)) relies on the existence of an anticontinuous limit of the dynamical equations. This is a limit of one of the parameters such that the system becomes a set of decoupled *nonlinear* oscillators, a trivial breather is then created in this limit: one oscillator oscillating whilst the others are stationary. The persistence of the breather into the small coupling regime is then proved, using the implicit function theorem or a variant thereof. The other category is the proof of existence of breathers whose frequency is close to the edge of the linear spectrum of small oscillations (e.g. James (2003), Aubry et al. (2001)). None of these proofs apply directly to the system with Hamiltonian (2.1) and potentials (2.2) due to the lack of a suitable anticontinuous limit, the mixed type of the lattice between the FPU and KG lattices and the fact that the coupling potential $w(x) = \sqrt{1-x^2}$ is of the softening type (i.e. $w''(x) < 0$ for all x). Thus in Chapter 5 we resort to numerical methods (specifically that of Marin & Aubry (1996) explained in detail in Section 5.3) to demonstrate the existence of breathers and phonobreathers.

2.5 Numerical path following: Auto

Many problems in applied mathematics, and several problems in this thesis, lead to looking, numerically, for solutions to a problem of the form $\boldsymbol{F}(\boldsymbol{X}, \boldsymbol{\lambda}) = \boldsymbol{0}$, where $\boldsymbol{F} : \mathbb{R}^N \times \mathbb{R}^k \to \mathbb{R}^N$, $\boldsymbol{X} \in \mathbb{R}^N$ is the solution to the problem, and $\boldsymbol{\lambda} \in \mathbb{R}^k$ is some set of parameters on which the solution depends. Often the most appropriate and efficient way of finding a solution to $\boldsymbol{F}(\boldsymbol{X}; \boldsymbol{\lambda}) = 0$ is highly problem dependent and several different methods are used in this thesis. However, once a particular solution has been found there do exist general methods to find other solutions nearby. One of these methods, first proposed by Keller (1977), is called pseudo-arc-length continuation. This method relies on the implicit function theorem to tell us that if we have a solution to $\boldsymbol{F}(\boldsymbol{X}; \boldsymbol{\lambda}) = 0$ given by $\boldsymbol{X}^*, \boldsymbol{\lambda}^*$ then as long as the matrix $\partial \boldsymbol{F}(\boldsymbol{X}; \boldsymbol{\lambda})/\partial \boldsymbol{X}$ is non-singular we can write our solution $\boldsymbol{X}^*$ as a continuous function of $\boldsymbol{\lambda}$ for $\boldsymbol{\lambda}$ near $\boldsymbol{\lambda^*}$ i.e. $\boldsymbol{X} = \boldsymbol{X}(\boldsymbol{\lambda})$. This application of the implicit function theorem also tells us that Newton's iterative method for finding solutions to $\boldsymbol{F}(\boldsymbol{X}; \boldsymbol{\lambda}^*) = 0$ will converge quadratically to the solution $\boldsymbol{X}^*$ as long as we start this iterative procedure close enough to the solution. In fact for systems where N is large and F is fairly complex the phrase 'close enough' should be interpreted as 'very close indeed'. One freely available computer code for performing arc length continuation is the code Auto Doedel et al. (1997).

This code has the advantages that it is reasonably efficient, has many options for computing specific information about solutions along the solution branches in various different application areas, and has a fair knowledge of how to cope with singular points where $\partial \boldsymbol{F}(\boldsymbol{X};\boldsymbol{\lambda})/\partial \boldsymbol{X}$ is singular. This allows, amongst other things, the computation of Floquet characteristic multipliers (see Section 5.3.3) for time periodic solutions to ODEs and automatic branch switching and fold detection for systems of algebraic equations. This briefly introduces the method referred in this thesis as numerical continuation, or just simply continuation.

Chapter 3

Modelling

Previously, the derivation of an iterated map and discrete boundary value problem from the condition that a mechanical system be in static equilibrium has been limited to specific mechanical systems and specific boundary behaviour. There are two possible types of behaviour for the vertical displacements at each end of the mechanical lattice: free (unconstrained) or fixed (constrained), and previous work has not considered these different possibilities or the impact they have on the subsequently derived iterated map. Section 3.1 of this chapter presents new results that rectify this for a general lattice with nearest neighbour coupling. This is done using methods from numerical analysis, discussed in detail in the paper '*Discrete Mechanics and Variational Integrators*' (Marsden & West (2001)), which, in addition to clarifying the above boundary issues and clarifying where the choices in deriving the iterated maps arise, gives a clear link between the discrete boundary value problem (discrete BVP) and its continuum limit.

The second section of this chapter, Section 3.2, introduces a mathematical model of mechanical system (b) in Figure 1.1 (also shown in Figure 3.1). This model is used in chapters 4 and 5 to study the static and dynamic behaviour of the mechanical system. The approximations made to the dynamic behaviour in deriving the model and the nondimensionalisations used in the remainder of this thesis are also presented.

3.1 Discrete mechanics

The potential energy for a general (mechanical) lattice with $N+1$ lattice sites (N links) and nearest neighbour coupling can be written as

$$V(Q_0, \ldots, Q_N) = h \sum_{n=0}^{N} v(Q_n) + h \sum_{n=0}^{N-1} w\left(\frac{Q_{n+1} - Q_n}{h}\right) \tag{3.1}$$

where $h \neq 0$ is a parameter of the system and, for reasons that will become clear later, we require $w''(x) \neq 0$ for all x in the domain of w. If we interpret this expression in terms of the standard mass-spring model of an atomic chain shown in Figure 2.1, the derivative of the function v gives the restoring force each mass feels towards its equilibrium position in the absence of any coupling springs, while the derivative of the function w gives the force displacement behaviour of the springs that couple neighbouring masses. For these reasons we call the function v the on-site potential and the function w the coupling potential. This general form includes the mechanical systems (a) and (b) of Figure 1.1, and in the case of mechanical system (b) the function v' gives the force-displacement behaviour of the vertical springs whilst the function w' is related to the work done by the external load in shortening the system.

When modelling the physical lattice we have to decide on the most appropriate behaviour for the coordinates at the ends of the lattice. For instance, when modelling the behaviour of a bridge, where the main structure is attached to solid rock at either end, fixed boundaries are appropriate (i.e. Q_0, Q_N fixed). Whereas for other examples, such as the modelling of a building crushed from above, a fixed lower boundary with a free upper boundary might be more appropriate. Here we show the new result that it is possible to model all four (fixed-fixed, free-fixed, fixed-free and free-free) combinations of end lattice behaviour using a discrete boundary value problem.

The main idea we make use of in doing this is the following theorem which takes the appropriate ideas from discrete mechanics (see Marsden & West (2001)) and shows how to derive a discrete boundary value problem from a suitable potential function. In the following theorem we use the following abbreviated notation for the evaluation

of the derivative of a function at a point,

$$\mathrm{D}_1 L_d(Q_n, Q_{n+1}) = \left.\frac{\partial L_d(a,b)}{\partial a}\right|_{\substack{a=Q_n \\ b=Q_{n+1}}}$$

$$\text{similarly,} \quad \mathrm{D}_2 L_d(Q_n, Q_{n+1}) = \left.\frac{\partial L_d(a,b)}{\partial b}\right|_{\substack{a=Q_n \\ b=Q_{n+1}}} . \quad (3.2)$$

Theorem 3.1. *Let the function $L_d\colon \mathbb{R}^2 \to \mathbb{R}$ satisfy*

$$\frac{\mathrm{d}^2 L_d(Q_n, Q_{n+1})}{\mathrm{d}Q_n \, \mathrm{d}Q_{n+1}} \neq 0. \quad (3.3)$$

The vector $\boldsymbol{Q} = (Q_0, \ldots, Q_N)$ is a stationary point of the function $S\colon \mathbb{R}^{N+1} \to \mathbb{R}$,

$$S(\boldsymbol{Q}) = \sum_{n=0}^{N-1} L_d(Q_n, Q_{n+1}), \quad (3.4)$$

so that $\partial S/\partial Q_n = 0$ for all n, subject to one of the following sets of constraints

① $Q_0 = \alpha_0$, $Q_N = \alpha_N$
② $Q_0 = \alpha_0$
③ $Q_N = \alpha_N$
④ *None,*

if the coordinates Q_n, $n = 0, \ldots, N$ satisfy the following discrete boundary value problem:

$$\boldsymbol{X}_n = \begin{pmatrix} Q_n \\ P_n \end{pmatrix}, \quad \boldsymbol{X}_{n+1} = \phi(\boldsymbol{X}_n) \quad n = 0, \ldots, N-1,$$

with the boundary conditions corresponding to the constraints ①–④ above given by

① $Q_0 = \alpha_0$, $Q_N = \alpha_N$
② $Q_0 = \alpha_0$, $P_N = 0$
③ $P_0 = 0$, $Q_N = \alpha_N$
④ $P_0 = 0$, $P_N = 0$.

Here, α_0 and α_N are fixed constants and $\phi : (Q_n, P_n)^{\mathrm{T}} \to (Q_{n+1}, P_{n+1})^{\mathrm{T}}$ is defined implicitly by

$$\begin{aligned} P_n &= -\mathrm{D}_1 L_d(Q_n, Q_{n+1}) \\ P_{n+1} &= \mathrm{D}_2 L_d(Q_n, Q_{n+1}). \end{aligned}$$

Proof. Consider the variation of the function S with respect to the variables Q_n

$$\begin{aligned}\delta S &= \sum_{i=0}^{N-1} \mathrm{D}_1 L_d(Q_i, Q_{i+1})\delta Q_i + \sum_{i=0}^{N-1} \mathrm{D}_2 L_d(Q_i, Q_{i+1})\delta Q_{i+1} + \mathcal{O}(\delta Q_n^2) \\ &= \sum_{i=1}^{N-1} \big(\mathrm{D}_1 L_d(Q_i, Q_{i+1}) + \mathrm{D}_2 L_d(Q_{i-1}, Q_i)\big)\delta Q_i \\ &\quad + \mathrm{D}_1 L_d(Q_0, Q_1)\delta Q_0 + \mathrm{D}_2 L_d(Q_{N-1}, Q_N)\delta Q_N + \mathcal{O}(\delta Q_n^2).\end{aligned}$$

We can see from this that if

$$\mathrm{D}_1 L_d(Q_i, Q_{i+1}) + \mathrm{D}_2 L_d(Q_{i-1}, Q_i) = 0 \text{ for } i = 1, \ldots, N-1 \tag{3.5}$$

$$\text{and} \qquad \mathrm{D}_1 L_d(Q_0, Q_1) = 0 \quad \text{or} \quad \delta Q_0 = 0 \tag{3.6}$$

$$\text{and} \qquad \mathrm{D}_2 L_d(Q_{N-1}, Q_N) = 0 \quad \text{or} \quad \delta Q_N = 0 \tag{3.7}$$

then to lowest order $\delta S = 0$ and $\partial S/\partial Q_n = 0$ for all n. The equations (3.5) are called the discrete Euler-Lagrange equations and, in this case, are a set of second order difference equations. Equations (3.6) and (3.7) are the boundary conditions for this set of difference equations. We now convert this set of second order difference equations into a set of coupled first order difference equations and with the appropriate boundary conditions these define the required discrete BVP. If we define

$$P_i \equiv \begin{cases} -\mathrm{D}_1 L_d(Q_i, Q_{i+1}) & \text{for } i = 0, \ldots, N-1 \\ \mathrm{D}_2 L_d(Q_{N-1}, Q_N) & \text{for } i = N \end{cases} \tag{3.8}$$

then the discrete Euler-Lagrange equations (3.5) and the second statement of (3.8) give

$$P_{i+1} = \mathrm{D}_2 L_d(Q_i, Q_{i+1}) \text{ for } i = 0, \ldots, N-1. \tag{3.9}$$

In terms of the new P_i variables, boundary condition (3.6) becomes $P_0 = 0$ or $Q_0 = \alpha_0$ and (3.7) becomes $P_N = 0$ or $Q_N = \alpha_N$ for some fixed constants α_0 and α_N.

The required boundary value problem is defined by letting $\boldsymbol{X}_i = (Q_i, P_i)^{\mathrm{T}}$ for $i = 0, \ldots, N$ and noting that (3.8) and (3.9) implicitly define the map $\phi : (Q_i, P_i)^{\mathrm{T}} \to (Q_{i+1}, P_{i+1})^{\mathrm{T}}$ for $i = 1, \ldots, N-1$. The condition (3.3) ensures via the implicit function theorem that (3.8), for $i = 1, \ldots, N-1$, can be solved to give Q_{i+1} as a function of P_i and Q_i. □

In order to find the discrete BVP that gives the stationary points of the potential (3.1) we attempt to write the potential in the form (3.4). In doing this we have a

certain amount of choice: do we include $v(Q_{i+1})$ as part of $L_d(Q_i, Q_{i+1})$ or $v(Q_i)$? We postpone this choice by introducing an extra parameter, $\beta \in [0, 1]$, thus

$$V(Q_0, \ldots, Q_N) = \sum_{n=0}^{N-1} L_d^\beta(Q_i, Q_{i+1}) + h\beta v(Q_0) + h(1-\beta)v(Q_N)$$

with

$$L_d^\beta(Q_i, Q_{i+1}, h) = h\beta v(Q_{i+1}) + h(1-\beta)v(Q_i) + hw\left(\frac{Q_{i+1}-Q_i}{h}\right). \tag{3.10}$$

As it is, the stationary points of V will not coincide identically with those of (3.4), but by choosing $\beta = 1$ and fixing Q_0 they will. Similarly, choosing $\beta = 0$ and fixing Q_N causes the stationary points of the functions V and (3.4) to be identical. Hence, with these conditions, the stationary points of V can be found using the discrete BVP of Lemma 3.1 with boundary conditions ② or ③ respectively. Also, if we fix both Q_0 and Q_N the discrete BVP of Lemma 3.1 with boundary conditions ① will give the stationary points of V with no restriction on the value of β. The one remaining combination of lattice end behaviour is that of unconstrained values of Q_0 and Q_N. However, as things stand,with no constraints on either Q_0 or Q_N, we cannot get the stationary points of V and (3.4) to coincide. To model these unconstrained boundary conditions we have to introduce an extra coordinate and consider an extended discrete BVP. Before we do this, we present a Lemma we will need later that shows that if a particular, extended potential function is stationary then so too is the original, unextended potential.

Lemma 3.1. *Let* $\bar{V}(Q_0, \ldots, Q_{N+1}) = V(Q_0, \ldots, Q_N) + hw\left(\frac{Q_{N+1}-Q_N}{h}\right)$ *for* $h \neq 0$, *then*

$$\frac{\partial \bar{V}}{\partial Q_i} = 0 \quad \textit{for} \quad i = 0, \ldots, N+1 \quad \textit{implies} \quad \frac{\partial V}{\partial Q_n} = 0 \quad \textit{for} \quad n = 0, \ldots, N.$$

Proof. Clearly

$$\frac{\partial \bar{V}}{\partial Q_i} = 0 \text{ implies } \frac{\partial V}{\partial Q_i} = 0 \text{ for } i = 0, \ldots, N-1.$$

Now consider the coordinates Q_N and Q_{N+1}; we have

$$\frac{\partial \bar{V}}{\partial Q_N} = \frac{\partial V}{\partial Q_N} - w'\left(\frac{Q_{N+1}-Q_N}{h}\right), \tag{3.11}$$

and so

$$\frac{\partial \bar{V}}{\partial Q_{N+1}} = 0 \quad \Rightarrow \quad w'\left(\frac{Q_{N+1}-Q_N}{h}\right) = 0$$

which along with (3.11) implies $\frac{\partial V}{\partial Q_N} = 0$.

□

Remark 3.1. *It is also the case that if* $\bar{V}(Q_{-1},\ldots,Q_N) = V(Q_0,\ldots,Q_N)+hw\left(\frac{Q_0-Q_{-1}}{h}\right)$ *then*

$$\frac{\partial \bar{V}}{\partial Q_i} = 0 \text{ for } i = -1,\ldots,N \text{ implies } \frac{\partial V}{\partial Q_n} = 0 \text{ for } n = 0,\ldots,N.$$

The extra coordinate required to extend the discrete BVP can be introduced at the start of the lattice or at the end. The following two extended potential functions correspond to these two different possibilities:

$$\begin{aligned}
\bar{V}_1(Q_{-1},\ldots,Q_N) &= V(Q_0,\ldots,Q_N) + hw\left(\frac{Q_0-Q_{-1}}{h}\right) \\
&= \sum_{i=-1}^{N-1} L_d^\beta(Q_i,Q_{i+1}) - h(1-\beta)v(Q_{-1}) + h(1-\beta)v(Q_N)
\end{aligned}$$

and

$$\begin{aligned}
\bar{V}_2(Q_0,\ldots,Q_{N+1}) &= V(Q_0,\ldots,Q_N) + hw\left(\frac{Q_{N+1}-Q_N}{h}\right) \\
&= \sum_{n=0}^{N} L_d^\beta(Q_i,Q_{i+1}) + h\beta v(Q_0) - h\beta v(Q_{N+1}).
\end{aligned}$$

Lemma 3.1 now tells us that with $\beta = 1$ we can find the equilibrium states of the unconstrained mechanical system using $\bar{V}_1$ and the discrete BVP this defines via Theorem 3.1 with boundary conditions ④. Similarly, setting $\beta = 0$ gives the unconstrained equilibrium states via the extended potential $\bar{V}_2$. We must, however, remember that when using $\bar{V}_1$ the final $N+1$ coordinates correspond to the original coordinates where as with $\bar{V}_2$ it is the first $N+1$ coordinates. It is important to note here that if we evaluate P_{-1} and P_N using (3.8) for the general discrete Lagrangian we are discussing (3.10) we get

$$P_{-1} = -h(1-\beta)v'(Q_{-1}) - w'\left(\frac{Q_0-Q_{-1}}{h}\right) \tag{3.12}$$

$$P_{N+1} = h\beta v'(Q_{N+1}) + w'\left(\frac{Q_{N+1}-Q_N}{h}\right). \tag{3.13}$$

Setting $\beta = 0$ in (3.13) means that one of boundary conditions ④ of Theorem (3.1), specifically $P_{N+1} = 0$, implies that $w'\left(\frac{Q_{N+1}-Q_N}{h}\right) = 0$ and so the converse of Lemma

3.1 holds for the extended potential function $\bar{V}_2$. This means that stationary points of $V(Q_0, \ldots, Q_N)$ are also stationary points of $\bar{V}_2(Q_0, \ldots, Q_{N+1})$. The same holds for the other extended potential function above, $\bar{V}_1$: setting $\beta = 1$ means that $P_{-1} = 0$ implies $w'\left(\frac{Q_0 - Q_{-1}}{h}\right) = 0$.

Of course, since the two different discrete BVPs found above are modelling the same system we expect their solutions to be identical. The next section studies some properties of the map ϕ^β, the map ϕ from Theorem 3.1 derived from the discrete Lagrangian $L_d^\beta(Q_i, Q_{i+1})$, and we see that there is a special relationship between the maps ϕ^β and $\phi^{1-\beta}$ which ensures that these two discrete BVPs do have the same solutions.

3.1.1 Map properties

When writing down the discrete Lagrangian (3.10) there was a certain amount of choice which was postponed by including the parameter β. It then transpired that the lattice end constraints we wanted to model affected the permitted values of β. In the following discussion of the properties of the map ϕ^β we will see the special relationship between the maps ϕ^β and $\phi^{(1-\beta)}$ mentioned in the previous section. The short derivations of these properties below will also show the usefulness of the variational derivation of the discrete BVP. This should be contrasted with the longer calculations of the next subsection that look at the explicit form of the map ϕ^β and classify it in terms of the numerical integration algorithms that exist in the literature.

To recap, the map ϕ^β is the map derived via Theorem 3.1 from the discrete Lagrangian $L_d^\beta(Q_i, Q_{i+1})$ of equation (3.10). The discrete Lagrangian $L_d^\beta(Q_i, Q_{i+1})$ is, in turn, derived from the potential with general form (3.1). In the following we need to indicate the dependence of ϕ^β on the parameter h in the potential and so we write ϕ_h^β to indicate this dependence. In the following list of properties of ϕ_h^β the bracketed references refer to the appropriate page or theorem of Marsden & West (2001).

- The map ϕ is symplectic, i.e. $\psi^T J \psi = J$ where $J = \begin{pmatrix} 0 & 1 \\ -1 & 0 \end{pmatrix}$ and $\psi = \frac{\partial \phi}{\partial \boldsymbol{X}}$.

  The map ϕ is the discrete Hamiltonian flow map derived from L_d^β and so is symplectic (p. 386).

- The maps ϕ^β and $\phi^{1-\beta}$ for $\beta \in [0, 1]$ are adjoint maps: $\phi_{-h}^{1-\beta} \circ \phi_h^\beta = \text{i.d.}$, and so for $\beta = 1/2$ ϕ_h^β is self adjoint. This is a result of the following property of the discrete Lagrangian (3.10): $L_d^\beta(Q_i, Q_{i+1}, h) = -L_d^{1-\beta}(Q_{i+1}, Q_i, -h)$ (p. 403 Theorem 2.4.1).

- The map ϕ_h^β is a numerical integrator, with step size h, of the differential equation with Lagrangian $L(q, \dot{q}) = v(q) + w(\dot{q})$. (Example 2.3.2 p. 402) This relationship is discussed further in the next section.

These relations show that for the class of lattice systems with potential (3.1) the static equilibrium states may be found through the use of a symplectic mapping with a well defined continuum limit. This is a discrete version of the 'dynamical phase space analogy' proposed by Hunt et al. (1989) where by spatial boundary value problems derived from continuous structural situations are analysed by first considering the phase space behaviour of the related initial value problem.

We also see that in the case where one of the boundaries is fixed these boundary conditions affect the choice of β which in turn affects the symmetry properties of ϕ_h^β. If we fix the lower (upper) boundary we are forced to choose $\beta = 1$ ($\beta = 0$) which means that the adjoint symmetry between ϕ_h^β and $\phi_h^{(1-\beta)}$ is a representation of the physical reflectional symmetry relating these two different boundary conditions. If we consider a system where both boundaries are fixed we find that we are able to chose $\beta = 1/2$, the self adjoint property of the map ϕ_h^β for $\beta = 1/2$ then reflects the global reflection symmetry of the mechanical system and boundary conditions at the 'local' level of an individual link.

3.1.2 A link to the continuum problem

The methods of discrete mechanics used in the previous sections allow the definition of a well defined continuum limit for the discrete mechanical system. After first presenting explicit expressions for the map ϕ and the continuum limit just mentioned we see here exactly what type of numerical integrator the map ϕ is.

The discrete Lagrangian L_d^β (3.10) is an approximation to an integral

$$L_d^\beta(Q_n, Q_{n+1}, h) = \int_{t_n}^{t_{n+1}} v(q) + w(\dot{q})\, \mathrm{d}t + \mathcal{O}(h^{r+1})$$

where $q(t_n) = Q_n$, $q(t_{n+1}) = Q_{n+1}$ and $r = 1$ for $\beta \neq 1/2$ and $r = 2$ for $\beta = 1/2$. This integral is the Lagrangian generating function for the flow of the dynamical system with Lagrangian

$$\mathcal{L}(q, \dot{q}) = v(q) + w(\dot{q}). \tag{3.14}$$

Section 2.3 from Marsden & West (2001) then tells us that for small h the map ϕ_h^β, defined implicitly in Lemma (3.1), and given explicitly by $\phi_h^\beta \colon (Q_n, P_n)^{\mathrm{T}} \to (Q_{n+1}, P_{n+1})^{\mathrm{T}}$

thus [1]

$$Q_{n+1} = Q_n + h(w')^{-1}\big(p_n + h(1-\beta)v'(Q_n)\big) \tag{3.15a}$$
$$P_{n+1} = P_n + h\beta v'(Q_{n+1}) + h(1-\beta)v'(Q_n) \tag{3.15b}$$

is a symplectic, order r numerical integrator. This numerical integrator approximates the time h flow map of the differential equation

$$w''(\dot{q})\ddot{q} = v'(q). \tag{3.16}$$

which is the Euler-Lagrange equation of the Lagrangian (3.14). We also note at this point that this is a Hamiltonian differential equation with Hamiltonian

$$H(p,q) = p(w')^{-1}(p) - w\left((w')^{-1}(p)\right) - v'(q)$$

giving Hamilton's equations

$$\dot{q} = \frac{\partial H}{\partial p} = (w')^{-1}(p) \quad \dot{p} = -\frac{\partial H}{\partial q} = v'(q).$$

The above expressions enable us to name the specific type of numerical integrator that the map ϕ_h^β represents. The symplectic Euler numerical integrator and its adjoint result from taking $\beta = 1$ and $\beta = 0$ respectively (Hairer et al. 2002, p3,43) whilst taking $\beta = 1/2$ results in a composition method formed from two steps of length $h/2$. The second step is a step of the symplectic Euler (SE) method and the first step is a step of the SE's adjoint method. Alternatively we can see this method as a partitioned Runge-Kutta method (see (Hairer et al. 2002, p25,p34)) with coefficients

$$\begin{array}{c|cc} 1/2 & 0 & 1/2 \\ 1/2 & 0 & 1/2 \\ \hline & 1/2 & 1/2 \end{array} \qquad \begin{array}{c|cc} 1/2 & 1/2 & 0 \\ 1/2 & 1/2 & 0 \\ \hline & 1/2 & 1/2 \end{array}.$$

3.2 Mechanical modelling

One of the most important principles in modelling the physical world is Hamilton's principle of least action (Arnold (1980), Feynman et al. (1963)). As described in the introduction (Section 2.3.1), using this principle requires the construction of the La-

[1] The condition $w''(x) \neq 0$ of the introduction to this section (Section 3.1) now ensures that the inverse of w' exists.

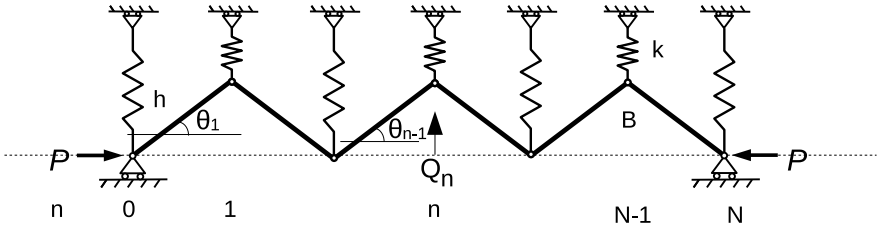

Figure 3.1: *This is the discrete mechanical system of Figure 1.1 (b) reproduced with the various coordinates and numbering conventions used in this, and subsequent, chapters.*

grangian function $\mathcal{L}(\boldsymbol{Q}, \dot{\boldsymbol{Q}})$ (where $\boldsymbol{Q} = (Q_0, \ldots, Q_N)^{\mathrm{T}}$), from the difference of the kinetic energy of the system $T(\boldsymbol{Q}, \dot{\boldsymbol{Q}})$ and the potential energy $V(\boldsymbol{Q}, \dot{\boldsymbol{Q}})$. The Euler-Lagrange equations (2.4) for this functional then give us the evolution equations for the system's state vector $\boldsymbol{Q}$. We now construct the function $\mathcal{L}(\boldsymbol{Q}, \dot{\boldsymbol{Q}})$ for the mechanical system shown in Figure 3.1 and assume, initially, that the boundaries are not constrained.

The potential energy is calculated by subtracting the work done by the load from the energy stored in the springs (Hunt et al. (1997)). The end shortening due to an individual link e_n, $n = 1, \ldots, N$ (i.e. the difference in the horizontal displacement of its end points) is

$$e_{n+1} = \begin{cases} h\left(1 - \sqrt{1 - \left(\frac{Q_{n+1} - Q_n}{h}\right)^2}\right) & \text{for} \quad -\pi/2 \leq \theta_n \leq \pi/2 \\ h\left(1 + \sqrt{1 - \left(\frac{Q_{n+1} - Q_n}{h}\right)^2}\right) & \text{for} \quad \pi/2 \leq |\theta_n| \leq \pi \end{cases}$$

for $n = 0, \ldots, N-1$, and so the work done by the load is $P\mathcal{E}$ where $\mathcal{E} = \sum e_n$ is the total end shortening of the system. In chapters 4 and 5 we restrict our attention to the first of these two θ_n ranges allowing us to write

$$V = \tfrac{1}{2}k \sum_{n=0}^{N} Q_n^2 - Ph \sum_{n=0}^{N-1} \left(1 - \sqrt{1 - \left(\frac{Q_{n+1} - Q_n}{h}\right)^2}\right). \tag{3.17}$$

As an aside, it is not immediately clear why the potential energy of the system should go down when the load P does work on it. This is easily justified if we consider the loads P to be applied, as shown in Figure 3.2, by weights attached to the end pivots by means of inextensible strings (Thompson & Hunt 1973, §3.1). Now it is clear that when the system shortens by total length $\mathcal{E}$ the weights move down and their potential energy

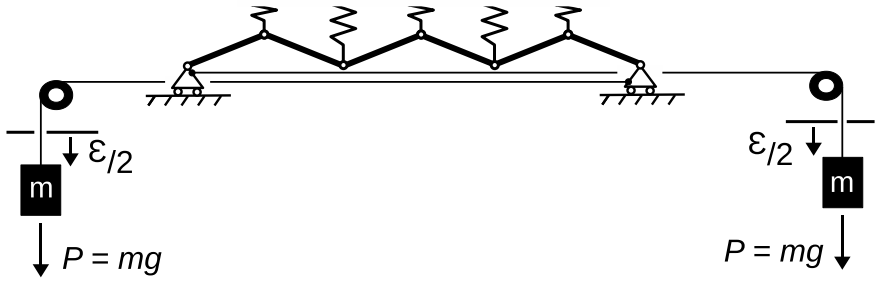

Figure 3.2: *This figure illustrates the justification in the text for why the potential energy of the whole mechanical system is considered to decrease when the load P does work shortening the system by the length $\mathcal{E}$.*

is reduced by the amount $mg\mathcal{E}$. Since these weights are chosen such that $P = mg$ the reduction in potential energy of this extended system due to the end shortening $\mathcal{E}$ is $P\mathcal{E}$.

The full geometric nonlinearity is retained in the potential (3.17). This will enable us, in the next chapter, to investigate the full large displacement behaviour of the static equilibrium states. However, methods for considering the fully nonlinear dynamic behaviour are far more difficult to find and use, we therefore take a first order approximation to the full kinetic energy of this system. We assume, also, that the links and springs are mass-less and so the only mass, m, in this mechanical system is located at the pivots connecting neighbouring links. If we label the horizontal coordinate of each pivot y_n we have

$$y_n = y_0 + h\sum_{i=1}^{n}\sqrt{1-\left(\frac{Q_i - Q_{i-1}}{h}\right)^2} \text{ for } n = 1, \ldots, N,$$

which, if we differentiate with respect to time, gives

$$\dot{y}_n = \dot{y}_0 - h\sum_{i=1}^{n}\bar{g}\left(\frac{Q_i - Q_{i-1}}{h}\right)\left(\frac{\dot{Q}_i - \dot{Q}_{i-1}}{h}\right)$$

where $\bar{g}(x) = x/\sqrt{1-x^2}$. In the above expression another degree of freedom has been introduced, y_0, which gives the overall horizontal displacement of the system. Since there is no net external force we can evaluate $\dot{y}_0$ by requiring the horizontal component of the centre of mass of the system $\bar{y}$ to be time independent i.e. $\dot{\bar{y}} = 0$. Evaluating the

horizontal component of the centre of mass we get

$$\bar{y} = \frac{1}{N+1}\sum_{i=0}^{N} y_i$$

and the condition $\dot{\bar{y}} = 0$ then becomes

$$\sum_{i=0}^{N} \dot{y}_i = 0. \tag{3.18}$$

To simplify these expressions we now expand them for small displacements, i.e. let $Q_n = \epsilon\bar{Q}_n$ and then expand for small ϵ. Doing this we get

$$\begin{aligned} y_n &= y_0 + nh - \frac{\epsilon^2}{2h}\sum_{i=1}^{n}(\bar{Q}_i - \bar{Q}_{i-1})^2 + \mathcal{O}(\epsilon^4) \\ \dot{y}_n &= \dot{y}_0 - \frac{\epsilon^2}{h}\sum_{i=1}^{n}(\bar{Q}_i - \bar{Q}_{i-1})(\dot{\bar{Q}}_i - \dot{\bar{Q}}_{i-1}) + \mathcal{O}(\epsilon^4). \end{aligned}$$

This expression along with (3.18) implies that $\dot{y}_0 = \mathcal{O}(\epsilon^2)$ and so $\dot{y}_i = \mathcal{O}(\epsilon^2)$. The total kinetic energy of the system is given by

$$T = \sum_{n=0}^{N}\frac{m}{2}\dot{y}_n^2 + \sum_{n=0}^{N}\frac{m}{2}\dot{Q}_n^2,$$

and since $\dot{y}_n^2 = \mathcal{O}(\epsilon^4)$ for all n neglecting terms of order ϵ^4 and greater we have the approximate kinetic energy

$$T = \sum_{n=0}^{N}\frac{m}{2}\dot{Q}_n^2.$$

With this kinetic energy and the potential energy (3.17) the Lagrangian $\mathcal{L}(\boldsymbol{Q}, \dot{\boldsymbol{Q}})$ is given, after removing the constant terms in the potential, by

$$\mathcal{L}(\boldsymbol{Q}, \dot{\boldsymbol{Q}}) = \sum_{n=0}^{N}\frac{m}{2}\dot{Q}_n^2 - \frac{k}{2}\sum_{n=0}^{N}Q_n^2 - Ph\sum_{n=0}^{N-1}\sqrt{1 - \left(\frac{Q_{n+1} - Q_n}{h}\right)^2}. \tag{3.19}$$

3.2.1 Nondimensionalisation

To bring the Lagrangian into nondimensional form we have two choices. We can nondimensionalise the displacements Q_n using the length of the individual links h so that

the new, nondimensional quantities $U_n^{(1)}$, p, $\mathcal{L}^{(1)}$ and τ_1 are given by

$$U_n^{(1)} = \frac{Q_n}{h}, \quad p = \frac{4P}{kh}, \quad \mathcal{L}^{(1)} = \frac{\mathcal{L}}{kh^2}, \quad \tau_1 = \sqrt{\frac{k}{m}}t \tag{3.20}$$

so that

$$\mathcal{L}^{(1)}(\boldsymbol{U}^{(1)}, \dot{\boldsymbol{U}}^{(1)}) = \sum_{n=0}^{N} \left(\frac{1}{2} \left(\dot{U}_n^{(1)} \right)^2 - \frac{1}{2} \left(U_n^{(1)} \right)^2 \right) - \frac{p}{4} \sum_{n=0}^{N-1} \sqrt{1 - \left(U_{n+1}^{(1)} - U_n^{(1)} \right)^2}.$$

Or, we can choose the total length of the system $L = Nh$ to nondimensionalise the displacements resulting in the nondimensional system

$$\delta = \frac{h}{L}, \quad U_n^{(2)} = \frac{Q_n}{L}, \quad \mathcal{L}^{(2)} = \frac{\lambda \mathcal{L}}{kL^2}, \quad \lambda = \frac{kL^2}{Ph} = \frac{kL}{P\delta}, \quad \tau_2 = \sqrt{\frac{P\delta}{mL}}t \tag{3.21}$$

giving

$$\mathcal{L}^{(2)}(\boldsymbol{U}^{(2)}, \dot{\boldsymbol{U}}^{(2)}) = \sum_{n=0}^{N} \left(\frac{1}{2} \left(\dot{U}_n^{(2)} \right)^2 - \frac{\lambda}{2} \left(U_n^{(2)} \right)^2 \right) - \sum_{n=0}^{N-1} \sqrt{1 - \left(\frac{U_{n+1}^{(2)} - U_n^{(2)}}{\delta} \right)^2}. \tag{3.22}$$

The first of these two scalings is more appropriate for considering small values of N and considering the behaviour as the physical load P is varied (since $p \propto P$). The second is more appropriate for considering large N where the system approaches a continuum limit. In this case, as we shall see in the next chapter, the parameter δ is the parameter that tell us how close to the continuum limit we are.

As both of these interpretations will be used in this thesis it is useful to note the relations between the two:

$$U_n^{(1)} = \frac{U_n^{(2)}}{\delta}, \quad p = \frac{4}{\delta^2 \lambda}, \quad \tau_1 = \sqrt{\lambda}\tau_2. \tag{3.23}$$

3.2.2 Constraints and equations of motion

In the previous section the Lagrangian function for the mechanical system of Figure 3.1 was derived with no constraints on the ends of the mechanical system. As explained in Chapter 2, for the rest of this thesis we consider fixed boundaries. We have seen already, in Section 3.1 of this chapter, how these fixed constraints are applied to modelling the static equilibrium states of the system using a discrete boundary value problem. Now, to be completely explicit in how these conditions are incorporated into the dynamic

model, we use the theory of Lagrange multipliers to include these constraints. It will be seen that the result of this is that we can reduce the system dimension by two, from $N+1$ to $N-1$, and simply consider the internal nodes.

The constraint functions we are applying are $U_0(t) = 0$ and $U_N(t) = 0$ for all t. To determine the dynamics of the system subject to these constraints we introduce the two undetermined functions or multipliers $\lambda_1(t)$ and $\lambda_2(t)$ and the new Lagrangian

$$\mathcal{L}_2 = \mathcal{L}^{(2)}(\boldsymbol{U}, \dot{\boldsymbol{U}}) - \lambda_1 U_0 - \lambda_2 U_N. \tag{3.24}$$

where $\mathcal{L}^{(2)}$ is given by (3.22). The Euler-Lagrange equations for this new Lagrangian are

$$\begin{aligned}
\ddot{U}_0 &= -\lambda U_0 - \frac{1}{\delta}\bar{g}\left(\frac{U_1 - U_0}{\delta}\right) + \frac{1}{\delta}\bar{g}\left(\frac{U_0}{\delta}\right) - \lambda_1 \\
\ddot{U}_n &= -\lambda U_n - \frac{1}{\delta}\bar{g}\left(\frac{U_{n+1} - U_n}{\delta}\right) + \frac{1}{\delta}\bar{g}\left(\frac{U_n - U_{n-1}}{\delta}\right) \\
\ddot{U}_N &= -\lambda U_N - \frac{1}{\delta}\bar{g}\left(\frac{-U_N}{\delta}\right) + \frac{1}{\delta}\bar{g}\left(\frac{U_N - U_{N-1}}{\delta}\right) - \lambda_2
\end{aligned} \tag{3.25}$$

for $n = 1, \ldots, N-1$ and $\bar{g}(x) = x/\sqrt{1-x^2}$. Here we see that the specific structure of these equations allows us to, almost trivially, determine the undetermined multipliers analytically and reduce the dimension of the system. (This is not the case , however, for the more general formulation of Chapter 6.) The constraint equations $U_0 = U_N = 0$ imply that $\ddot{U}_0 = \ddot{U}_N = 0$ and so

$$\begin{aligned}
\lambda_1 &= -\lambda U_0 - \frac{1}{\delta}\bar{g}\left(\frac{U_1 - U_0}{\delta}\right) + \frac{1}{\delta}\bar{g}\left(\frac{U_0}{\delta}\right) \\
\text{and} \quad \lambda_2 &= -\lambda U_N - \frac{1}{\delta}\bar{g}\left(\frac{-U_N}{\delta}\right) + \frac{1}{\delta}\bar{g}\left(\frac{U_N - U_{N-1}}{\delta}\right).
\end{aligned}$$

Physically the functions $\lambda_1(t)$ and $\lambda_2(t)$ give the previously unknown vertical reaction forces required at the two end pivots to keep their displacements equal to zero. The $N+1$ equations of motion (3.25) can then be reduced to the $N-1$ equations

$$\begin{aligned}
\ddot{U}_1 &= -\lambda U_1 - \frac{1}{\delta}\bar{g}\left(\frac{U_2 - U_1}{\delta}\right) + \frac{1}{\delta}\bar{g}\left(\frac{U_1}{\delta}\right) \\
\ddot{U}_n &= -\lambda U_n - \frac{1}{\delta}\bar{g}\left(\frac{U_{n+1} - U_n}{\delta}\right) + \frac{1}{\delta}\bar{g}\left(\frac{U_n - U_{n-1}}{\delta}\right) \\
\ddot{U}_{N-1} &= -\lambda U_{N-1} - \frac{1}{\delta}\bar{g}\left(\frac{-U_{N-1}}{\delta}\right) + \frac{1}{\delta}\bar{g}\left(\frac{U_{N-1} - U_{N-2}}{\delta}\right)
\end{aligned} \tag{3.26}$$

for $n = 2, \ldots, N-2$. These are the equations studied in Chapter 5.

3.2.3 A discrete boundary value problem

We now apply some of the general results of Section 3.1 to the specific mechanical system modelled in the previous few sections. In doing this we derive a specific discrete boundary value problem which is then solved in the next chapter to give the static equilibrium states of the mechanical system that has been considered above. To apply the general results from Section 3.1 we bring the potential energy of the mechanical system into the forms (3.1) and (3.10) by setting $\dot{\boldsymbol{U}} = 0$ in (3.22) and multiplying by the factor $-\delta$. This gives

$$\begin{aligned} V(\boldsymbol{U}) =& \delta \sum_{n=0}^{N} \frac{\lambda}{2}(U_n)^2 + \delta \sum_{n=0}^{N-1} \sqrt{1 - \left(\frac{U_{n+1} - U_n}{\delta}\right)^2} \\ =& \sum_{n=0}^{N-1} L_d(U_n, U_{n+1}) + \frac{\lambda}{4}(U_0^2 + U_N^2) \end{aligned} \tag{3.27}$$

where

$$L_d(U_n, U_{n+1}) = \frac{\delta\lambda}{4}(U_n^2 + U_{n+1}^2) + \delta\sqrt{1 - \left(\frac{U_{n+1} - U_n}{\delta}\right)^2}. \tag{3.28}$$

We are modelling fixed-fixed boundary conditions ($U_0 = U_N = 0$) and so we have made the choice $\beta = 1/2$ in (3.10) which, as discussed in the sections above, gives the resulting discrete BVP extra symmetries. The stationary points of this potential function can then be turned into the solutions of a discrete boundary value problem using Theorem 3.1, and this discrete boundary value problem is defined as follows:

$$\begin{aligned} &\boldsymbol{X_{n+1}} = \phi(\boldsymbol{X_n}) \text{ for } n = 0, \ldots, N-1 \\ &\boldsymbol{X_0} = \begin{pmatrix} 0 \\ W_0 \end{pmatrix}, \quad \boldsymbol{X_N} = \begin{pmatrix} 0 \\ W_N \end{pmatrix} \\ &\delta = \tfrac{1}{N} \end{aligned} \tag{3.29}$$

where $\phi\colon (U_i, W_i)^{\mathrm{T}} \to (U_{i+1}, W_{i+1})^{\mathrm{T}}$ and

$$\begin{aligned} U_{i+1} &= U_i - \delta \frac{W_i + \frac{\delta\lambda}{2}U_i}{\sqrt{1 + (W_i + \frac{\delta\lambda}{2}U_i)^2}} \\ W_{i+1} &= W_i + \frac{\delta\lambda}{2}(U_i + U_{i+1}). \end{aligned}$$

Chapter 4

Static equilibrium states of a second order mechanical system

In the first half (Section 3.1) of the previous chapter it was shown how to derive a discrete boundary value problem (discrete BVP) that, when solved, gives the static equilibrium states of a general lattice model. The second half of that chapter then applied these general results to the specific mechanical system shown in Figures 1.1 (b) and 3.1. This lead to the discrete boundary value problem that we shall study in this chapter:

$$\begin{aligned} &\boldsymbol{X_{n+1}} = \phi(\boldsymbol{X_n}) \text{ for } n = 0, \ldots, N-1 \\ &\boldsymbol{X_0} = \begin{pmatrix} 0 \\ W_0 \end{pmatrix}, \quad \boldsymbol{X_N} = \begin{pmatrix} 0 \\ W_N \end{pmatrix} \\ &\delta = \tfrac{1}{N} \end{aligned} \tag{4.1}$$

where $\phi\colon (U_i, W_i)^{\mathrm{T}} \to (U_{i+1}, W_{i+1})^{\mathrm{T}}$ and

$$U_{i+1} = U_i - \delta \frac{W_i + \frac{\delta\lambda}{2} U_i}{\sqrt{1 + (W_i + \frac{\delta\lambda}{2} U_i)^2}} \tag{4.2a}$$

$$W_{i+1} = W_i + \frac{\delta\lambda}{2}(U_i + U_{i+1}). \tag{4.2b}$$

Later in this chapter it becomes necessary to highlight the dependence of ϕ on δ and when this happens we will call the above map ϕ_δ, we shall also use the notation

$$\phi^N(\boldsymbol{X_0}) = \underbrace{\phi \circ \phi \circ \cdots \circ \phi}_{N \text{ times}}(\boldsymbol{X_0}).$$

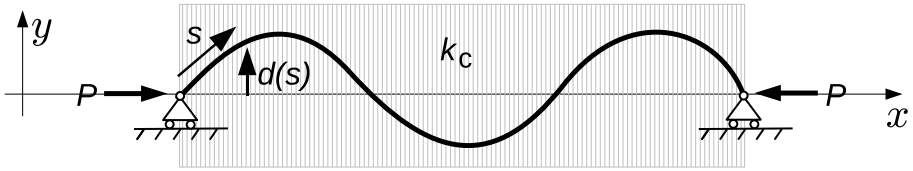

Figure 4.1: *A strut with zero bending stiffness on a Winkler foundation of spring constant per unit length k_c. Variables x and y are the coordinates in the plane of the strut, s measures the distance along its length and d gives the vertical displacement of the strut from the flat state as a function of s.*

This chapter starts with a detailed analysis of the formal continuum limit of this discrete boundary value problem. This continuum limit is introduced, first, through physical considerations; we imagine sending h to zero in the discrete system of Figures 1.1 (b) and 3.1 and use this thought experiment to derive a continuum strut model. This leads to the same differential equations as the formal continuum limit, defined in Section 3.1.2 of the previous chapter, of the discrete boundary value problem shown above. The second half of this chapter extends the work of Hunt et al. (1997) to consider the whole bifurcation diagram and solution symmetries for the above discrete boundary value problem.

4.1 The continuous limit

Imagine the system that would result from sending $h \to 0$ in Figure 3.1, p. 33. As the links get shorter and more numerous, the free pivots between these links causes the chain to behave more and more like a continuous medium with no bending stiffness, like a fine cotton thread. Also, as the links shrink, the number of springs supporting their intersections increases. This supporting medium then approaches that of the Winker foundation, allowing only vertical reaction forces to be applied to to the strut. Requiring the spring stiffness per unit length, rather than the stiffnesses of each individual spring, to be constant ensures that the foundation resulting from the infinite collection of springs is not infinitely stiff. A diagram of the strut on a foundation that arises in the limit of an infinite number of links in the discrete system is shown in Figure 4.1.

Figure 4.1 shows a strut of length L with no bending stiffness, supported on a linear elastic foundation of spring constant per unit length k_c. The deflection of the strut d is a function of the coordinate s which varies along the length of the strut. There is an applied axial load P. As for the discrete case we write the total potential energy of the system as the energy stored in the foundation minus the work done by the applied

load:

$$V = \frac{1}{2}k_c \int_0^L d^2 \, \mathrm{d}s - P\left(L - \int_0^L \sqrt{1 - d'^2} \, \mathrm{d}s\right). \tag{4.3}$$

This expression contains the implicit gradient restriction $-1 < d' < 1$. Seeking stationary points of the total potential energy (4.3) is equivalent to finding stationary points of the functional

$$V = \int_0^L \left[\frac{1}{2}k_c d^2 + P\sqrt{1 - d'^2}\right] \mathrm{d}s. \tag{4.4}$$

The Euler-Lagrange equation for this functional is

$$d'' + \frac{k_c}{P} d(1 - d'^2)^{\frac{3}{2}} = 0$$

with $d(0) = d(L) = 0$. The scalings

$$\bar{s} = Ls, \quad u = Ld, \quad \lambda = \frac{k_c L^2}{P} \tag{4.5}$$

then give the non-dimensionalised differential equation

$$u'' + \lambda u(1 - u'^2)^{\frac{3}{2}} = 0 \tag{4.6a}$$

$$\text{with boundary conditions } u(0) = 0 \text{ and } u(1) = 0. \tag{4.6b}$$

In Section 3.1.2 we saw that, in general, considering the formal continuum limit of a discrete lattice system leads to a map that is a numerical integrator for an ordinary differential equation. If we use the results of Section 3.1.2 to determine the differential equation that corresponds to the specific discrete mechanical system we are studying in this chapter (see Figure 3.1, p. 33) we arrive at exactly the differential equation (4.6a) derrived above. This confirms the equivalence of the two different formal continuum limits we have studied: the continuum limit derived using physical reasoning above, and the formal limit derived using the ideas of discrete mechanics and variational integration in the previous chapter.

The differential equation (4.6a) has first integral

$$E = \frac{1}{\sqrt{1 - u'^2}} + \frac{\lambda u^2}{2} \tag{4.7}$$

and Hamiltonian

$$H(u, w) = -\sqrt{1 + w^2} - \lambda u^2/2 \tag{4.8}$$

with $w = -u'/\sqrt{1 - u'^2}$. If we let $\boldsymbol{z} = (u, w)^{\mathrm{T}}$ the corresponding phase space flow is

given by Hamilton's equations of motion applied to the above Hamiltonian:

$$\boldsymbol{z}' = J\boldsymbol{\nabla}H \quad \text{which implies} \quad \begin{pmatrix} u' \\ w' \end{pmatrix} = \begin{pmatrix} -w/\sqrt{1+w^2} \\ \lambda u \end{pmatrix} \tag{4.9}$$

where

$$J = \begin{pmatrix} 0 & 1 \\ -1 & 0 \end{pmatrix} \quad \text{and} \quad \boldsymbol{\nabla}H = \begin{pmatrix} \frac{\partial H}{\partial u} \\ \frac{\partial H}{\partial w} \end{pmatrix}.$$

It is useful, in terms of understanding the physical behaviour of this system, if we note that $w(s) = -\tan(\theta(s))$ where $\theta(s)$ is the angle the strut makes with the horizontal at a distance s from the left end.

4.1.1 Bifurcation behaviour

We begin our analysis of the continuous boundary value problem (4.6) by determining the linear behaviour of the Hamiltonian differential equation (4.9) about the origin. This linear behaviour is determined by the eigenvalues $\mu_\pm$ of the matrix

$$\left.\frac{\mathrm{d}J\boldsymbol{\nabla}H}{\mathrm{d}\boldsymbol{z}}\right|_{\boldsymbol{z}=\boldsymbol{0}} = \begin{pmatrix} 0 & -1 \\ \lambda & 0 \end{pmatrix}.$$

These are $\mu_\pm = \pm\sqrt{-\lambda}$, showing that for $\lambda > 0$ the origin is an elliptic equilibrium and for $\lambda < 0$ it is hyperbolic. This is illustrated in Figure 4.2 which shows the level sets of the Hamiltonian (4.8) for $\lambda = \pm 100$. Before we move on to consider the boundary value problem we first consider (4.6a) as an initial value problem. As we expect from the level sets shown in Figure 4.2, for $\lambda > 0$ and $(u(0), w(0)) \neq (0, 0)$, all solutions to this IVP are periodic. This, along with the period of these periodic solutions, is proved in the following proposition.

Proposition 4.1. *The differential equation (4.9) viewed as an IVP with $\lambda > 0$, $u(0) = 0$ and $w(0) = w_0$ has periodic solutions for all w_0 with period given by*

$$T(w_0) = 2\sqrt{\frac{8}{\lambda(\mathcal{E}+1)}}\left[(\mathcal{E}+1)E(k) - K(k)\right] \tag{4.10}$$

where $\mathcal{E} = \sqrt{1+w_0^2}$, $k^2 = (\mathcal{E}-1)/(\mathcal{E}+1)$, $K(k)$ and $E(k)$ are the complete elliptic integrals of the first and second kinds respectively.

Proof. For $\lambda > 0$ $\det(\mathrm{d}^2H/\mathrm{d}\boldsymbol{z}^2) = \lambda(1+w^2)^{-3/2} > 0$ and so the Hamiltonian (4.8) is

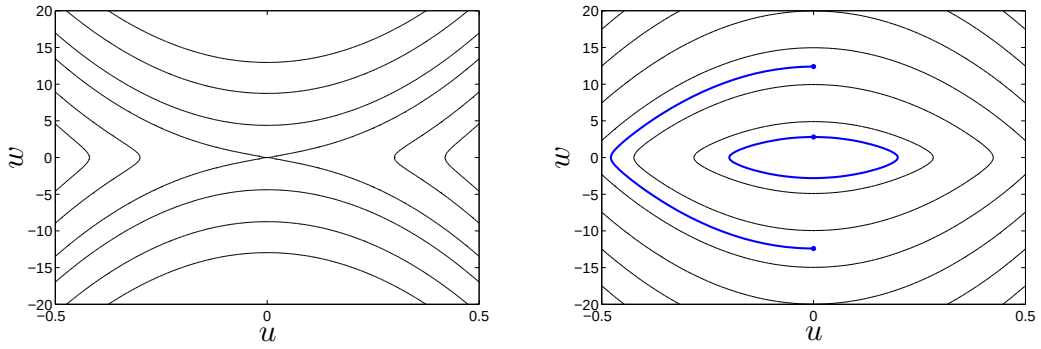

Figure 4.2: *Level sets of the Hamiltonian function (4.8) for* $\lambda = -100$ *(left) and* $\lambda = 100$ *(right) in the* (u, w) *phase plane. The thick blue lines in the right pane show the BVP solutions on the primary branch (outer solution) and secondary,* $m = 2$*, branch (inner solution) at* $\lambda = 100$*.*

convex for all $(u, w) \in \mathbb{R}^2$. This implies that its level sets are convex closed curves and since the evolution of the system is restricted to a particular level set all solutions are periodic with period T. We now find this period analytically.

From (4.7) we have

$$u' = \pm \sqrt{\frac{\left(\mathcal{E} - \frac{\lambda u^2}{2}\right)^2 - 1}{\left(\mathcal{E} - \frac{\lambda u^2}{2}\right)^2}}, \tag{4.11}$$

and choosing the positive square root in this expression gives us the value of u' in the lower half of the $(u, w)^{\mathrm{T}}$ phase plane ($u' > 0$ and equation (4.9) implies that $w < 0$). Rearranging and then integrating this expression we get

$$t = \int_{u_1}^{u_2} \frac{\mathcal{E} - \frac{\lambda u^2}{2}}{\sqrt{\left(\mathcal{E} - \frac{\lambda u^2}{2}\right)}} \, \mathrm{d}u,$$

which gives the 'time' taken for the solution to move along the $w < 0$ part of the level set of Hamiltonian (4.8) with value $-\mathcal{E}$ from the point u_1 to u_2 ($u_1 < u_2$). The form of the Hamiltonian (4.8) shows that this system is invariant under the transformation $u \to -u$ and $w \to -w$ allowing the computation of the full period of this solution via

$$T = 4 \int_0^{\bar{u}} \frac{\mathcal{E} - \frac{\lambda u^2}{2}}{\sqrt{\left(\mathcal{E} - \frac{\lambda u^2}{2}\right)}} \, \mathrm{d}u. \tag{4.12}$$

The quantity $\bar{u}$ is given by $\bar{u} = \sqrt{\frac{2}{\lambda}(\mathcal{E} - 1)}$ and is the positive solution to $H(\bar{u}, 0) = -\mathcal{E}$.

The substitution $y = u/\bar{u}$ brings (4.12) into the form

$$T = 2\sqrt{\frac{8(\mathcal{E}-1)}{\lambda}} \int_0^1 \frac{\left[(\mathcal{E}+1)-(\mathcal{E}-1)y^2\right]-1}{\sqrt{(\mathcal{E}-(\mathcal{E}-1)y^2)^2-1}}\,\mathrm{d}y.$$

Expanding and re-factorising the denominator leaves us, after a little manipulation, with

$$T = 2\sqrt{\frac{8}{\lambda(\mathcal{E}+1)}} \int_0^1 \frac{(\mathcal{E}+1)(1-k^2y^2)-1}{\sqrt{(1-y^2)(1-k^2y^2)}}\,\mathrm{d}y$$

where $k^2 = (\mathcal{E}-1)/(\mathcal{E}+1)$. Rearranging we have

$$\begin{aligned} T &= 2\sqrt{\frac{8}{\lambda(\mathcal{E}+1)}}\left[(\mathcal{E}+1)\int_0^1 \sqrt{\frac{1-k^2y^2}{1-y^2}}\,\mathrm{d}y - \int_0^1 \frac{1}{\sqrt{(1-y^2)(1-k^2y^2)}}\,\mathrm{d}y\right] \\ &= 2\sqrt{\frac{8}{\lambda(\mathcal{E}+1)}}\left[(\mathcal{E}+1)E(k)-K(k)\right]. \end{aligned}$$

□

The solutions to the boundary value problem (4.6) above are the set of periodic solutions found in Proposition 4.1 that have period that is an integer divisor of two, i.e. $T = 2/m$ for $m \in \mathbb{Z}^+$. In this way, we label each solution to the boundary value problem by m. For example, the solutions for $m = 1$ and $m = 2$ are shown in the right pane of Figure 4.2. The next Lemma guarantees the existence of such a periodic solution to the IVP for $\lambda > \pi^2$ and also proves that for each m there is a globally unique (up to phase) periodic solution with period $T = 2/m$.

Lemma 4.1. *The function $T(w_0)$ of Proposition 4.1 satisfies*

$$T(0) = \frac{2\pi}{\sqrt{\lambda}} \quad \textit{and} \quad \frac{\mathrm{d}T}{\mathrm{d}w_0} > 0 \quad \textit{for } w_0 > 0.$$

Proof. Substituting $w_0 = 0$ into the expressions of Proposition 4.1 we get $\mathcal{E} = 1$ and $k = 0$, and since the complete elliptic integrals of the first and second kinds satisfy $K(0) = \pi/2$ and $E(0) = \pi/2$ (Abramowitz & Stegun 1964, §17.3), $T(0) = 2\pi/\sqrt{\lambda}$.

We can evaluate $\mathrm{d}T/\mathrm{d}w_0$ by using the following result from Section 3.3 of Abramowitz & Stegun (1964): for

$$F(w_0) = \int_{a(w_0)}^{b(w_0)} f(u, w_0)\,\mathrm{d}u$$

$$F'(w_0) = b'(w_0)f(b(w_0), w_0) - a'(w_0)f(a(w_0), w_0) + \int_{a(w_0)}^{b(w_0)} \partial_{w_0} f(u, w_0)\, \mathrm{d}u. \quad (4.13)$$

Defining

$$f(u, w_0) = \frac{\mathcal{E}(w_0) - \lambda u^2/2}{\sqrt{(\mathcal{E}(w_0) - \lambda u^2/2)}}$$

and using (4.13) we have

$$\frac{\mathrm{d}T}{\mathrm{d}w_0} = 4\bar{u}'(w_0)f(\bar{u}(w_0), w_0) + 4\int_0^{\bar{u}(w_0)} \partial_{w_0} f(u, w_0)\, \mathrm{d}u. \quad (4.14)$$

Before we show that $\mathrm{d}T/\mathrm{d}w_0 > 0$ we first derive some preliminary results:

$$\mathcal{E}(w_0) = \sqrt{1 + w_0^2} \quad \text{which implies} \quad \frac{\mathrm{d}\mathcal{E}}{\mathrm{d}w_0} = \frac{w_0}{\sqrt{1 + w_0^2}} > 0 \quad \text{for} \quad w_0 > 0, \quad (4.15)$$

also,

$$\bar{u}(w_0) = \sqrt{\frac{2}{\lambda}(\mathcal{E}(w_0) - 1)} \quad \text{implies} \quad \frac{\mathrm{d}\bar{u}}{\mathrm{d}w_0} = \frac{1}{\lambda}\frac{\mathrm{d}\mathcal{E}}{\mathrm{d}w_0}\left(\frac{2}{\lambda}(\mathcal{E}(w_0) - 1)\right)^{-\frac{1}{2}}$$
$$\text{and so } \frac{\mathrm{d}\bar{u}}{\mathrm{d}w_0} > 0 \text{ for } w_0 > 0 \text{ and } \lambda > 0. \quad (4.16)$$

Therefore

$$\frac{\partial f(u, w_0)}{\partial w_0} = \left(4\sqrt{\mathcal{E}(w_0) - \frac{\lambda u^2}{2}}\right)^{-\frac{1}{2}} \frac{\mathrm{d}\mathcal{E}}{\mathrm{d}w_0} > 0 \quad \text{for} \quad w_0 > 0 \quad \text{by (4.15)}. \quad (4.17)$$

We can now see that (4.16) and (4.17) along with (4.14) and $f(\bar{u}(w_0), w_0) = 1$ imply that

$$\frac{\mathrm{d}T}{\mathrm{d}w_0} > 0 \text{ for } w_0 > 0.$$

□

The invariance of the Hamiltonian (4.8) under the transformation $w \to -w$ tells us that for each BVP solution with $w(0) = w_0 > 0$ there is another BVP solution with $w(0) = -w_0$. This means that for each m there are two solutions to the BVP. We will call the BVP solution with $w(0) > 0$ and $m = 1$, which is formed from one half period of the periodic IVP solution with period 2, the *primary* solution. Given this primary solution we can construct all of the other solutions to this BVP using the following proposition.

Proposition 4.2. *If the primary branch of solutions to the BVP (4.6) is given by*

$\bar{z}(\bar{s};\bar{\lambda}) = (\bar{u}(\bar{s};\bar{\lambda}),\bar{w}(\bar{s};\bar{\lambda}))^{\mathrm{T}}$ for $\bar{s} \in [0,1]$, where for $s \in \mathbb{R}$ $\bar{z}(\bar{s};\bar{\lambda})$ is the periodic solution to the Hamiltonian system (4.9) of period 2, then the remaining branches with $w(0;\lambda) > 0$, labelled by $n \in \{2,3,4,\ldots\}$, are given by $(u(s;\lambda),w(s;\lambda))^{\mathrm{T}}$, where

$$\lambda = m^2\bar{\lambda}, \quad u(s;\lambda) = \frac{1}{m}\bar{u}\left(ms;\frac{\lambda}{m^2}\right), \quad \textit{and} \quad w(s;\lambda) = \bar{w}\left(ms;\frac{\lambda}{m^2}\right) \tag{4.18}$$

with $s \in [0,1]$.

Proof. We shall first prove that $(u(s;\lambda),w(s;\lambda))^{\mathrm{T}}$ satisfies the equations (4.9). In the proof $'$ denotes the following idea of differentiation at a point:

$$u'(a;b) = \left.\frac{\mathrm{d}u(s;\lambda)}{\mathrm{d}s}\right|_{\substack{s=a\\ \lambda=b}}.$$

In the following set of equalities the first equality of each line determines u' and w' in terms of $\bar{u}'$ and $\bar{w}'$, the second equality uses the fact that $\bar{u}'$ and $\bar{w}'$ satisfy (4.9) and the third equality uses (4.18);

$$u'(s;\lambda) = \frac{m}{m}\bar{u}'\left(ms;\frac{\lambda}{m^2}\right) = \frac{-\bar{w}\left(ms;\frac{\lambda}{m^2}\right)}{\sqrt{1+\bar{w}\left(ms;\frac{\lambda}{m^2}\right)^2}} = \frac{-w(s;\lambda)}{\sqrt{1+w(s;\lambda)^2}} \quad \text{and}$$
$$w'(s;\lambda) = m\bar{w}'\left(ms;\frac{\lambda}{m^2}\right) = m\frac{\lambda}{m^2}\bar{u}\left(ms;\frac{\lambda}{m^2}\right) = \lambda u(s;\lambda).$$

To prove that the solution $\boldsymbol{z}$ satisfies the boundary value problem we check the boundary conditions, $u(0;\lambda) = 0$ and $u(1;\lambda) = 0$, are satisfied: $u(0;\lambda) = \bar{u}(0;\lambda/m^2) = 0$ and $u(1;\lambda) = \bar{u}(m;\lambda/m^2) = 0$ since $\bar{u}$ is a period two solution to the differential equations (4.9) that satisfies $\bar{u}(m;\lambda/m^2) = 0$ for any $m \in \mathbb{Z}$. □

The bifurcation diagram for this BVP can now be constructed and is shown in Figure 4.3. Due to the uniqueness of solutions of the related IVP the BVP solutions can be uniquely represented in $(w(0),\lambda)$ space. Each branch, labelled by m, bifurcates from the flat solution at the λ value $\lambda = m^2\pi^2$. We can obtain an analytic expression for the λ dependence of $w(0)$ on these branches by using expression (4.10) for the period of the IVP solutions. From Proposition 4.2 we know that $T = 2/m$ on the mth branch, which if we substitute into (4.10) we get

$$\lambda(w_0) = \frac{8m^2}{\sqrt{1+w_0^2}+1}\left(K(k(w_0)) - \left(\sqrt{1+w_0^2}+1\right)E(k(w_0))\right)^2 \tag{4.19}$$

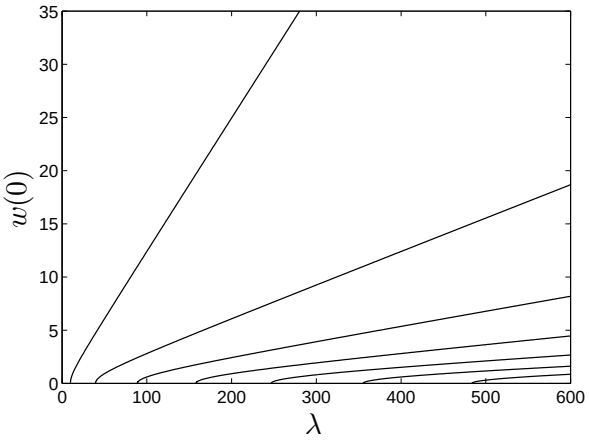

Figure 4.3: *The bifurcation diagram for the BVP (4.6) computed using the explicit expression for $\lambda(w_0)$, equation (4.19).*

with $(k(w_0))^2 = (\sqrt{1+w_0^2}-1)(\sqrt{1+w_0^2}+1)$. It appears from Figure 4.3 that λ depends quadratically on $w(0)$ for small $w(0)$ whilst this dependence appears linear for large $w(0)$. Using the expression (4.19) we can make these limits of the behaviour precise, which is done in the following proposition.

Proposition 4.3. *The limits of (4.19) for large and small w_0 are*

$$\lambda \to 8m^2 w_0 \text{ as } w_0 \to \infty \tag{4.20}$$

and

$$\lambda = m^2\pi^2 + \frac{3m^2\pi^2}{8}w_0^2 + \mathcal{O}(w_0^4) \tag{4.21}$$

for small w_0.

Proof. We first consider small w_0. For small k we can expand $E(k)$ and $K(k)$ as follows (see (Abramowitz & Stegun 1964, §17.3))

$$\begin{aligned} E(k) &= \frac{\pi}{2} + \frac{\pi}{8}k^2 + \mathcal{O}(k^4) \\ K(k) &= \frac{\pi}{2} - \frac{\pi}{8}k^2 + \mathcal{O}(k^4). \end{aligned}$$

Expanding k^2 for small w_0 we have $k^2 = w_0^2/4 - w_0^4/8 + \mathcal{O}(w_0^6)$ and also $\sqrt{1+w_0^2} = 1 + w_0^2/2 - w_0^4/8 + \mathcal{O}(w_0^6)$. Substituting these into (4.19) and keeping terms of order w_0^2 leaves us with (4.21).

For large w_0 we have that $k \to 1$ as $w_0 \to \infty$, also $K(k) \to \frac{1}{2}\ln\left(\frac{16}{1-k^2}\right)$ and $E(k) \to 1$

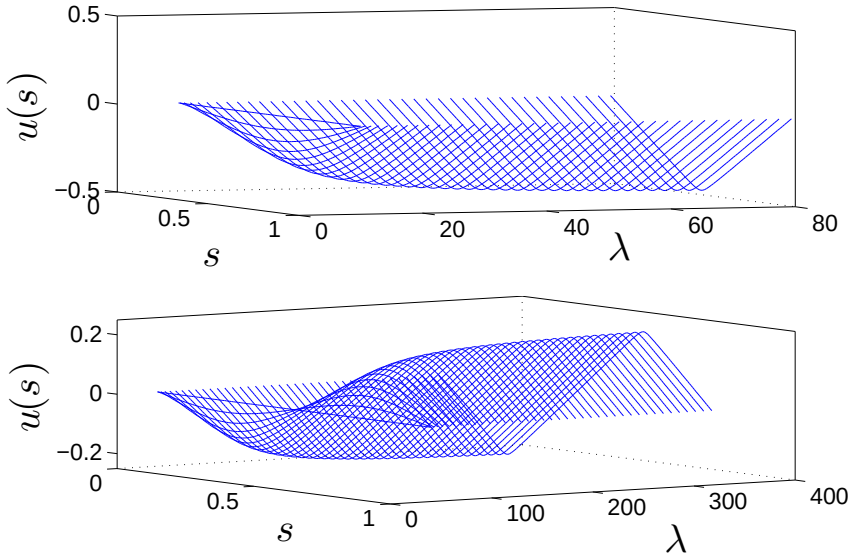

Figure 4.4: *The λ dependence of the primary (top) and $m = 2$ (bottom) solutions to the the continuous BVP (4.6). We see that $u'(s) \to \pm 1$ as $\lambda \to \infty$.*

as $k \to 1$. These, with (4.19) give

$$\begin{aligned} \lambda &\to \frac{8m^2}{\mathcal{E}+1}\left(\tfrac{1}{2}\ln\left(\frac{16}{1-k^2}\right) - (\mathcal{E}+1)\right)^2 \\ &= \frac{8m^2}{\mathcal{E}+1}\left(\tfrac{1}{2}\ln\left(8(\mathcal{E}+1)\right) - (\mathcal{E}+1)\right)^2. \end{aligned}$$

Since $\mathcal{E} = \sqrt{1+w_0^2}$, $\mathcal{E} \to \infty$ as $w_0 \to \infty$ which means that the expression for λ above will be dominated by the polynomial terms in $\mathcal{E}$. Neglecting the logarithmic term and simplifying we arrive at the result: $\lambda \to 8m^2 w_0$ as $w_0 \to \infty$. □

4.1.2 Solution behaviour on the solution branches

We now look at how the solution shapes vary as they move along their respective branches towards higher λ values. The behaviour of the solutions on the first two solution branches with $w(0) > 0$ is shown in Figure 4.4. Equation (4.11) leads us to expect that as $\lambda \to \infty$ $u' \to \pm 1$. This is clearly shown in the figure; as the solutions move away from the sinusoidal form at the bifurcation from the zero solution their shape becomes triangular as $\lambda \to \infty$. It is important to remember at this point that the independent variable s in this section measures the distance along the length of the strut and so the plots of Figure 4.4 do not represent the physical shape of the strut.

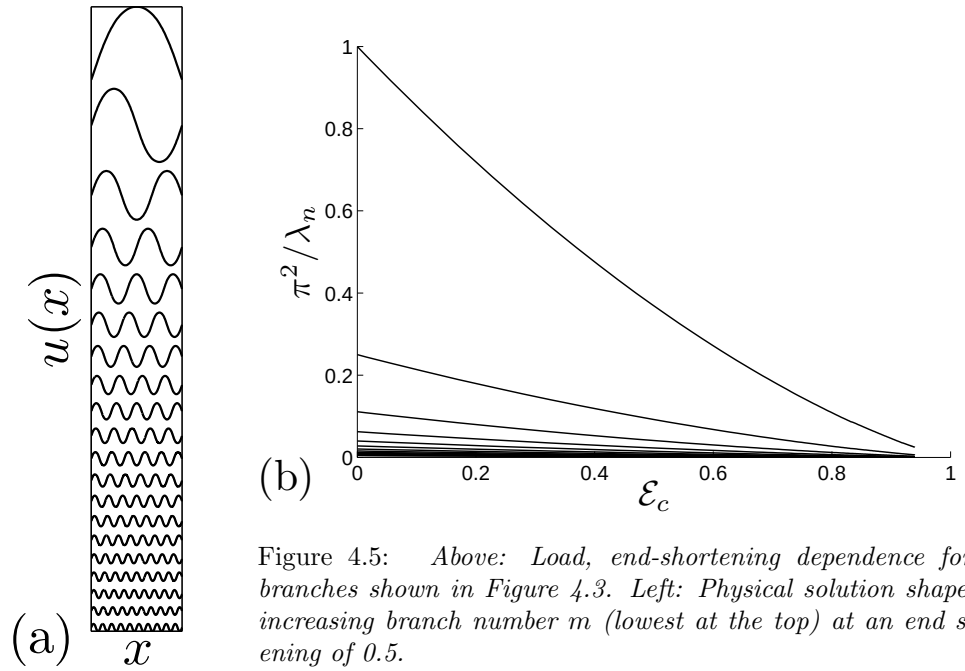

Figure 4.5: *Above: Load, end-shortening dependence for the branches shown in Figure 4.3. Left: Physical solution shapes for increasing branch number m (lowest at the top) at an end shortening of 0.5.*

Imagine an experiment on the continuous strut of Figure 4.1 in which we take the flat equilibrium and gradually increase the load P. The first bifurcation reached will be the bifurcation that occurs at the lowest load or highest λ value ((4.5) implies $\lambda \propto 1/P$). There is, however, no highest λ bifurcation and so to get an idea of the solution that will bifurcate at very low loads we consider a sequence of solutions. This sequence is shown in Figure 4.5 (a) and shows the physical shape of the solutions as we move to higher and higher branch numbers at constant end shortening. Mathematically, the physical shape of the solution is given by $u(x)$ where x is the distance in the horizontal direction calculated from the solution as a function of arc length $u(s)$ via

$$x(s) = \int_0^s \sqrt{1 - \left(\frac{\mathrm{d}u}{\mathrm{d}x}\right)^2}\, \mathrm{d}s.$$

This relation and the property that $u'(s) \to \pm 1$ as $\lambda \to \infty$ tells us that as $\lambda \to \infty$, equivalently $p \to 0$, $x(s) \to 0$ for all s. Specifically the end shortening for the solution $\mathcal{E}_c = 1 - z(1)$ tends to one as $p \to 0$ as shown in Figure 4.5 (b). This analysis tells us that the solution we expect to see physically is the infinitely wrinkled solution approximated at the bottom of Figure 4.5 (a). These results and those from the previous section will be useful in the next section when discerning the mathematical and physical effect discretisation has on this system.

4.2 The discrete BVP

This section considers the discrete BVP (4.1) derived at the end of the previous chapter and extends the work of Hunt et al. (1997) to consider the global bifurcation diagram for this discrete BVP and the detailed symmetry properties of the solutions. This section starts, in Section 4.2.1 below, by looking at the behaviour of the IVP that corresponds to the discrete BVP (4.1). This discussion will help to understand the map behaviour underlying the BVP solutions found later. Before we move onto this discussion the main results on the discrete BVP (4.1) are summarised.

The uniqueness of solutions to the IVP corresponding to the BVP (4.1) tells us that solutions to the BVP for a specific N are uniquely parametrised by W_0 and λ, and so the bifurcation diagrams in figures 4.8 and 4.9 (generated by the bisection algorithm used in Domokos & Holmes (1993)) are plotted in (W_0, λ) space for specific values of N. The ρ_W reversibility of the map ϕ (see below) tells us that if $\boldsymbol{X}_0 = (0, W_0)^{\mathrm{T}}$ is a solution to the BVP so is $\boldsymbol{X}_0 = (0, -W_0)^{\mathrm{T}}$ and so only the positive half of the bifurcation diagrams are plotted.

The results below start by showing that there are $N-1$ primary pitchfork bifurcations from the zero equilibrium state at the λ values $\lambda^*_{n,N} = \frac{2}{\delta^2}\left(2 - \cos\frac{n\pi}{N}\right)$ for $n = 1, 2, \ldots, N-1$ (Section 4.2.2). A discussion then follows of the numerically obtained bifurcation diagram and solution shapes for the discrete BVP. This includes a prediction of the experimental behaviour of the mechanical lattice under controlled end-shortening (or rigid loading) conditions. After this, it is shown (Proposition 4.7) that on all connected solution branches the rotation number is conserved. These results are then used to show that solutions on the first $\lfloor \frac{N-1}{2} \rfloor$ primary branches satisfy $W_0 \to \infty$ as $\lambda \to \infty$. Following this consideration of the behaviour as $\lambda \to \infty$ a scaling argument adds weight to the numerical suggestion that this divergence is linear. The final bifurcation results follow after some symmetry properties of $\phi'(X)$ (Lemma 4.2). These lead us to expect, for even N, $N/2-1$ secondary, symmetry breaking bifurcations on the 'central', $n = N/2$ primary branch at the λ values $\lambda^{(2)}_{k,N} = 4/(\delta^4(1 - \cos k\pi/N))$ for $k = 1, 2, \ldots, N/2 - 1$. The final part of this section (Section 4.2.5) changes theme slightly and presents results on the symmetry relations between different BVP solutions and the symmetry invariants of the BVP solutions.

Before we begin to prove the results previewed above two symmetries of the map ϕ (4.2) (in addition to those already presented in Section 3.1.1) are shown. These further symmetries of ϕ are:

1. ρ_W reversibility: $\rho_W \circ \phi_\delta = \phi_\delta^{-1} \circ \rho_W$ where ρ_W is the involution $\rho_W : \mathbb{R}^2 \to \mathbb{R}^2$, $(U, W)^{\mathrm{T}} \to (U, -W)^{\mathrm{T}}$ and

2. ρ_U reversibility: $\rho_U \circ \phi_\delta = \phi_\delta^{-1} \circ \rho_U$ where ρ_U is the involution $\rho_U : \mathbb{R}^2 \to \mathbb{R}^2$, $(U, W)^{\mathrm{T}} \to (-U, W)^{\mathrm{T}}$.

4.2.1 IVP behaviour

Before the discrete BVP (4.1) is analysed it is helpful to consider the behaviour of the corresponding IVP. This IVP is given by the iterated map ϕ (4.2) with initial conditions $(U_0, W_0)^{\mathrm{T}}$:

$$\boldsymbol{X_{n+1}} = \phi(\boldsymbol{X_n}) \quad \text{with} \quad \boldsymbol{X_0} = (U_0, W_0)^{\mathrm{T}}. \tag{4.22}$$

Proposition 4.4. *The map ϕ has one and only one fixed point at $(0,0)^{\mathrm{T}}$ which exists for all δ and λ.*

Proof. Suppose $\boldsymbol{X} = (U, W)^{\mathrm{T}}$ is a fixed point of ϕ. Then $\phi(\boldsymbol{X}) = \boldsymbol{X}$ and by the first component of (4.2) we have $W + \delta\lambda U/2 = 0$. The second component of (4.2) then gives

$$2U - \delta \frac{W + \delta\lambda U/2}{1 + (W + \delta\lambda U/2)^2)} = 0,$$

which with the previous equation implies that $U = 0$; hence $W = 0$ and $\boldsymbol{X} = (0,0)^{\mathrm{T}}$. □

We can determine character of this fixed point by determining the eigenvalues of the Jacobian of ϕ at $(0,0)^T$. This Jacobian, at the point $\boldsymbol{X}$, is given by

$$[\phi'(\boldsymbol{X})]_{ij} = \frac{\partial[\phi(\boldsymbol{X})]_i}{\partial X_j} \quad \text{which implies} \quad \phi'(\boldsymbol{X}) = \begin{pmatrix} 1 - \frac{\delta^2\lambda}{2\beta(\boldsymbol{X})} & \frac{-\delta}{\beta(\boldsymbol{X})} \\ \delta\lambda - \frac{\delta^3\lambda^2}{4\beta(\boldsymbol{X})} & 1 - \frac{\delta^2\lambda}{2\beta(\boldsymbol{X})} \end{pmatrix} \tag{4.23}$$

where $\beta(\boldsymbol{X}) = (1 + (W + (\delta\lambda U)/2)^2)^{\frac{3}{2}}$. To find $\phi'(\mathbf{0})$ we substitute $\beta(\mathbf{0}) = 1$ into (4.23). The characteristic polynomial for $\phi'(\mathbf{0})$ is $P(\mu) = \mu^2 + \mu(\delta^2\lambda - 2) + 1$ and the discriminant of $P(\mu)$ tells us that the fixed point of ϕ is hyperbolic for $\lambda < 0$ and $\lambda > 4/\delta^2$, and elliptic for $0 < \lambda < 4/\delta^2$. Figure 4.6 shows how the locations, relative to the unit circle in the complex plane, of the eigenvalues of $\phi'(\mathbf{0})$ change as δ and λ are varied. On the solid curves in Figure 4.6 the eigenvalues are repeated and on the dotted curve the eigenvalues have zero real part. The paths in this parameter space that correspond to the physical system buckling under increasing load are paths that

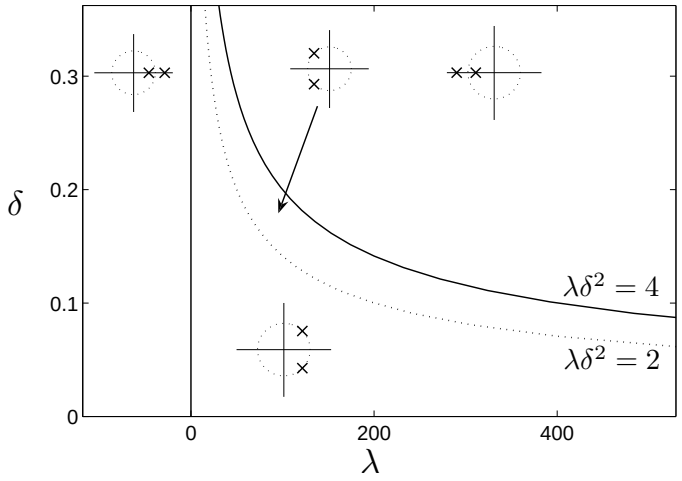

Figure 4.6: *Parameter dependence of the eigenvalues of the zero fixed point of the map ϕ. The inset plots show the location of the eigenvalues (crosses) in the complex plane relative to the real and imaginary axes and the unit circle (dotted).*

move from higher λ values to lower λ values at constant δ. Solving the polynomial equation $P(\mu) = 0$ gives, for $\mu \in \mathbb{C}$, the eigenvalues of $\phi'(\mathbf{0})$:

$$\mu_{\pm} = \frac{1}{2}\left(2 - \delta^2\lambda \pm \sqrt{(\delta^2\lambda - 2)^2 - 4}\right). \tag{4.24}$$

In the elliptic regime we can write $\mu_{\pm} = \exp(\pm \mathrm{i}\theta)$, and using this and (4.24) we can determine the dependence of the argument of the eigenvalues on λ to give

$$\cos\theta = 1 - \frac{\delta^2\lambda}{2} \quad \text{and} \quad \lambda = \frac{2}{\delta^2}(1 - \cos\theta). \tag{4.25}$$

Thus, as λ increases from 0 to $4/\delta^2$, θ increases from 0 to π.

To help describe and visualise the behaviour of the IVP (4.22) for $\lambda > 0$ we now introduce the idea of the rotation number for a point $\boldsymbol{X} \in \mathbb{R}^2$ in the phase space of the map ϕ. This is defined by considering an infinite sequence of angles generated by the IVP iterates $\boldsymbol{X_n}$. The total rotation of each point $\boldsymbol{X_n}$, anticlockwise about the origin from the positive U axis, is denoted by Θ_n. This total rotation is defined so that $0 \leq \Theta_0 < 2\pi$ and $0 \leq \Theta_{n+1} - \Theta_n < 2\pi$. The rotation number for a point $\boldsymbol{X_0}$ is then defined[1] by

$$\rho(\boldsymbol{X_0}) = \frac{1}{2\pi} \lim_{n\to\infty} \frac{\Theta_n - \Theta_0}{n}. \tag{4.26}$$

[1]Computationally the limit is computed over a finite number of iterations e.g. $N = 500$ and then $\rho(\boldsymbol{X_0}) \approx (\Theta_N - \Theta_0)/N$.

Figure 4.7 shows the variation of this rotation number across a section of the phase plane of the map ϕ for six different λ values. As discussed in Section 3.2.1 δ is not a true free parameter in this system, and can be scaled out, and so in Figure 4.7 for convenience we have set $\delta = 1$. We will now look at various aspects of the behaviour of the IVP (4.22) that can be seen in Figure 4.7.

For small λ, see (a) of Figure 4.7, the map ϕ is close to its continuum limit and so the iterates of ϕ follow curves that are close to the contours of the Hamiltonian (4.8) from the previous section. The rotation number is then related to the frequency of the underlying, continuous, periodic solution and decreases as the amplitude of the orbit increases.

To explain some of the behaviour of panes (b)-(d) in Figure 4.7 we recall some ideas from the bifurcation theory of symplectic and reversible maps (Meyer (1970), Ciocci (2004), see also the appendix of Holmes & Williams (1985)). These theories lead us to expect that as the eigenvalues of $\phi'(\mathbf{0})$ move through the complex roots of unity, $\exp(2\pi \mathrm{i} p/q)$ for p, q mutually prime integers, then periodic points of period q will bifurcate from the zero fixed point. Specifically, we expect (Ciocci 2004, Theorem 3) that for $q > 3$ at each bifurcation point exactly two branches of periodic solutions bifurcate which share one or both of the symmetries ρ_U and ρ_W. For $q > 5$ one of these periodic solutions is stable (elliptic) and the other unstable (hyperbolic). This behaviour can be seen in (b)-(d) of Figure 4.7. Pane (b) shows the elliptic regions about high period periodic orbits as small patches of identical colour that are spaced regularly about the origin. The hyperbolic periodic points are in between these patches of colour and the plot also shows the tangling of stable and unstable manifolds for these hyperbolic fixed points. Panes (c) and (d) show this process continuing, with lower period periodic orbits bifurcating from the fixed point as λ is increased. We can also see from (c)-(d)-(e)-(f) that as λ increases some of the periodic solutions are stretched in the W direction.

As described above, as λ is increased through $4/\delta^2$ the fixed point at the origin becomes hyperbolic. This can be seen in pane (e) of Figure 4.7 as the appearance of two regions of rotation number approximately equal to $1/2$ that surround a period two fixed point (see Proposition 4.8) appearing in a bifurcation at $\lambda = 4/\delta^2$. As λ is increased further, much of the remaining regular behaviour of the iterates of ϕ close to the origin is destroyed by a homoclinic tangle. This homoclinic tangle was found in a different map modelling the same physical system in Hunt et al. (1997) and it leads to an infinitely folded structure in the phase space of the IVP close to the fixed point (see, for example, Thompson & Stewart (2002)). The homoclinic tangle causes the generation of infinitely

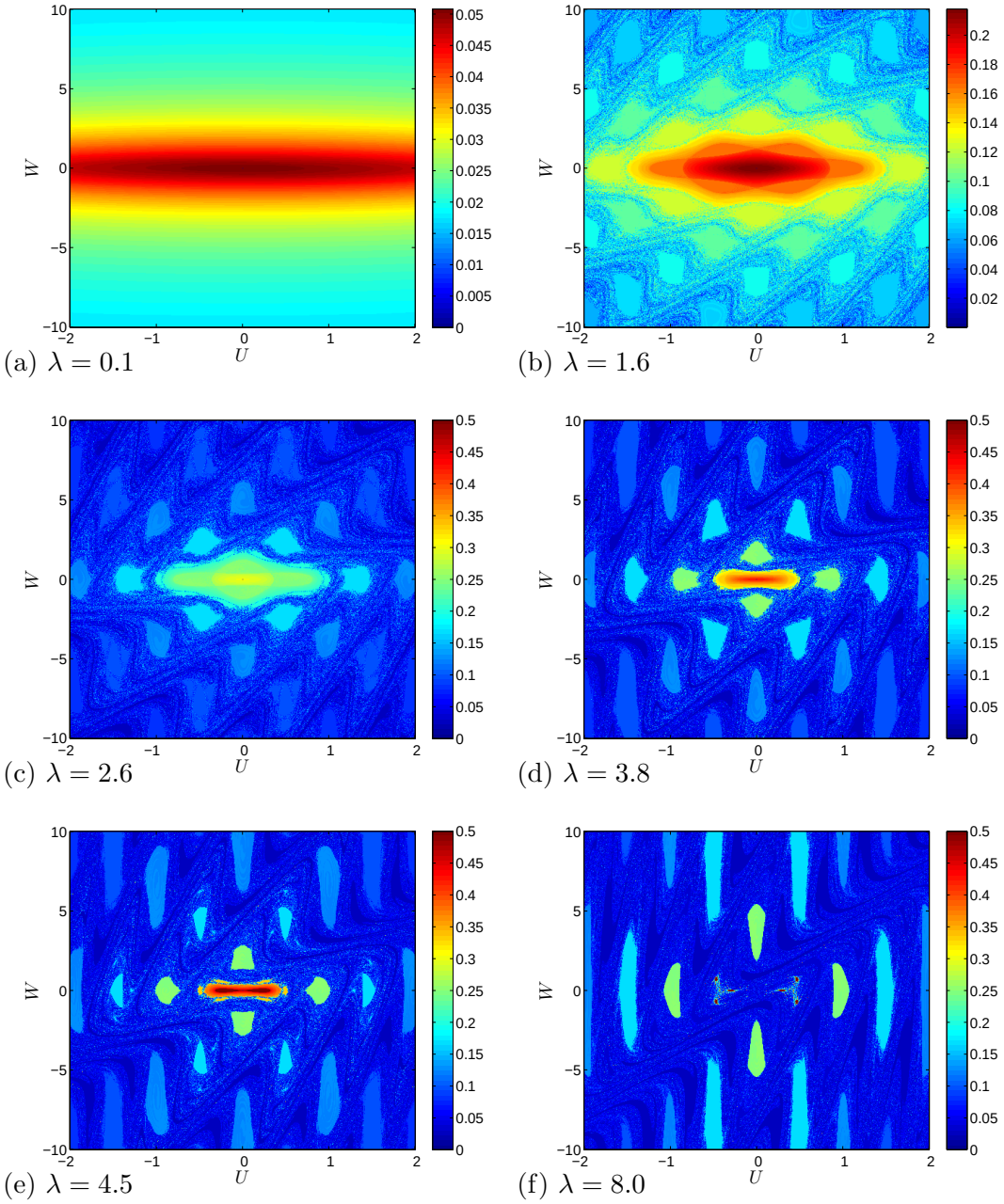

(a) $\lambda = 0.1$ (b) $\lambda = 1.6$

(c) $\lambda = 2.6$ (d) $\lambda = 3.8$

(e) $\lambda = 4.5$ (f) $\lambda = 8.0$

Figure 4.7: *Plots showing how the rotation number (4.26) varies in the phase space of the map ϕ. Plots (a) and (b) are plotted with a different colour scale to bring out the more subtle rotation number variation for these values of λ.*

many periodic solutions to the IVP of various periods some of which also solve the BVP (see Domokos & Holmes (1993) and the next section).

We can determine a first order approximation to the periodic solutions that bifurcate from the fixed point at $\boldsymbol{X} = (0,0)^{\mathrm{T}}$ by transforming into a coordinate system where the linear part of ϕ is a pure rotation. These new coordinates, $\boldsymbol{Y_n}$, are defined by $\boldsymbol{X_n} = T\boldsymbol{Y_n}$ where the transformation matrix T is formed from the imaginary and real parts of the eigenvector $\boldsymbol{\nu}_+$ of $\phi'(\mathbf{0})$. The eigenvector $\boldsymbol{\nu}_+$ is the eigenvector of $\phi'(\mathbf{0})$ that corresponds to the eigenvalue μ_+ and is given by $\boldsymbol{\nu}_+ = (\mathrm{i}\delta/\sin\theta, 1)^{\mathrm{T}}$, this tells us that

$$T = \begin{pmatrix} \frac{\delta}{\sin\theta} & 0 \\ 0 & 1 \end{pmatrix}.$$

The map ϕ transformed into the new coordinate system is given by $\boldsymbol{Y_{n+1}} = T^{-1}\phi(T\boldsymbol{Y_n})$ the linear part of which is given by an anticlockwise rotation of the plane through angle θ:

$$\boldsymbol{Y_{n+1}} = \underbrace{\begin{pmatrix} \cos\theta & -\sin\theta \\ \sin\theta & \cos\theta \end{pmatrix}}_{R_\theta} \boldsymbol{Y_n}.$$

This implies that $\boldsymbol{Y_n} = R_{n\theta}\boldsymbol{Y_0}$ and so

$$\begin{aligned} \boldsymbol{X_n} = T\boldsymbol{Y_n} = TR_{n\theta}\boldsymbol{Y_0} &= TR_{n\theta}T^{-1}\boldsymbol{X_0} \\ &= \begin{pmatrix} \cos(n\theta) & -\frac{\delta}{\sin\theta}\sin(n\theta) \\ \delta^{-1}\sin(n\theta)\sin(\theta) & \cos(n\theta) \end{pmatrix} \begin{pmatrix} U_0 \\ W_0 \end{pmatrix}. \end{aligned} \tag{4.27}$$

This expression gives the dependence of the bifurcating solutions on n but does not tell us their $(U_0, W_0)^{\mathrm{T}}$ values. The question of whether any of these bifurcating periodic solutions satisfy $U_0 = U_N = 0$ and hence solve the discrete BVP (4.1) will be answered in the next section.

4.2.2 Bifurcation diagram

In this section we consider the discrete boundary value problem (4.1) that gives the static equilibrium states of the mechanical system we are studying in this chapter. The discussion of the behaviour of the corresponding IVP (4.22) in the previous section will help us to understand how the solutions to the BVP arise and behave. We start by considering the bifurcations from the flat, zero solution analytically before moving onto a numerical inspection of the nonzero solutions and their bifurcations.

In the previous section we saw that the IVP (4.22) has periodic solutions with rotation number $\rho = p/q$ bifurcating from the zero fixed point at the λ values $\lambda = 2(1 - \cos(2\pi p/q))/\delta^2$. Here, we show that for specific values of p and q a necessary condition for bifurcation to occur from the zero solution to the discrete BVP (4.1) is satisfied before presenting numerical evidence that bifurcations do indeed occur at these λ values.

To do this we formulate the discrete BVP as a one dimensional bifurcation problem $g(W_0, \lambda) = 0$, where

$$g(W_0, \lambda) = (1, 0)\phi_\lambda^N((0, W_0)^{\mathrm{T}}) \equiv U_N(W_0, \lambda). \tag{4.28}$$

Standard bifurcation theory tells us that in order to have a bifurcation from the solution $W_0 = 0$ we require $\partial g/\partial W_0(0, \lambda) = 0$, the following proposition tells us at which λ values this occurs.

Proposition 4.5. *With $g(W_0, \lambda)$ defined by (4.28),*

$$\lambda = \lambda_{k,N} \equiv \frac{2}{\delta^2}\left(1 - \cos\frac{k\pi}{N}\right) \quad \textit{for} \quad k = 1, \ldots, N-1 \tag{4.29}$$

implies $\left.\frac{\partial g}{\partial W_0}\right|_{W_0=0} = 0$.

Proof. Let $\boldsymbol{K_n} = \frac{\partial \boldsymbol{X_n}}{\partial W_0}$, $\boldsymbol{e_1}^{\mathrm{T}} = (1, 0)$ and $\boldsymbol{e_2}^{\mathrm{T}} = (0, 1)$, then, using (4.1), we have $\boldsymbol{K_{n+1}} = \phi'(\boldsymbol{X_n})\boldsymbol{K_n}$ and $\boldsymbol{K_0} = \boldsymbol{e_2}$. Equation (4.28) then tells us that

$$\frac{\partial g}{\partial W_0} = \boldsymbol{e_1}^{\mathrm{T}}\boldsymbol{K_N}.$$

Since we are considering bifurcations from the zero solution, $W_0 = 0$, we can use $\phi'(\boldsymbol{X_n}) = \phi'(\boldsymbol{0})$ for all n to give

$$\left.\frac{\partial g}{\partial W_0}\right|_{W_0=0} = \boldsymbol{e_1}^{\mathrm{T}} A^N \boldsymbol{e_2}.$$

where $A = \phi'(\boldsymbol{0})$. From this we can see that if $\boldsymbol{e_2}$ is an eigenvector of A^N then $\partial g/\partial W_0 = 0$. We will now show that the condition that $\boldsymbol{e_2}$ is an eigenvector of A^N leads to the result.

For $0 < \lambda < 4/\delta^2$ we know from Section 4.2.1 (see also Figure 4.6) that the eigenvalues of A are given by

$$\mu_\pm = \mathrm{e}^{\pm 2\pi \mathrm{i}\theta} \quad \text{for} \quad \theta \in (0, \pi). \tag{4.30}$$

This means that in this parameter region the eigenvectors of A, $\boldsymbol{\nu_\pm}$, form a basis for

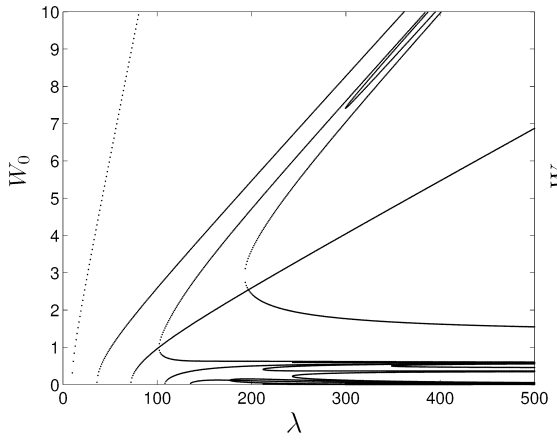

Figure 4.8: *The bifurcation diagram for the $N = 6$ discrete boundary value problem (4.1). Note the fixed point at the origin of the map ϕ is elliptic for $\lambda > 4/\delta^2 = 144$.*

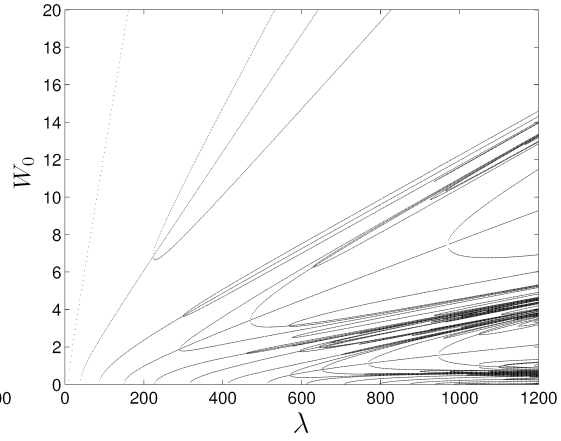

Figure 4.9: *The bifurcation diagram for the $N = 16$ discrete boundary value problem (4.1). Note the fixed point at the origin of the map ϕ is elliptic for $\lambda > 4/\delta^2 = 1024$.*

$\mathbb{R}^2$ allowing us to write $\boldsymbol{e_2} = a_1\boldsymbol{\nu_+} + a_1^*\boldsymbol{\nu_-}$ for some complex coefficient a_1. Applying A^N to this we find $A^N\boldsymbol{e_2} = a_1\mu_+^N\boldsymbol{\nu_+} + a_1^*\mu_-^N\boldsymbol{\nu_-}$. From this we see that for $\boldsymbol{e_2}$ to be an eigenvector of A^N we require $\mu_+^N = \mu_-^N$, and since $\det(A^N) = (\det(A))^N = 1$ and $\det(A^N) = \mu_+^N\mu_-^N$ we have $\mu_+^{2N} = 1$. This implies that $\mu_+ = \exp(\pi \mathrm{i} k/N)$ for $k \in \mathbb{Z}$, whilst the requirement (4.30) above restricts the range of k to $k = 1, \ldots, N-1$. Equation (4.25) for $\theta = \pi k/N$ with $k = 1, \ldots, N-1$ then gives the result. □

When bifurcations occur at the points found in the previous proposition the following proposition tells us that they are indeed periodic solutions to the IVP $\boldsymbol{X}_{n+1} = \phi(\boldsymbol{X_n})$.

Proposition 4.6. *Solutions to the BVP (4.1) with initial and final coordinates $\boldsymbol{X}_0 = (0, W_0)^{\mathrm{T}}$, $\boldsymbol{X}_N = (0, W_N)^{\mathrm{T}}$ are periodic solutions the corresponding IVP with minimal period less than or equal to N for $W_0 = W_N$ or $2N$ for $W_0 \neq W_N$.*

Proof. If $W_0 = W_N$ then $\boldsymbol{X_0} = \boldsymbol{X_N}$ and $\phi^N(\boldsymbol{X_0}) = \boldsymbol{X_N} = \boldsymbol{X_0}$ the result is clear. If $W_0 \neq W_N$ then the ρ_U reversibility of ϕ gives

$$\phi^{2N}(\boldsymbol{X_0}) = \phi^N(\boldsymbol{X_N}) = \phi^N(\rho_U(\boldsymbol{X_N})) = \rho_U(\phi^{-N}(\boldsymbol{X_N})) = \rho_U(\boldsymbol{X_0}) = \boldsymbol{X_0}$$

Thus the point $\boldsymbol{X_0}$ is on a periodic orbit of ϕ with minimal period less than or equal to $2N$. □

We have now seen that for the discrete boundary value problem (4.1) a necessary

condition for bifurcation from the flat, zero state is satisfied at the λ values $\lambda_{k,N}$ given by (4.29). Figures 4.8 and 4.9 show numerically computed global bifurcation diagrams for the discrete BVP (4.1) in the (λ, W_0) plane. We can see that there are $N-1$ bifurcations from the zero state ($W_0 = 0$), which do occur at the λ values give by (4.29). There are many solutions to the BVP shown in these diagrams, but these solutions are created by only a few different mechanisms (Domokos & Holmes (1993)).

- Pitchfork bifurcations on the zero solution branch arising when the eigenvalues of $\phi'(\mathbf{0})$ move through the roots of unity causing periodic solutions for the corresponding IVP to bifurcate from the fixed point at the origin. Behaviour analogous to this occurs also on the non-zero branches leading to secondary bifurcations. These can in principle occur at any λ value.

- Fold bifurcations seen towards the bottom right of figures 4.8 and 4.9 which are caused by a homoclinic tangle that appears in the phase space of the map ϕ for $\lambda > 4/\delta^2$ (see Section 4.2.1 and Hunt et al. (1997)).

- Fold bifurcations which can occur for $\lambda < 4/\delta^2$, for instance $(\lambda, W_0) \approx (900, 9)$ in Figure 4.9. It is suggested by Domokos & Holmes (1993) that these are due to tangling of the stable and unstable manifolds of non-zero hyperbolic higher period fixed points of the iterated map ϕ.

We now consider the solution shapes on the branches just described. Expression (4.27) from Section 4.2.1 allows us to write down the form of the solutions on the primary branches just after bifurcation from the zero solution:

$$\boldsymbol{X}_{\boldsymbol{n}}^{(\boldsymbol{k})} = W_0 \begin{pmatrix} \frac{-\delta}{\sin\frac{k\pi}{N}} \sin\left(\frac{nk\pi}{N}\right) \\ \cos\left(\frac{nk\pi}{N}\right) \end{pmatrix}. \tag{4.31}$$

Figure 4.10 shows some examples of the solutions to the discrete BVP generated by taking a slice through the bifurcation diagrams in figures 4.8 and 4.9 at the λ values $\lambda = 400$ and $\lambda = 600$ respectively[2]. These solutions are plotted in (x_i, y_i) space where $y_i = U_i$ and

$$x_0 = 0 \quad \text{and} \quad x_n = \sum_{i=1}^{n} \sqrt{\delta^2 - (U_i - U_{i-1})^2} \quad \text{for} \quad n = 1, \ldots, N.$$

[2]Plots similar to this, of buckled chain configurations, can also be seen in a dynamic model of protein folding (Mingaleev et al. (2002)) and the mechanical system discussed in Section 2.2 (Domokos & Holmes (1993))

The sinusoidal form of the bifurcating solutions (4.31) can be seen in several of the solutions in the top pane of Figure 4.10, for instance, look at the solutions with $W_0 \approx 18.6884$, $W_0 \approx 4.4997$ and $W_0 \approx 0.61098$. Also, an example of a secondary pitchfork bifurcation from a primary branch can be seen in the third to fifth solutions plotted in the top pane of Figure 4.10 (W_0 values approximately 7.5089, 7.2494 and 7.002). The central solution is symmetric about its central pivot whilst the solutions on the secondary branches either side of this solution have clearly broken this symmetry. In Figure 4.9 it is also possible to see further bifurcations on these secondary branches. These tertiary branches were predicted by Domokos & Holmes (1993) but not observed, and so this confirms that their prediction holds for this discrete BVP.

It is useful from a mechanical point of view to consider the behaviour of the end shortening, $\mathcal{E}_d = 1 - x_N$, of the solutions as the nondimensional load $p = 4/(\delta^2\lambda)$ is varied. On a branch of solutions the gradient of the function $p(\mathcal{E}_d)$ gives the stiffness of the system under axial compression, and this is shown in figures 4.11 and 4.12. We can see that all of the solutions appear to have negative stiffness and so the load they can support falls with increasing end shortening. Hence, in an experiment under controlled load once the buckling load is reached the system will simply crumple up. This is the physical reasoning behind the mathematical results presented in Section 5.2 of the next chapter that show that under controlled loading conditions all of the non-zero static equilibrium states are unstable. These solutions are not, however, physically uninteresting. Often experiments are performed under controlled end-shortening rather than controlled load, and it is seen in studies of continuum buckling models that controlling the end shortening (rigid loading) has a stabilising effect on solutions unstable under controlled loads (dead loading) (see for example Sandstede (1997), Peletier (2001), Wadee (2005)). Thus many of these solutions may well be stable and observable under rigid loading conditions.

To determine the most likely behaviour in a rigid loading experiment we consider the behaviour of the experimental apparatus. As described in (Thompson & Hunt 1984, p188-194) when performing an experiment under rigid loading conditions the loading apparatus and links in the mechanical system under study cannot have infinite stiffness. This means that the start of the experiment proceeds more like that of a dead loading experiment in which the load increases very quickly from zero for a very small end-shortening. The system will then buckle at the lowest buckling load. We thus predict an experimental scenario that unfolds via an initial distributed buckle pattern close to $p = 1$, shown in (a) of Figure 4.13. Then via secondary bifurcations this primary shape becomes asymmetric: (b) of Figure 4.13. Through further bifurcations, and increased

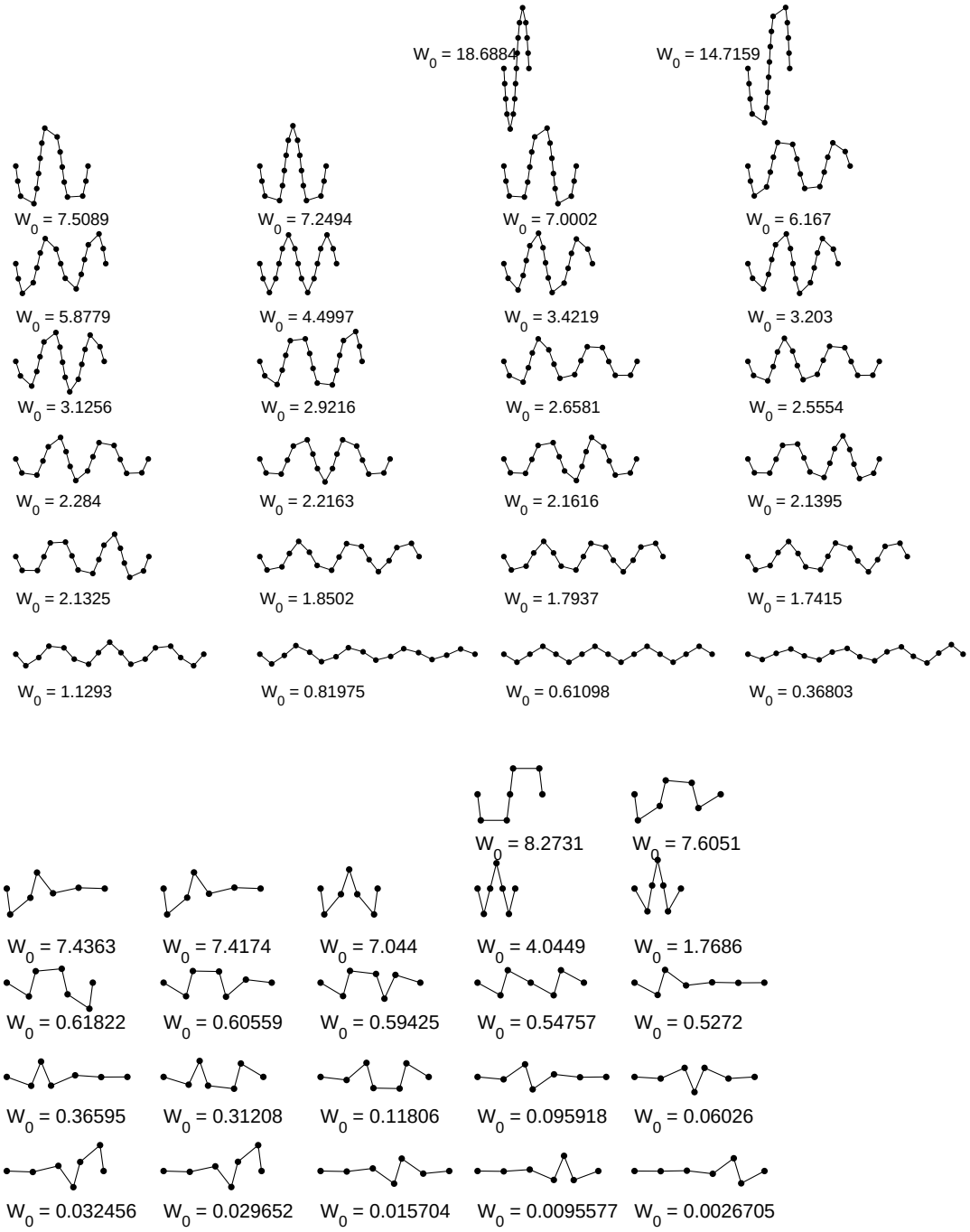

Figure 4.10: *Solutions from the bifurcation diagrams 4.8 (bottom) and 4.9 (top) at the λ values $\lambda = 300$ and $\lambda = 600$ respectively.*

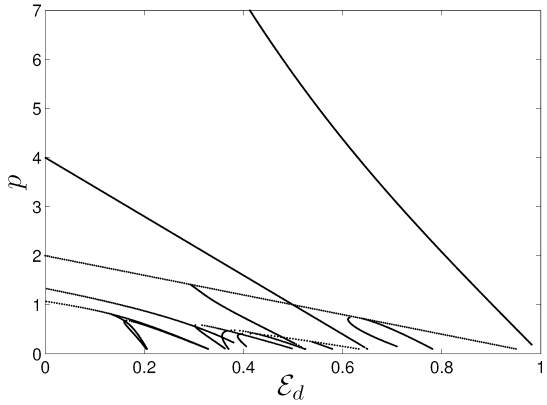

Figure 4.11: *The solution branches of the discrete BVP (4.1) with $N = 6$ shown in Figure 4.8 showing p as a function of the end shortening $\mathcal{E}_d$.*

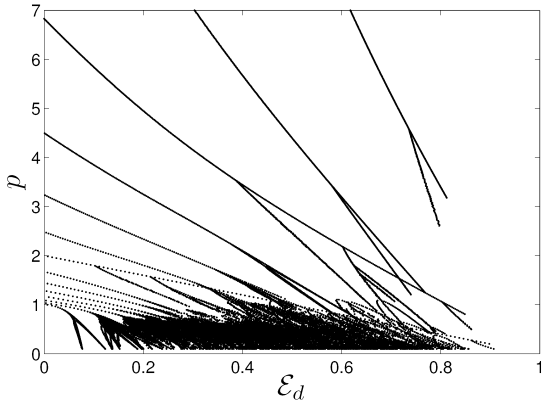

Figure 4.12: *The solution branches of the discrete BVP (4.1) with $N = 16$ shown in Figure 4.9 showing p as a function of the end shortening $\mathcal{E}_d$.*

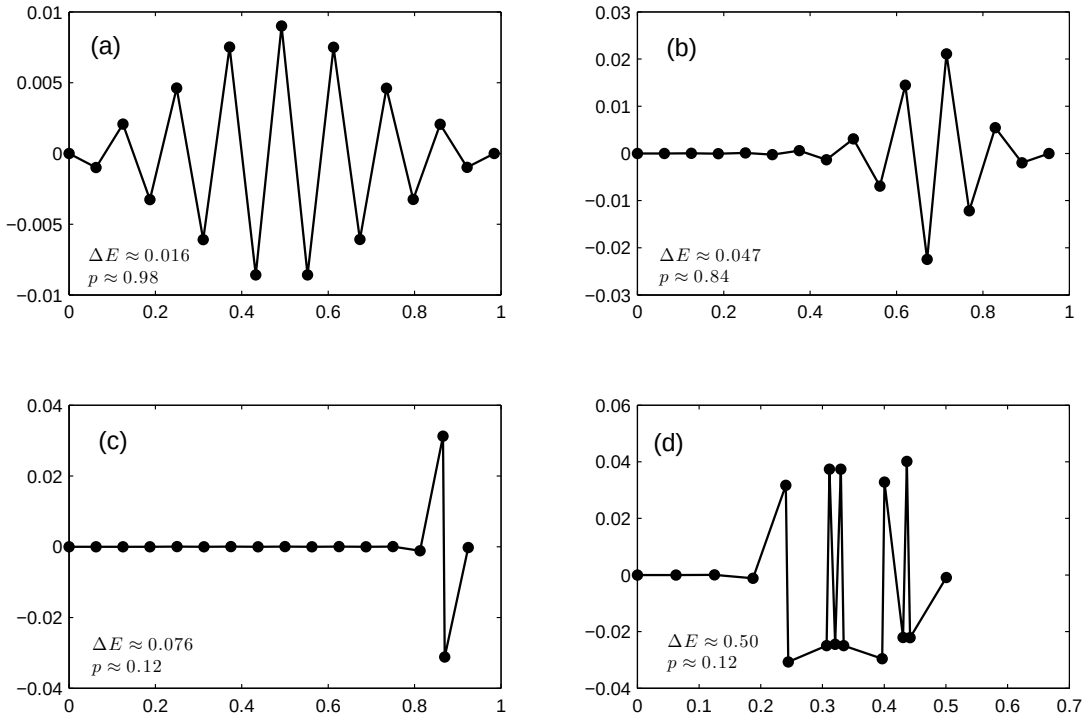

Figure 4.13: *Evolution of the static equilibrium states of the mechanical lattice of Figure 3.1 with $N = 16$ under increasing end shortening for small to moderate end shortening (a)-(c). (d) shows a spatially irregular state for a higher value of the lattice end shortening.*

end shortening, the displacement eventually localises at the end of the structure in a spatially localised solution: (c) of Figure 4.13. As the end shortening is increased from here we expect a jump to a child solution of the second primary branch before the chaos seen for larger end shortening values, seen in Figure 4.12, dictates the behaviour, making predicting experimental behaviour impossible. We do, however, expect the structure to move into spatially irregular states, an example of which is shown in panel (d) of Figure 4.13.

The behaviour just discussed differs considerably from the continuum limit of this system. From Figure 4.5 we see that the solution branches for the continuous BVP bifurcate at loads approaching zero. The scaling argument of the previous section tells us that solution with the lowest load for a given end shortening will be composed of infinitely many, infinitely small wrinkles. This singular behaviour is due to the lack of bending stiffness in the continuum model. In reality a continuous medium will have a finite bending stiffness giving a non-zero lowest buckling load (Hunt et al. (2000)).

The next sections prove some further properties of the bifurcation diagrams shown in figures 4.8 and 4.9.

4.2.3 Further branch properties

The main aim of this section is to present Proposition 4.9 that tells us which branches of solutions to the discrete boundary value problem satisfy $W_0(\lambda) \to \infty$ as $\lambda \to \infty$. We first show that the rotation number for a non-zero periodic solution to the IVP (4.22) can only change by deforming into a period two solution. We then see that this cannot occur for the solutions to the BVP (4.1). This then allows us to use the fact that ρ is conserved on branches of solutions to the BVP to prove in Proposition 4.9 that for BVP solutions with $\rho \in (0, 1/4)$ $W_0(\lambda) \to \infty$ as $\lambda \to \infty$. The numerical results of the previous section suggest that the divergence of the branches proved in Proposition (4.9) is linear and, finally in this section, a scaling argument adds weight to this numerical observation.

If we have a period q solution to the IVP (4.22) then $\boldsymbol{X_{n+q}} = \boldsymbol{X_n}$ for all n. This implies that the rotation number is the same for each point in the periodic solution and we call this the rotation number of the periodic solution. Proposition 4.6 of the previous section told us that all solutions to the BVP (4.1) are also periodic solutions to the discrete IVP and so we say that the rotation number for a particular BVP solution is equal to the rotation number of the corresponding IVP solution. The next proposition tells us that for any periodic solution to the IVP (4.22) with a rotation

number in the interval $(0, 1/2)$ the rotation number of the solution can only change along the solution branch if the solution deforms into a period two solution.

Proposition 4.7. *The rotation number for a non-zero periodic solution to the IVP (4.22) with $\rho \in (0, 1/2)$ cannot change unless it deforms into a solution with $\rho = 1/2$.*

Proof. The rotation number for a periodic solution to the IVP (4.22) is equivalent to the winding number of the polygon formed by taking the solution points $\boldsymbol{X_n}$ as vertices and connecting consecutive points with edges. For this winding number to change one of the edges or vertices must pass through the origin. If vertex n passes through the origin then $\boldsymbol{X_n} = (0, 0)^{\mathrm{T}}$ and $\phi(\boldsymbol{X_n}) = \boldsymbol{X_n}$ for all n since the origin is a fixed point of ϕ. This contradicts the assumption that the solution is non-zero. Now consider what happens when an edge passes through the origin: the continuous dependence of the periodic solution points, $\boldsymbol{X}_n$, on λ tells us that in this case

$$\boldsymbol{X}_{n+1} = a\boldsymbol{X}_n$$

for some $a \in \mathbb{R}^-$. It is now shown that this condition leads to a contradiction. The condition above implies that

$$\boldsymbol{X}_{n+1} = a\boldsymbol{X}_n \Rightarrow \phi(\boldsymbol{X}_n) = a\boldsymbol{X}_n \Rightarrow \det(\phi'(\boldsymbol{X}_n)) = a^2.$$

Since ϕ is an area preserving map $\det(\phi'(\boldsymbol{X}_n)) = 1$ (Lemma 4.2, p. 66), and so $a = \pm 1$. Consider these two cases separately

$a = +1$: In this case $\phi(\boldsymbol{X}_n) = \boldsymbol{X}_n$ and so $\boldsymbol{X}_n$ is a fixed point of the map ϕ. Since ϕ has a unique fixed point $\boldsymbol{X}_n = \boldsymbol{0}$ for all n contradicting the assumption that $\boldsymbol{X_n}$ is non-zero.

$a = -1$: This implies that $\phi(\boldsymbol{X}_n) = -\boldsymbol{X}_n$ and so $\phi(\phi(\boldsymbol{X}_n)) = \phi(-\boldsymbol{X}_n) = -\phi(\boldsymbol{X}_n) = \boldsymbol{X}_n$. i.e. $\boldsymbol{X}_n$ is a period two fixed point of the map ϕ and $\rho = 1/2$.

Therefore for the rotation number to change the solution must deform into a solution with $\rho = 1/2$. □

We now show that the IVP (4.22) has a unique period two solution that does not satisfy $U_0 = U_N = 0$ and so cannot solve the BVP (4.1).

Proposition 4.8. *The IVP (4.22) has a unique period two fixed point for $\lambda > 4/\delta^2$. This period two fixed point is given by $\boldsymbol{X}_+ = (U_+, 0)^{\mathrm{T}}$ and $\boldsymbol{X}_- = (U_-, 0)^{\mathrm{T}}$ where*

$$U_\pm = \pm\sqrt{\frac{\delta^4\lambda^2 - 16}{4\delta^2\lambda^2}}.$$

Proof. The condition that $\boldsymbol{X}_+$ and $\boldsymbol{X}_-$ form a period two solution to the IVP (4.22) is that $\boldsymbol{X}_+ = \phi(\boldsymbol{X}_-)$ and $\boldsymbol{X}_- = \phi(\boldsymbol{X}_+)$. Writing this out in component form using (4.2) gives

$$U_+ = U_- - \delta g\left(W_- + \frac{\delta\lambda U_-}{2}\right) \quad (4.32a) \qquad U_- = U_+ - \delta g\left(W_+ + \frac{\delta\lambda U_+}{2}\right) \quad (4.32c)$$

$$W_+ = W_- + \frac{\delta\lambda}{2}(U_+ + U_-) \quad (4.32b) \qquad W_- = W_+ + \frac{\delta\lambda}{2}(U_- + U_+) \quad (4.32d)$$

where $g(x) = x/\sqrt{1+x^2}$. Equations (4.32b) and (4.32d) imply that

$$W_+ - W_- = \frac{\delta\lambda}{2}(U_- + U_+) \quad \text{and} \quad -(W_+ - W_-) = \frac{\delta\lambda}{2}(U_- + U_+),$$

and so we must have $U_- = -U_+$ and $W_+ = W_-$. These results, along with equations (4.32a) and (4.32c), and a little algebra imply that

$$W_- = \frac{-\delta\lambda}{2}U_- + g^{-1}\left(\frac{2U_0}{\delta}\right) \quad \text{and} \quad W_- = -\left(\frac{-\delta\lambda}{2}U_- + g^{-1}\left(\frac{2U_0}{\delta}\right)\right)$$

where $g^{-1}(x) = x/\sqrt{1-x^2}$. This tells us that $W_\pm = 0$. After some more algebra this leads to the result

$$U_\pm^2 = \frac{\delta^4\lambda^2 - 16}{4\delta^2\lambda^2}.$$

□

These previous two propositions show that the rotation number of a solution to the BVP cannot change. This is because for the rotation number of the BVP solution to change the rotation number of the corresponding periodic IVP solution has to change, and this can only occur if the IVP solution deforms into a period two solution. There are no period two solutions to the IVP that satisfy the BVP and so the rotation number of a BVP solution cannot change. We now use this to prove the following proposition.

Proposition 4.9. *A solution branch to the BVP (4.1) given by $(\lambda, W_0(\lambda))$ with $W_0(\lambda) > 0$ and rotation number $\rho \in (0, \frac{1}{4})$ satisfies $W_0(\lambda) \to \infty$ as $\lambda \to \infty$.*

Proof. This follows the proof of Proposition 4.7 in Domokos & Holmes (1993).

The linearised solutions are rotations through $\pi n/N$ radians and so close enough to the bifurcation points, say $\lambda = \lambda_1$, for $\rho \in (0, \frac{1}{4})$ we have $U_2(\lambda_1) < 0$. We now prove that $U_2(\lambda) < 0$ for all $\lambda > \lambda_{n,N}$ and proceed by contradiction. Suppose that for some $\bar{\lambda} > \lambda_{n,N}$ $U_2(\bar{\lambda}) > 0$. Then we have $U_2(\lambda_1) < 0$ and $U_2(\bar{\lambda}) > 0$ and so by the intermediate value theorem we know there exists a $\lambda^* \in (\lambda_1, \bar{\lambda})$ such that $U_2(\lambda^*) = 0$. But with $U_2(\lambda^*) = 0$ we have $\boldsymbol{X_0} = (0, W_0)^{\mathrm{T}}$ and $\boldsymbol{X_2} = (0, W_2)^{\mathrm{T}}$ which means that the orbit is a solution to the BVP with rotation number $\rho = 1/4$. This contradicts our assumption that $\rho \in (0, 1/4)$ and so $U_2(\lambda) < 0$ for all $\lambda > \lambda_{n,N}$.

From the definition of ϕ and the condition $X_0 = (0, W_0^{\mathrm{T}})$ we have

$$U_2 = -\delta(g(W_0) + g(W_0 - \delta^2 \lambda g(W_0)))$$

where $g(x) = x/\sqrt{1+x^2}$. The condition $U_2 < 0$, after some algebra, leads to

$$2\sqrt{1 + W_0^2} > \delta^2 \lambda.$$

Therefore, as $\lambda \to \infty$ we must have $W_0 \to \infty$ at constant δ. □

From figures 4.8 and 4.9 we expect the divergence of solution branches proved in the above proposition to be linear. The following scaling argument lends weight to this numerical observation.

For large $W_i + \delta\lambda U_i/2$ the map ϕ can be written

$$\begin{pmatrix} U_{i+1} \\ W_{i+1} \end{pmatrix} = \begin{pmatrix} U_i - \delta \mathrm{sign}(W_i + \frac{\delta\lambda}{2} U_i) \\ W_i + \frac{\delta\lambda}{2}(U_i + U_{i+1}) \end{pmatrix} + \mathcal{O}\left(\left(W_i + \frac{\delta\lambda}{2} U_i\right)^{-2}\right).$$

If, in this expression, we then perform the scaling

$$\bar{U}_i = U_i, \quad b\bar{W}_i = W_i, \quad b\bar{\lambda} = \lambda$$

with $b > 0$, we notice that it is invariant under this scaling. Thus, if we have a particular solution to the BVP (4.1), given by $(U_i(\lambda), W_i(\lambda))^{\mathrm{T}}$ for $i = 0, \ldots, N$, for which $W_i + \delta\lambda U_i/2$ is large for all i we can construct a whole set of solutions $(\bar{U}_i(\bar{\lambda}), \bar{W}_i(\bar{\lambda}))^{\mathrm{T}}$ that satisfy

$$\bar{W}_i(\bar{\lambda}) = \frac{W_i(\lambda)}{\lambda} \bar{\lambda}.$$

This gives us a branch of solutions with $\bar{W}_i$ and $\bar{\lambda}$ linearly related.

4.2.4 Secondary bifurcations

In Figure 4.9 it is possible to see secondary bifurcations on some of the primary branches of solutions to the discrete BVP (4.1). Here we derive the λ values at which we expect secondary bifurcations on the $n = N/2$ or $\rho = 1/4$ branch, when N is even. This result is made possible by the symmetry properties of this particular branch. Before this, some symmetry properties of the Jacobian of ϕ, $\phi'(\boldsymbol{X})$, are presented which allow the derivation of analytic expressions for the solutions on the $\rho = 1/4$ branch.

Lemma 4.2. *The Jacobian of the map ϕ, $\psi = \phi'$ satisfies the following properties for all X in $\mathbb{R}^2$*

1. *Symplecticity: $\psi^T J \psi = J$ where $J = \begin{pmatrix} 0 & 1 \\ -1 & 0 \end{pmatrix}$*
2. *$\psi_{-\delta}(\rho_U(X)) = [\psi_\delta(X)]^{-1}$*
3. *$\psi(-X) = \psi(X)$*
4. *Transformation invariance: $\psi(AX) = \psi(X)$ where A is an operator in $\mathbb{R}^2$ than preserves $W + \frac{\delta\lambda}{2}U$*
5. *Eigenvalues: The eigenvalues of ψ are given by*

$$\lambda_\pm = \frac{1}{2\beta}\left(2\beta - \delta^2\lambda \pm \sqrt{\delta^4\lambda^2 - 4\delta^2\lambda\beta}\right) \tag{4.33}$$

where $\beta = (1 + (W + \frac{\delta\lambda U}{2})^2)^{\frac{3}{2}}$.

Proof. From (4.23) (p. 51) we have

$$\psi = \begin{pmatrix} 1 - \frac{\delta^2\lambda}{2\beta} & \frac{-\delta}{\beta} \\ \delta\lambda - \frac{\delta^3\lambda^2}{4\beta} & 1 - \frac{\delta^2\lambda}{2\beta} \end{pmatrix} \tag{4.34}$$

where $\beta = (1 + (W + \frac{\delta\lambda U}{2})^2)^{\frac{3}{2}}$. Parts 1, 2 and 3 can be proved by direct evaluation. To prove 4 notice that if $W + \frac{\delta\lambda}{2}U$ is preserved then β and thus ψ is unchanged. Part 5 can be derived from by applying the quadratic formula to the characteristic polynomial of ψ

$$\lambda^2 + \frac{\delta^2\lambda - 2\beta}{\beta}\lambda + 1.$$

□

Proposition 4.10. *For N even, the BVP (4.1) has a solution with $\rho = 1/4$ that exists for $\lambda \in (2/\delta^2, \infty)$ with solution points*

$$\boldsymbol{X_{4n}} = \begin{pmatrix} 0 \\ W_0 \end{pmatrix} \quad \boldsymbol{X_{4n+1}} = \begin{pmatrix} -\delta g(W_0) \\ 0 \end{pmatrix}$$
$$\boldsymbol{X_{4n+2}} = -\boldsymbol{X_{4n}} \quad \boldsymbol{X_{4n+3}} = -\boldsymbol{X_{4n+1}}$$

$$W_0 = \sqrt{\frac{\delta^4\lambda^2}{4} - 1}, \quad g(x) = \frac{x}{\sqrt{1+x^2}}.$$

Proof. We will assume the above form of the function $W_0(\lambda)$ and show that this gives a solution to the BVP for all $\lambda \in (2/\delta^2, \infty)$. With $U_0 = 0$ we have from the definition of ϕ that

$$\begin{aligned} U_1 &= -\delta g(W_0) \quad \text{and so} \\ W_1 &= W_0 + \frac{\delta\lambda}{2}U_1 = W_0 - \frac{\delta^2\lambda}{2}g(W_0) \\ &= \sqrt{\frac{\delta^4\lambda^2}{4} - 1} - \frac{\delta^2\lambda}{2}g\left(\sqrt{\frac{\delta^4\lambda^2}{4} - 1}\right) \\ &= 0. \end{aligned}$$

Since $W_1 = 0$ we have $\boldsymbol{X_1} \in \mathrm{Fix}(\rho_W)$ and the ρ_W reversibility of ϕ gives

$$\boldsymbol{X_2} = \phi(\boldsymbol{X_1}) = \phi \circ \rho_W(\boldsymbol{X_1}) = \rho_W \circ \phi^{-1}(\boldsymbol{X_1}) = \rho_W(\boldsymbol{X_0}) = -\boldsymbol{X_0}.$$

Similarly,

$$\boldsymbol{X_3} = \phi(\boldsymbol{X_2}) = \phi \circ \rho_U(\boldsymbol{X_2}) = \rho_U \circ \phi^{-1}(\boldsymbol{X_2}) = \rho_U(\boldsymbol{X_1}) = -\boldsymbol{X_1}.$$

The expression for W_0 has real solutions for

$$\frac{\delta^4\lambda^2}{4} > 1 \quad \Rightarrow \quad \lambda > \frac{2}{\delta^2}.$$

To find the rotation number ρ for this solution we notice that the angles the solution points $\boldsymbol{X_n}$ make with the positive U axis are given by $\Theta_n = (n+1)\pi/2$ and so

$$\rho = \frac{1}{2\pi}\lim_{n\to\infty}\frac{\Theta_n - \Theta_0}{n} = \frac{1}{4}.$$

This proves that the IVP has a $\rho = 1/4$ periodic solution with the given solution points.

That this IVP solution solves the BVP for N even follows from the fact that $U_{2n} = 0$ for all $n \in \mathbb{Z}$. □

The ability to determine the λ values at which we expect secondary bifurcations on this branch rests in the fact, presented in the next lemma, that the Jacobians of ϕ evaluated at each point in a solution on this branch are equal.

Lemma 4.3. *Let $\boldsymbol{X_n}$ for $n = 0, \ldots, N$ be the solution found in Lemma 4.10, then $\phi'(\boldsymbol{X_n}) = \phi'(\boldsymbol{X_0})$ for $n = 1, \ldots, N$.*

Proof. For any solution we have $\boldsymbol{X_N} = (0, W_N)^{\mathrm{T}}$ and $\boldsymbol{X_N} = \phi(\boldsymbol{X_{N-1}})$ which implies

$$\begin{aligned} W_N &= W_{N-1} + \frac{\delta\lambda}{2}(U_{N-1} + U_N) \\ W_N &= W_{N-1} + \frac{\delta\lambda}{2}U_{N-1} \\ W_N + \frac{\delta\lambda}{2}U_N &= W_{N-1} + \frac{\delta\lambda}{2}U_{N-1}. \end{aligned}$$

From Lemma 4.2 we know that $\phi'(\boldsymbol{X})$ is invariant on curves of constant $W + \frac{\delta\lambda}{2}U$ and so the above result implies that $\phi'(\boldsymbol{X_N}) = \phi'(\boldsymbol{X_{N-1}})$.

Now, since $\boldsymbol{X_2} = -\boldsymbol{X_0}$, the fact that $\phi'(-\boldsymbol{X}) = \phi'(\boldsymbol{X})$ (Lemma 4.2) implies that $\phi'(\boldsymbol{X_2}) = \phi'(\boldsymbol{X_0})$. The argument given above for $\phi'(\boldsymbol{X_N}) = \phi'(\boldsymbol{X_{N-1}})$ for $\boldsymbol{X_2}$ implies $\phi'(\boldsymbol{X_2}) = \phi'(\boldsymbol{X_{N-1}})$ and so we have $\phi'(\boldsymbol{X_0}) = \phi'(\boldsymbol{X_n})$ for $n = 1, 2, 3$. The result follows from the fact that this solution is periodic with period four when we view $\boldsymbol{X_{n+1}} = \phi(\boldsymbol{X_n})$ as an IVP. □

In Section 4.2.2 solutions to the discrete BVP were put in a one to one correspondence with a one dimensional bifurcation problem $g(W_0(\lambda), \lambda) = 0$ (4.28). When the condition $\partial_{W_0} g(W_0(\lambda), \lambda) = 0$ is satisfied we expect a bifurcation on the branch $W_0(\lambda)$. In the next proposition it is shown that this condition is satisfied at $N/2 - 1$ points on the solution branch just determined in Proposition 4.10.

Proposition 4.11. *We expect there to be $N/2 - 1$ bifurcations on the primary branch of solutions given in Proposition (4.10) at the λ values*

$$\lambda_{k,N}^2 = \frac{4}{\delta^4(1 - \cos\frac{k\pi}{N})} \text{ for } k = 1, 2, \ldots, \frac{N}{2} - 1.$$

Proof. Using the bifurcation formulation of Section 4.2.2 we expect bifurcations from the branch $W_0(\lambda)$ of the system $g(W_0, \lambda) = 0$ (4.28) when $\frac{\partial g}{\partial W_0} = 0$. From (4.28) and

the recent result in Lemma 4.3 we have

$$\frac{\partial g}{\partial W_0} = (1\ 0)\phi'(X_0)^N \begin{pmatrix} 0 \\ 1 \end{pmatrix}.$$

The reasoning of Proposition 4.5 holds here also and so we have

$$\frac{\partial g}{\partial W_0} = 0 \Leftrightarrow \mu = \mathrm{e}^{\frac{k\pi i}{N}} \text{ for } k = 1, 2, \ldots, N-1$$

where μ is one of the eigenvalue pair of $\phi'(\boldsymbol{X_0})$. From the expression for the eigenvalues of $\phi'(\boldsymbol{X})$ in Lemma (4.2) we have

$$\begin{aligned} \frac{1}{2\beta}\left(2\beta - \delta^2\lambda + \sqrt{\delta^4\lambda^2 - 4\delta^2\lambda\beta}\right) &= \mathrm{e}^{\frac{k\pi i}{N}} \\ \Rightarrow 1 - \frac{\delta^2\lambda}{2\beta} &= \cos\frac{k\pi}{N} \end{aligned}$$

where $\beta = \left(1 + \left(W + \frac{\delta\lambda}{2}U\right)^2\right)^{\frac{3}{2}}$. On the $\rho = 1/4$ branch we have $W_0 = \sqrt{\frac{\delta^4\lambda^2}{4} - 1}$ and so then $\beta = \left(\frac{\delta^2\lambda}{2}\right)^3$ and

$$\begin{aligned} 1 - \frac{4}{\delta^4}\lambda &= \cos\frac{k\pi}{N} \\ \Rightarrow \lambda^2 &= \frac{4}{\delta^4\left(1 - \cos\frac{k\pi}{N}\right)}. \end{aligned}$$

At this point the range of k is $1, 2, \ldots, N-1$, but we now notice that the primary branch we are considering only exists for $\lambda > \lambda^*_{N/2,N} = 2/\delta^2$. This gives us the additional requirement

$$\begin{aligned} \frac{4}{\delta^4\left(1 - \cos\frac{k\pi}{N}\right)} &> \frac{4}{\delta^2} \\ \Rightarrow \cos\frac{k\pi}{N} &> 0 \\ \Rightarrow 0 < k &< \frac{N}{2}. \end{aligned}$$

Since N is even we have $N/2 - 1$ integer values for which this is true. □

4.2.5 Solution symmetries

This section presents and proves the symmetry relations between solutions and the symmetry invariants of the solutions to the discrete BVP (4.1). In order to discuss the symmetries of the solutions to the discrete BVP we now introduce some symmetry operations that act on a whole BVP solution $\Gamma = \{\boldsymbol{X_0}, \ldots, \boldsymbol{X_N}\}$. These operations are:

$\boldsymbol{R}$: This transformation reverses the order of the solution points, i.e.

$$R(\Gamma) = \{\boldsymbol{X_N}, \ldots, \boldsymbol{X_0}\}, \text{ equivalently, } R : X_i \to X_{N-i} \text{ for } i = 0, 1, \ldots, N.$$

$\boldsymbol{T_{N/2}}$: For N even with $\boldsymbol{X_0} = \boldsymbol{X_N}$, this transformation translates the solution by $N/2$ lattice points and takes care of the end points, i.e.

$$T_{N/2}(\Gamma) = \{\boldsymbol{X_{N/2}}, \ldots, \boldsymbol{X_N}, \boldsymbol{X_1}, \ldots, \boldsymbol{X_{N/2}}\}.$$

$\boldsymbol{\bar{\rho}_{U,W}}$: This transformation reflects the solution about the W (for ρ_U) or U (for ρ_W), axis in the phase space of the map ϕ, i.e.

$$\bar{\rho}_{U,W} : X_i \to \rho_{U,W}(X_i) \text{ for } i = 0, 1, \ldots, N.$$

The first table of Figure 4.14 summarises the solution symmetry relations that are proved in the next few propositions. The plots in this table show, for each type of solution specified by the values of N, W_0 and W_N, a schematic example of that type of solution in the (U, W) phase plane of the map ϕ. The solutions denoted by different colours and symbols are the solutions related by symmetry, as shown in the following propositions. The second table of Figure 4.14 shows the symmetry invariants of the various solutions shown in the first table of Figure 4.14.

Although we are discussing these symmetries in the context of the specific mechancial system of this chapter the proofs of the following propositions only rely on a few symmetry properties of the map ϕ. These symmetries are the ρ_W and ρ_U reversibility of ϕ described on p. 50. Both of these symmetries rely on the self adjoint of ϕ (see Section 3.1.1) which resulted from the choice $\beta = 1/2$ in Section 3.2.3. If we now consider the general lattice potential (3.1) p. 25, the ρ_U and ρ_W reversibilities are consequences of the properties $v'(-x) = -v'(x)$ and $w'(-x) = -w'(x)$ respectively, where v and w are the potential functions that define our general lattice. This means that the following symmetry relations will hold in any lattice that satisfies these conditions.

	Solution invariants	Size of solution group	Relevant proposition
①	$\bar{\rho}_U \circ R$	2	Proposition 4.14
②	$\bar{\rho}_W \circ R$	2	Proposition 4.13
③	None	4	Proposition 4.12
④	$\bar{\rho}_U \circ R$	4	Proposition 4.15

Figure 4.14: *The solution groups and solution invariants of the discrete BVP (4.1). The vertical axis on the plots above is W_n and the horizontal axis is U_n. Each plot gives a schematic representation of a BVP solution in the relevant symmetry category.*

Proposition 4.12. *Let* $\Gamma_1 = \{\boldsymbol{X_0}, \ldots, \boldsymbol{X_N}\}$ *be a solution to the discrete BVP (4.1) with* $\boldsymbol{X_0} = (0, W_0)^{\mathrm{T}}$ *and* $\boldsymbol{X_N} = (0, W_N)^{\mathrm{T}}$ *where* $W_0 > 0$ $W_N < 0$ *and* $W_0 \neq -W_N$. *Then there is a group of four solutions related by the transformations given in the following table.*

Solution	Γ_1	Γ_2	Γ_3	Γ_4
Γ_1	***i.d.***	$\bar{\rho}_U \circ \bar{\rho}_W$	$\bar{\rho}_W \circ R$	$\bar{\rho}_U \circ R$
Γ_2		***i.d.***	$\bar{\rho}_U \circ R$	$\bar{\rho}_W \circ R$
Γ_3			***i.d.***	$\bar{\rho}_U \circ \bar{\rho}_W$
Γ_4				***i.d.***

The symbol ***i.d.*** *represents the identity transformation. (Each of the transformations in the above table commutes, and is an involution, and so only the upper right triangle of the table is required. Also, the order the transformations are applied does not matter, e.g.* $\Gamma_1 = \bar{\rho}_U \circ \bar{\rho}_W(\Gamma_2)$ *and* $\Gamma_2 = \bar{\rho}_U \circ \bar{\rho}_W(\Gamma_1)$. *)*

Proof. All of the transformations in the table above commute and so we need only proof that Γ_2, Γ_3 and Γ_4 are solutions given that Γ_1 is a solution to the discrete BVP. The remaining transformation properties can be found by transforming via solution Γ_1. To prove that Γ_i is a solution we need to show that $\boldsymbol{e_1}^{\mathrm{T}}\boldsymbol{X_0^{(i)}} = 0$, $\boldsymbol{e_1}^{\mathrm{T}}\boldsymbol{X_N^{(i)}} = 0$ and $\boldsymbol{X_{n+1}^{(i)}} = \phi(\boldsymbol{X_n^{(i)}})$. Since the transformations $\bar{\rho}_U$ and $\bar{\rho}_W$ map points, $\boldsymbol{X}$, with $\boldsymbol{e_1}^{\mathrm{T}}\boldsymbol{X} = 0$ onto points that also satisfy this condition, and the transformation R swaps $\boldsymbol{X_0}$ with $\boldsymbol{X_N}$, the first two conditions are satisfied for Γ_2, Γ_3 and Γ_4. We now prove that $\boldsymbol{X_{n+1}^{(i)}} = \phi(\boldsymbol{X_n^{(i)}})$ for $i = 2, 3, 4$ given that this holds for $i = 1$ using the ρ_U and ρ_W reversibility of ϕ.

Γ_2**:** Consider $\boldsymbol{X_{i+1}^{(2)}}$:

$$\begin{aligned}\boldsymbol{X_{i+1}^{(2)}} = \rho_U \circ \rho_W(\boldsymbol{X_{i+1}^{(1)}}) &= \rho_U \circ \rho_W \circ \phi(\boldsymbol{X_i^{(1)}}) \\ &= \rho_U \circ \phi^{-1} \circ \rho_W(\boldsymbol{X_i^{(1)}}) = \phi \circ \rho_U \circ \rho_W(\boldsymbol{X_i^{(1)}}) = \phi(\boldsymbol{X_i^{(2)}}).\end{aligned}$$

Γ_3**:** Consider $\boldsymbol{X_{i+1}^{(3)}}$:

$$\boldsymbol{X_{i+1}^{(3)}} = \rho_U(\boldsymbol{X_{N-(i+1)}^{(1)}}) = \rho_U \circ \phi^{-1}(\boldsymbol{X_{N-i}^{(1)}}) = \phi \circ \rho_U(\boldsymbol{X_{N-i}^{(1)}}) = \phi(\boldsymbol{X_i^{(3)}}).$$

Γ_4**:** This is the same as for Γ_2 with ρ_U and $\boldsymbol{X_i^{(4)}}$ in place of ρ_W and $\boldsymbol{X_i^{(3)}}$.

□

Proposition 4.13. *Let* $\Gamma = \{\boldsymbol{X_0}, \ldots, \boldsymbol{X_N}\}$ *be a solution to the BVP (4.1) that satisfies* $W_0 = -W_N$*. Then* $\bar{\rho}_W \circ R(\Gamma) = \Gamma$ *and* $\bar{\Gamma} = \bar{\rho}_U \circ R(\Gamma)$ *is also a solution to the BVP.*

Proof. First we show that the solution Γ is invariant under $\bar{\rho}_W \circ R$. To show this we need to show that $\boldsymbol{X_n} = \rho_W(\boldsymbol{X_{N-n}})$ for $n = 0, \ldots, N$. Consider the following

$$\begin{aligned}\rho_W(\boldsymbol{X_{N-n}}) &= \rho_W \circ \phi^{-n}(\boldsymbol{X_N}) = \rho_W \circ \phi^{-n} \circ \rho_W(\boldsymbol{X_0}) \\ &= \rho_W \circ \phi^{-n+1} \circ \rho_W \circ \phi(\boldsymbol{X_0}) = \cdots = \rho_W \circ \rho_W \circ \phi^n(\boldsymbol{X_0}) = \boldsymbol{X_n}, \quad (4.35)\end{aligned}$$

which proves that $\bar{\rho}_W \circ R(\Gamma) = \Gamma$.

Now we show that $\bar{\Gamma} = \bar{\rho}_U \circ R(\Gamma)$, equivalently $\bar{\boldsymbol{X}}_{\boldsymbol{n}} = \rho_U(\boldsymbol{X_{N-n}})$, is a solution to the discrete BVP. To show this we need to show that $\boldsymbol{e_1}^{\mathrm{T}}\bar{\boldsymbol{X}}_{\boldsymbol{0}} = 0$, $\boldsymbol{e_1}^{\mathrm{T}}\bar{\boldsymbol{X}}_{\boldsymbol{N}} = 0$ and $\bar{\boldsymbol{X}}_{\boldsymbol{n+1}} = \phi(\bar{\boldsymbol{X}}_{\boldsymbol{n}})$. Now, $\bar{\boldsymbol{X}}_{\boldsymbol{0}} = \rho_U(\boldsymbol{X_N}) = \boldsymbol{X_N}$ hence $\boldsymbol{e_1}^{\mathrm{T}}\bar{\boldsymbol{X}}_{\boldsymbol{0}} = 0$. Similarly, $\bar{\boldsymbol{X}}_{\boldsymbol{N}} = \rho_U(\boldsymbol{X_0}) = \boldsymbol{X_0}$ hence $\boldsymbol{e_1}^{\mathrm{T}}\bar{\boldsymbol{X}}_{\boldsymbol{N}} = 0$. To check the third condition, consider

$$\bar{\boldsymbol{X}}_{\boldsymbol{n+1}} = \rho_U(\boldsymbol{X_{N-(n+1)}}) = \rho_U \circ \phi^{-1}(\boldsymbol{X_{N-n}}) = \phi \circ \rho_U(\boldsymbol{X_{N-n}}) = \phi(\bar{\boldsymbol{X}}_{\boldsymbol{n}}).$$

Hence $\bar{\Gamma}$ is also a solution to the discrete BVP (4.1). □

Proposition 4.14. *Let* $\Gamma = \{\boldsymbol{X_0}, \ldots, \boldsymbol{X_N}\}$ *be a solution to the BVP (4.1) that satisfies* $W_0 = W_N$*. Then* $\bar{\rho}_U \circ R(\Gamma) = \Gamma$ *and* $\bar{\Gamma} = \bar{\rho}_W \circ R(\Gamma)$ *is also a solution to the BVP.*

Proof. The proof that $\bar{\rho}_U \circ R(\Gamma) = \Gamma$ is the same as the first part of the proof in Proposition 4.13 with ρ_W replaced with ρ_U, and so we do not repeat it here. Similarly the proof that $\bar{\Gamma} = \bar{\rho}_W \circ R(\Gamma)$ is a solution to the BVP is the same as in the second half of the proof of Proposition 4.13 with ρ_U replaced with ρ_W. □

Proposition 4.15. *Let* $\Gamma = \{\boldsymbol{X_0}, \ldots, \boldsymbol{X_N}\}$ *be a solution to the discrete BVP (4.1) with* N *even,* $W_0 = W_N$ *and* $W_0 \neq W_{N/2}$*. Then there is a group of four solutions to the discrete BVP related by the transformations in the following table.*

Solution	Γ_1	Γ_2	Γ_3	Γ_4
Γ_1	***i.d.***	$\bar{\rho}_U \circ \bar{\rho}_W$	$T_{N/2}$	$\bar{\rho}_U \circ \bar{\rho}_W \circ T_{N/2}$
Γ_2		***i.d.***	$\bar{\rho}_U \circ \bar{\rho}_W \circ T_{N/2}$	$T_{N/2}$
Γ_3			***i.d.***	$\bar{\rho}_U \circ \bar{\rho}_W$
Γ_4				***i.d.***

Proof. We first prove that if N is even and $\boldsymbol{e_1}^{\mathrm{T}}\boldsymbol{X_0} = 0$ then $\boldsymbol{e_1}^{\mathrm{T}}\boldsymbol{X_{N/2}} = 0$. Consider the following:

$$\boldsymbol{X_n} = \phi^n(\boldsymbol{X_0}) = \phi^n \circ \rho_U(\boldsymbol{X_0}) = \rho_U \circ \phi^{-n}(\boldsymbol{X_N}) = \rho_U(\boldsymbol{X_{N-n}}),$$

this tells us that the BVP solutions Γ_i satisfy $\bar{\rho}_U \circ R(\Gamma_i) = \Gamma_i$ and also, taking this expression for $n = N/2$, that $\boldsymbol{e_1}^{\mathrm{T}}\boldsymbol{X_{N/2}} = 0$. With this and some of the reasoning from Proposition 4.12, we can see that $\boldsymbol{e_1}^{\mathrm{T}}\boldsymbol{X}^{(i)}_{\boldsymbol{0,N}} = 0$ for $i = 2, 3, 4$. The condition that $W_0 \neq W_{N/2}$ ensures that the four solutions given above are distinct.

We now prove $\boldsymbol{X}^{(i)}_{\boldsymbol{n+1}} = \phi(\boldsymbol{X}^{(i)}_{\boldsymbol{n}})$ for $i = 2, 3, 4$. The proof that Γ_2 from Proposition 4.12 satisfies this relation holds here. If $\boldsymbol{X}^{(i)}_{\boldsymbol{n+1}} = \phi(\boldsymbol{X}^{(i)}_{\boldsymbol{n}})$ then $\boldsymbol{X}^{(i)}_{\boldsymbol{n+1+m}} = \phi(\boldsymbol{X}^{(i)}_{\boldsymbol{n+m}})$ for any $m \in \mathbb{Z}$ where the indices are computed mod N and so Γ_3 and Γ_4 also satisfy $\boldsymbol{X}^{(i)}_{\boldsymbol{n+1}} = \phi(\boldsymbol{X}^{(i)}_{\boldsymbol{n}})$. □

4.3 Summary

This chapter has studied, in detail, the static equilibrium states of the discrete mechanical system shown in Figure 3.1 (p33), and also the static equilibrium states of this system's continuous limit. Physically, this continuum limit leads to a strut with no bending stiffness on a linear Winkler foundation. The analysis of this strut lead to a differential equation that has an explicit solution in terms of elliptic integrals, and this solution was used to plot the relatively simple bifurcation diagram for the equilibrium states of this strut (Figure 4.3 p47). We also saw that the lowest load bifurcation from the flat equilibrium state occurred into a solution that was composed of an infinite number of infinitely small wrinkles (see Figure 4.5 p49).

This chapter then went on to analyse the static equilibrium states of the discrete mechanical system by using the discrete boundary value problem derived in Section 3.2.3 of Chapter 3. Some examples of the bifurcation diagrams for these static equilibrium states were presented for different lattice sizes: $N = 6$ and $N = 16$ in Figures 4.8 and 4.9, p57. We saw that as the bifurcation parameter λ increased, a large number of static equilibrium states is seen in the bifurcation diagram, especially for $\lambda > 4/\delta^2$. The mechanisms for the creation of these solutions in terms of the underlying iterated map were discussed. Finally, the detailed symmetry properties of the solutions to the discrete BVP, summarised in Figure 4.14 p71, were stated and proved.

Chapter 5

Dynamics of a second order mechanical system

The previous chapter studied the global behaviour of the static equilibrium states of the mechanical lattice with vertical springs only shown in Figure 3.1, p33. In this chapter we consider the dynamical behaviour of this mechanical system which is a Hamiltonian dynamical system with Hamiltonian (derived in Section 3.2)

$$H(\boldsymbol{P},\boldsymbol{U}) = \sum_{n=1}^{N-1}\left(\frac{1}{2}(P_n)^2 + \frac{\lambda}{4}(U_n)^2\right) + \sum_{n=1}^{N-1}\sqrt{1-\left(\frac{U_{n+1}-U_n}{\delta}\right)^2} \tag{5.1}$$

where $P_n = \dot{U}_n$ and $U_0 = U_N = 0$. Specifically, we start by analysing the linear behaviour and see how the zero equilibrium loses stability as the applied load exceeds the first buckling load. The spectrum of low amplitude oscillations that exists at prebuckling loads tells us that the linear modes with the lowest spatial wavelength have the highest temporal frequencies. The dynamic stability, under dead loading conditions, of the many static equilibrium states found in the previous chapter is then investigated numerically in Section 5.2 and it is conjectured that all equilibria are dynamically unstable except the prebuckling flat state.

The second part of this chapter considers the existence and stability of breather and phonobreather solutions in this mechanical lattice. Breather solutions are exact time periodic solutions to the equations of motion with, usually exponential, spatial localisation away from the large amplitude breather core. Phonobreather solutions look like breather solutions superimposed on a large amplitude background with sinusoidal spatial oscillations. As described in the introduction (Section 2.4) current existence

proofs for breather solutions in non-linear lattices do not apply to the system with Hamiltonian (5.1). The main reason for this is that the standard anticontinuous limit for this system (sending $\delta \to \infty$ in (5.2) below) leads to decoupled *linear* oscillators, while for proofs such as that of MacKay & Aubry (1994) we require the decoupled oscillators to be nonlinear. This leads us, in Section 5.3, to demonstrate numerically that stable breather solutions can exist in this mechanical lattice and hence could be observed experimentally. Similarly, in Section 5.4 it is shown that the system with Hamiltonian (5.1) can support phonobreather solutions. It is seen that despite the fact that these solutions are linearly unstable, the nonlinear dynamics close to the exact phonobreather solution is regular for a time long enough for this behaviour to be observed experimentally. This new behaviour consists of a growing, disordered phonobreather core which slowly envelops the phonon-like tails. This growth is investigated and it is found that the phonobreather's core width grows at a constant velocity.

The equations of motion studied in this chapter, derived in Section 3.2, for the system with Hamiltonian (5.1) are given in terms of the coordinates $\boldsymbol{U}$ by $\ddot{\boldsymbol{U}} = \boldsymbol{f}(\boldsymbol{U})$ where

$$\boldsymbol{f}(\boldsymbol{U}) = \begin{pmatrix} -\lambda U_1 - \frac{1}{\delta}\bar{g}\left(\frac{U_2 - U_1}{\delta}\right) + \frac{1}{\delta}\bar{g}\left(\frac{U_1}{\delta}\right) \\ \vdots \\ -\lambda U_i - \frac{1}{\delta}\bar{g}\left(\frac{U_{i+1} - U_i}{\delta}\right) + \frac{1}{\delta}\bar{g}\left(\frac{U_i - U_{i-1}}{\delta}\right) \\ \vdots \\ -\lambda U_{N-1} - \frac{1}{\delta}\bar{g}\left(\frac{-U_{N-1}}{\delta}\right) + \frac{1}{\delta}\bar{g}\left(\frac{U_{N-1} - U_{N-2}}{\delta}\right) \end{pmatrix} \tag{5.2}$$

for $i = 2, \ldots, N-2$ and $\bar{g}(x) = x/\sqrt{1-x^2}$. Strictly, we saw in sections 3.2 and 3.2.1 where the above equations of motion were derived from a mechanical system that, the parameter δ is not a free parameter and is given by $\delta = 1/N$. However, if we remove this restriction we notice that there is a scaling symmetry of (5.2) related to the variable δ that is presented in the following lemma.

Lemma 5.1. *Given a solution $\boldsymbol{U}(t)$ to the equations of motion $\ddot{\boldsymbol{U}} = \boldsymbol{f}(\boldsymbol{U})$ at the parameter values λ and δ, the function $\bar{\boldsymbol{U}} = a\boldsymbol{U}$ is also a solution at the parameter values $\bar{\delta} = a\delta$, $\bar{\lambda} = \lambda/a^2$ $\bar{t} = at$, for any $a \in \mathbb{R}$.*

Proof. The inverse of the given transformation is

$$\boldsymbol{U} = \frac{\bar{\boldsymbol{U}}}{a}, \quad \delta = \frac{\bar{\delta}}{a}, \quad \lambda = a^2\bar{\lambda}, \quad t = \frac{\bar{t}}{a}.$$

Substituting this into the general term of function $\boldsymbol{f}$ (5.2) gives

$$\begin{aligned} \frac{a^2}{a}\frac{\mathrm{d}^2\bar{U}_i}{\mathrm{d}\bar{t}^2} &= -\frac{a^2}{a}\bar{\lambda}\bar{U}_i - \frac{a}{\bar{\delta}}\bar{g}\left(\frac{\bar{U}_{i+1}-\bar{U}_i}{\bar{\delta}}\right) + \frac{a}{\bar{\delta}}\bar{g}\left(\frac{\bar{U}_i-\bar{U}_{i-1}}{\bar{\delta}}\right) \\ \Rightarrow \frac{\mathrm{d}^2\bar{U}_i}{\mathrm{d}\bar{t}^2} &= -\bar{\lambda}\bar{U}_i - \frac{1}{\bar{\delta}}\bar{g}\left(\frac{\bar{U}_{i+1}-\bar{U}_i}{\bar{\delta}}\right) + \frac{1}{\bar{\delta}}\bar{g}\left(\frac{\bar{U}_i-\bar{U}_{i-1}}{\bar{\delta}}\right) \end{aligned}$$

for $i = 2, \ldots, N-2$. Considering this expression for $i = 1$ with $U_0 = 0$ and $i = N-1$ with $U_N = 0$ demonstrates that this scaling also holds for the first and last components of (5.2). Thus, the new function $\bar{\boldsymbol{U}}(\bar{t})$ at the parameter values $\bar{\delta}$ and $\bar{\lambda}$ is also a solution to the differential equation $\ddot{\boldsymbol{U}} = \boldsymbol{f}(\boldsymbol{U})$. □

Using this this scaling symmetry we can investigate the equations $\ddot{\boldsymbol{U}} = \boldsymbol{f}(\boldsymbol{U})$ for any convenient value of δ and then transform the solution to the 'correct' value of δ, $\delta = 1/N$, later if necessary. This is used in Section 5.3 and 5.4 in this chapter to choose a value of δ ($\delta = 0.1$) for which the numerical calculations are better scaled for the lattice with $N = 29$.

5.1 Primary bifurcations

In Chapter 4 the static equilibrium states of the mechanical system of Figure 3.1 with vertical springs only were studied in detail. In the notation of this chapter these solutions correspond to solutions of the equation $\boldsymbol{f}(\boldsymbol{U}) = 0$ where $\boldsymbol{f}$ is given by (5.2) above. As a reminder, in the previous chapter it was found that there are $N-1$ primary, buckling bifurcations from the flat equilibrium state as λ is increased from 0 to $4/\delta^2$, also for $\lambda > 4/\delta^2$ a large number of secondary solutions appear through various mechanisms (see Section 4.2.2). This static behaviour cannot exist independently of the dynamic behaviour and so in this section we see how the $N-1$ primary, static bifurcations lead to the increasing dynamic stability of the zero equilibrium state as each normal (or linear) mode becomes oscillatory as λ passes through the critical values $\lambda^*_{n,N} = 2(1-\cos n\pi/N)/\delta^2$. Equivalently, this demonstrates how the mechanical system's flat state becomes more and more unstable as the load p is increased through the first and then subsequent buckling loads (from the nondimensionalisations presented in Section 3.2.1 we have $p \propto 1/\lambda$).

To begin this analysis we shall look at the linear behaviour of the second order differential equations given by $\ddot{\boldsymbol{U}} = \boldsymbol{f}(\boldsymbol{U})$ where $\boldsymbol{f}$ is given by (5.2) above. The linear

behaviour is determined by the properties of the Jacobian matrix $\boldsymbol{f}'(\boldsymbol{U})$ where

$$[\boldsymbol{f}'(\boldsymbol{U})]_{ij} = \frac{\partial f_i}{\partial U_j} \quad \text{for} \quad i,j = 1,\ldots,N-1$$

and

$$\boldsymbol{f}'(\boldsymbol{U}) = \begin{pmatrix} -\lambda + \frac{1}{\delta^2}\bar{g}'\left(\frac{U_2-U_1}{\delta}\right) + \frac{1}{\delta^2}\bar{g}'\left(\frac{U_1}{\delta}\right), & -\frac{1}{\delta^2}\bar{g}'\left(\frac{U_2-U_1}{\delta}\right), & \ldots, & 0 \\ & \ddots & & \ddots \\ \ldots, & -\frac{1}{\delta^2}\bar{g}'\left(\frac{U_i-U_{i-1}}{\delta}\right), & -\lambda + \frac{1}{\delta^2}\bar{g}'\left(\frac{U_{i+1}-U_i}{\delta}\right) + \frac{1}{\delta^2}\bar{g}'\left(\frac{U_i-U_{i-1}}{\delta}\right), & -\frac{1}{\delta^2}\bar{g}'\left(\frac{U_{i+1}-U_i}{\delta}\right) \\ & \ddots & \ddots & \ddots \\ 0, & \ldots, & -\frac{1}{\delta^2}\bar{g}'\left(\frac{U_{N-1}-U_{N-2}}{\delta}\right), & -\lambda + \frac{1}{\delta^2}\bar{g}'\left(\frac{U_{N-1}}{\delta}\right) + \frac{1}{\delta^2}\bar{g}'\left(\frac{U_{N-1}-U_{N-2}}{\delta}\right) \end{pmatrix} \tag{5.3}$$

with $\bar{g}'(x) = (1-x^2)^{\frac{-3}{2}}$. The analysis below begins by looking at the linear behaviour about the zero equilibrium $\boldsymbol{U} = \boldsymbol{0}$ and so we require $\boldsymbol{f}'(\boldsymbol{0})$:

$$\boldsymbol{f}'(\boldsymbol{0}) = \frac{1}{\delta^2}\begin{pmatrix} -\lambda\delta^2+2 & -1 & & & \\ & \ddots & \ddots & & \\ & -1 & -\lambda\delta^2+2 & -1 & \\ & & \ddots & \ddots & \\ & & -1 & -\lambda\delta^2+2 \end{pmatrix}. \tag{5.4}$$

The eigenvalues γ_k and eigenvectors $\boldsymbol{U^{(k)}}$ of this matrix are easily found (see, for example, Saad (2003)) to be

$$\gamma_k = \lambda^*_{k,N} - \lambda \tag{5.5}$$

$$U^{(k)}_n = \sin\frac{kn\pi}{N} \quad \text{for} \quad n = 1,\ldots,N-1. \tag{5.6}$$

with $\lambda^*_{k,N} = 2\left(1-\cos\frac{k\pi}{N}\right)/\delta^2$. The dynamic behaviour about the $\boldsymbol{U} = \boldsymbol{0}$ equilibrium now becomes clear if for $\lambda \neq \lambda^*_{n,N}$, $(n = 1,\ldots,N-1)$ we choose coordinates $\boldsymbol{Q}$ that diagonalise the matrix $\boldsymbol{f}'(\boldsymbol{0})$ (i.e. we move into normal mode coordinates). This transformation is given by

$$\boldsymbol{U} = V\boldsymbol{Q} \quad \text{where} \quad [V]_{ij} = \sin\frac{ij\pi}{N}$$

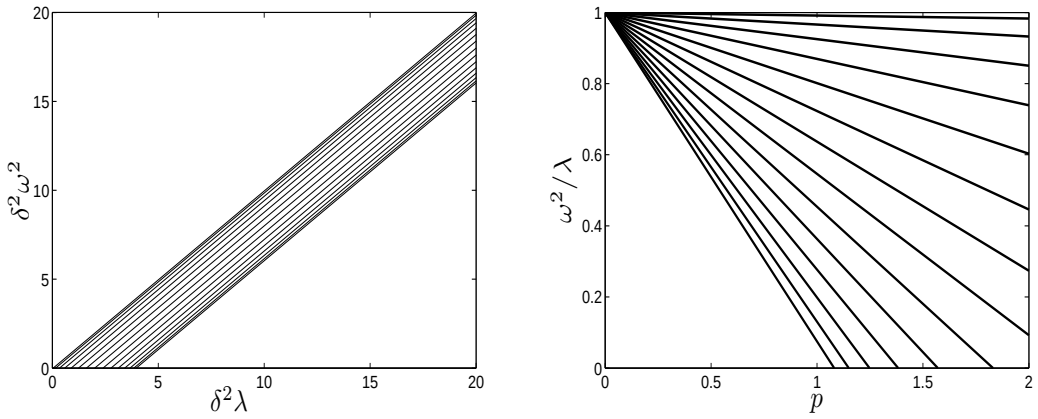

Figure 5.1: *Left: The λ dependence of the linear mode frequencies for $N = 16$. Right: The nondimensional load, p, dependence of the normal mode frequencies for $N = 16$.*

so that $\ddot{\boldsymbol{Q}} = D\boldsymbol{Q}$ with the diagonal matrix D given by $D = \mathrm{Diag}(\gamma_1, \ldots, \gamma_{N-1})$. Using this transformation we immediately see that the resulting linear system $\ddot{\boldsymbol{Q}} = D\boldsymbol{Q}$ comprises $N-1$ harmonic oscillators with frequencies ω_k given by $\omega_k = \sqrt{-\gamma_k} = \sqrt{\lambda - \lambda^*_{k,N}}$. The $N-1$ linearly independent solutions being given by

$$Q_k(t) = Q_k(0)\sin(\omega_k t + \phi) \quad \text{equivalently} \quad U_n^{(k)}(t) = Q_k(0)\sin(\omega_k t + \phi)\sin\frac{kn\pi}{N} \tag{5.7}$$

for some initial amplitudes $Q_k(0)$ and phase ϕ. Thus for $\lambda < \lambda^*_{1,N}$ all of the normal modes have imaginary frequencies and so do not oscillate but diverge exponentially, and the zero equilibrium state is maximally unstable. As λ then increases through the values $\lambda^*_{k,N}$ for $k = 1, \ldots, N-1$ each normal mode becomes oscillatory until for $\lambda > \lambda_{N-1,N}$ all the normal modes are oscillatory and the zero equilibrium is stable. This dependence of the frequencies ω_k on λ is shown in the left panel of Figure 5.1 for $N = 16$. In the right panel of Figure 5.1 it is shown how the frequencies depend on the load applied to the mechanical system (recall $p \propto 1/\lambda$). Here we see that with no load, $p = 0$, all the oscillators are uncoupled and oscillate with the same angular frequency. As the load is increased the spread of frequencies then increases until the first buckling load $p = 4N^2/\lambda^*_{N-1,N}$ is reached. The zero equilibrium then becomes unstable as a normal mode becomes hyperbolic. It is interesting to note here that the fixed boundary conditions we are studying have prevented the very first bifurcation at $p = 1$ into the mode where all the pivots of the system oscillate in phase; similarly, the very last bifurcation where $U_n \propto (-1)^n$ is also prevented. These two modes would appear in a system with periodic or free boundary conditions.

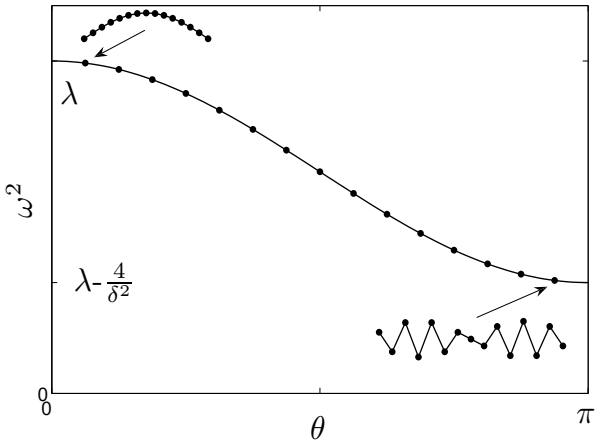

Figure 5.2: *A graph of the dispersion relation (5.8). The dots correspond to the modes present in the lattice with $N = 16$. The inset plots show the spatial profiles of the first and last modes in the $N = 16$ lattice.*

It is also interesting to note the relation between the temporal period of these lattice oscillations and the spatial wavelength. This dispersion relation, found by expanding (5.5) to give

$$\omega(\theta)^2 = \lambda - 2(1-\cos\theta)/\delta^2 \quad \Rightarrow \quad \left(\frac{\omega}{\sqrt{\lambda}}\right)^2 = 1 + p\frac{1}{2}(\cos(\theta)-1) \tag{5.8}$$

where θ is the spatial wave number given by $\theta = k\pi/N$ for the kth mode of the N link lattice, is plotted in Figure 5.2. The dots in Figure 5.2 show the frequencies present in the lattice for $N = 16$ whilst the line shows the curve that results from the dense set of frequencies that occur for the infinite lattice. We can clearly see that the highest frequency modes have the lowest wavenumber θ and hence the longest spatial wavelength.

The next section investigates the number of stable eigenvalues on the multitude of non-zero static equilibrium states found in the previous chapter, but before this is done it is useful for this and later sections to write the second order differential equations $\ddot{\boldsymbol{U}} = \boldsymbol{f}(\boldsymbol{U})$ in the canonical first order form $\dot{\boldsymbol{X}} = \boldsymbol{F}(\boldsymbol{X})$ where $\boldsymbol{X} = (U_1, U_2, \ldots, U_{N-1}, \dot{U}_1, \ldots, \dot{U}_{N-1})^{\mathrm{T}}$ and

$$\dot{\boldsymbol{X}} = \boldsymbol{F}(\boldsymbol{X}) \equiv \begin{pmatrix} \dot{\boldsymbol{U}} \\ \boldsymbol{f}(\boldsymbol{U}) \end{pmatrix}. \tag{5.9}$$

The Jacobian of $\boldsymbol{F}$ is given in block form by

$$\boldsymbol{F}'(\boldsymbol{X}) = \begin{pmatrix} 0 & \mathrm{I}_{N-1} \\ \boldsymbol{f}'(\boldsymbol{U}) & 0 \end{pmatrix} \tag{5.10}$$

and the linearisation of this system about the zero, flat static equilibrium state $\boldsymbol{X} = \boldsymbol{0} \in \mathbb{R}^{2N-2}$ is given, in block form, by

$$\boldsymbol{F}'(\boldsymbol{0}) = \begin{pmatrix} 0 & \mathrm{I}_{N-1} \\ \boldsymbol{f}'(\boldsymbol{0}) & 0 \end{pmatrix}. \tag{5.11}$$

The next lemma finds the eigenvalues and eigenvectors of the matrix $\boldsymbol{F}'(\boldsymbol{0})$ in terms of the eigenvalues and eigenvectors of $\boldsymbol{f}'(\boldsymbol{0})$.

Lemma 5.2. *The $2N-2$ eigenvalues γ and eigenvectors ν of $\boldsymbol{F}'(\boldsymbol{0})$ come in pairs μ_k^+, μ_k^-, ν_k^+ and ν_k^- for $k = 1, \ldots, N-1$ and are given by*

$$\begin{array}{ll} \textit{Eigenvalue} & \textit{Corresponding Eigenvector} \\ \mu_k^+ = +\sqrt{\gamma_k} & \nu_k^+ = \begin{pmatrix} \boldsymbol{U^{(k)}} \\ +\sqrt{\gamma_k}\,\boldsymbol{U^{(k)}} \end{pmatrix} \\ \mu_k^- = -\sqrt{\gamma_k} & \nu_k^- = \begin{pmatrix} \boldsymbol{U^{(k)}} \\ -\sqrt{\gamma_k}\,\boldsymbol{U^{(k)}} \end{pmatrix} \end{array}$$

where γ_k and $\boldsymbol{U^{(k)}}$ are the eigenvalues and eigenvectors of $\boldsymbol{f}'(\boldsymbol{0})$ respectively given by (5.5) and (5.6).

Proof. We can write the eigenvector equation for $\boldsymbol{F}'(\boldsymbol{0})$ in block form using (5.11) to give

$$\begin{gathered} \boldsymbol{F}'(\boldsymbol{0}) \begin{pmatrix} \boldsymbol{\nu_1} \\ \boldsymbol{\nu_2} \end{pmatrix} = \begin{pmatrix} 0 & \mathrm{I}_{N-1} \\ \boldsymbol{f}'(\boldsymbol{0}) & 0 \end{pmatrix} \begin{pmatrix} \boldsymbol{\nu_1} \\ \boldsymbol{\nu_2} \end{pmatrix} = \mu \begin{pmatrix} \boldsymbol{\nu_1} \\ \boldsymbol{\nu_2} \end{pmatrix} \\ \Rightarrow \boldsymbol{\nu_2} = \mu \boldsymbol{\nu_1} \quad \text{and} \quad \boldsymbol{f}'(0)\boldsymbol{\nu_1} = \mu \boldsymbol{\nu_2} \\ \Rightarrow \boldsymbol{f}'(\boldsymbol{0})\boldsymbol{\nu_1} = \mu^2 \boldsymbol{\nu_1}. \end{gathered}$$

From this we can see that the square of the eigenvalues of $\boldsymbol{F}'(\boldsymbol{0})$ are the eigenvalues of $\boldsymbol{f}'(\boldsymbol{0})$ and that the corresponding eigenvectors of $\boldsymbol{F}'(\boldsymbol{0})$ are given by the expressions above in the table. □

The previous discussion on the stability of the zero equilibrium can now be rephrased in terms of the eigenvalues of $\boldsymbol{F}'(\boldsymbol{0})$. For $\lambda < 2\left(1 - \cos\frac{\pi}{N}\right)/\delta^2$ all the eigenvalues of $\boldsymbol{F}'(\boldsymbol{0})$ are real and come in pairs of opposite sign, making the zero equilibrium state unstable. As λ in increased through each singular point, $\lambda = \lambda_{k,N}^* = 2\left(1 - \cos\frac{k\pi}{N}\right)/\delta^2$ for $k = 1, \ldots, N-1$, in turn, a pair of real eigenvalues passes through zero and moves onto the imaginary axis.

5.2 Stability of static equilibrium states

Chapter 4 studied the existence, symmetry properties and parameter dependence of the static equilibrium states for the mechanical system with vertical springs only of Figure 3.1. These static equilibrium states, in the notation of the previous section, satisfy $\boldsymbol{F}(\boldsymbol{X}) = \boldsymbol{0}$, and in this section we move on to study the linear dynamic stability of these equilibrium states by computing the eigenvalues of $\boldsymbol{F}'(\boldsymbol{X})$ on the solution branches. These eigenvalue calculations can be performed automatically using the continuation software Auto and this is the method used here. We define N_s to be equal to the number of eigenvalues, μ, of $\boldsymbol{F}'(\boldsymbol{X})$ that satisfy $\mathrm{Re}(\mu) \leq 0$. Then, since the dimension of $\boldsymbol{F}'(\boldsymbol{X})$ is $2N-1$, if $N_s < 2N-1$ there is an eigenvalue with $\mathrm{Re}(\mu) > 0$ and the equilibrium is unstable.

Figure 5.3 shows the value of N_s on the branches connected to the zero equilibrium of the lattice with $N = 8$. With $N = 8$ for an equilibrium state to be linearly stable we require $N_s = 2(N-1) = 14$. In Figure 5.3 we can see that at each of the primary bifurcations from the zero solution the zero equilibrium becomes more stable, as a pair of eigenvalues with opposite sign move off the real axis and onto the imaginary axis as found in the previous section. The zero equilibrium is thus linearly stable for $\lambda > \lambda^*_{N-1,N}$.

Now considering the non-zero branches, we see in Figure 5.3 that all the primary branches are unstable to varying degrees and lose stability at the secondary bifurcations, the secondary branches inheriting the stability of the main branch. Along the secondary branches we have the opposite behaviour at the tertiary bifurcations: the secondary branch gains stability and the bifurcating solutions are less stable than the secondary branch. If this alternating behaviour of the bifurcation character continues for all branch sub-bifurcations it tells us that none of the branches connected to a primary branch can have a stability greater than that of the primary branch. This leads us to predict that all of the branches connected to the zero equilibrium are linearly unstable. Physically, this is what one would expect. Since all the bifurcations from the zero solution are subcritical once the system has buckled from its zero state, at constant load the structure will simply fold up and end up in a state where the first and last pivots are touching.

Figure 5.4 shows the stability of some of the disconnected static equilibrium states for $N = 6$. The circles are solutions computed by the bisection algorithm of Domokos & Holmes (1993) used in Chapter 4 while the solid lines are the branches computed using the continuation software Auto on which the stability values have been calculated.

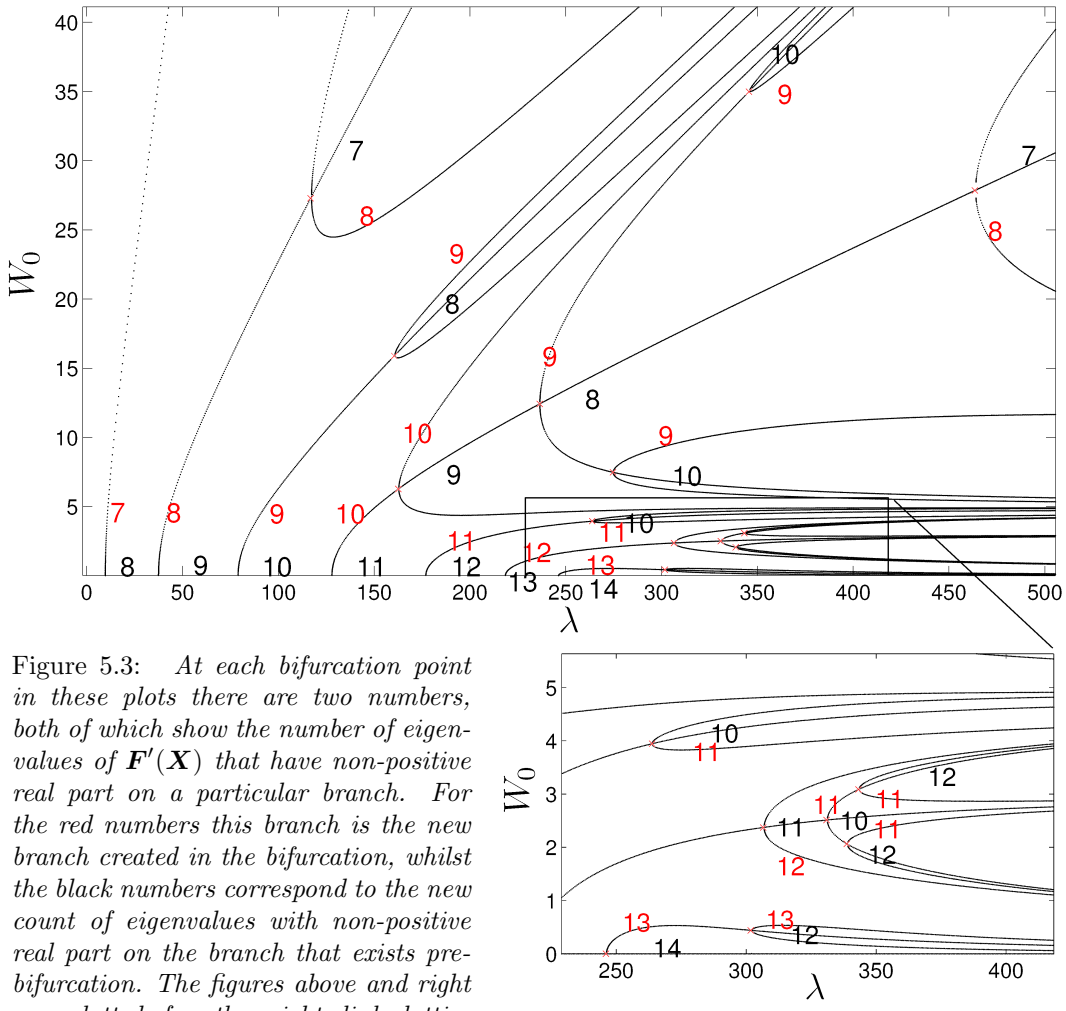

Figure 5.3: *At each bifurcation point in these plots there are two numbers, both of which show the number of eigenvalues of $\boldsymbol{F}'(\boldsymbol{X})$ that have non-positive real part on a particular branch. For the red numbers this branch is the new branch created in the bifurcation, whilst the black numbers correspond to the new count of eigenvalues with non-positive real part on the branch that exists pre-bifurcation. The figures above and right are plotted for the eight link lattice ($N = 8$).*

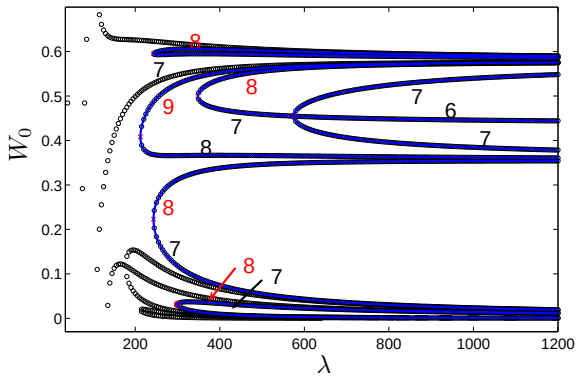

Figure 5.4: *This shows the number of eigenvalues of $\boldsymbol{F}'(\boldsymbol{X}(\lambda))$ that have non-positive real part on some of the disconnected static equilibrium solution branches for $N = 6$.*

The lower half of the disconnected branches have lower N_s than the upper branches. With $N = 6$ we require $N_s = 10$ to have a linearly stable equilibrium and so there are no linearly stable equilibria in this bifurcation diagram. This circumstantial evidence leads us to conjecture that the zero equilibrium for $\lambda > \lambda^*_{N-1,N}$ is the only linearly stable equilibrium state for this mechanical system.

5.3 Breathers

In this section we find, numerically, time periodic, spatially localised solutions of the nonlinear lattice equations $\ddot{\boldsymbol{U}} = \boldsymbol{f}(\boldsymbol{U})$ with $\boldsymbol{f}$ given by (5.2). This type of solution, called a discrete breather, has seen a great deal of attention in the literature (see the reviews of Flach & Willis (1998), Flach & Gorbach (2008)) but little of this attention has been in macroscopic structural engineering systems (see Section 2.4 of the introduction for further discussion). Thus these computations are some of the first to show the existence of breathers in a structural system.

5.3.1 Breather search: method

There are several methods for computing breather solutions numerically (Flach & Willis (1998)) which fall into two categories: phase space methods and Fourier space methods. Here we use the phase space method of Marin & Aubry (1996). Fourier space methods work by writing the time dependence of the solution with frequency ω_b in the form

$$u_n(t) = \sum_{k=-\infty}^{\infty} x_n^{(k)} \exp(\mathrm{i}k\omega_b t)$$

and then, since the Fourier coefficients $x_n^{(k)}$ decay fairly quickly with k, the infinite series can be truncated early to obtain the approximation as a system of algebraic equations for the $x_n^{(k)}$. One drawback of this method is that it only works efficiently for systems with low order polynomial Hamiltonians (see (Marin & Aubry 1996, §A.2) for further discussion). Since the Hamiltonian (5.1) has a square root nonlinearity we use the more general phase space method which is now described.

We restrict ourselves to searching for time reversible periodic solutions and do this using a Newton based method. These solutions $\boldsymbol{Y}(t) = (\boldsymbol{q}(t), \boldsymbol{p}(t))^{\mathrm{T}}$ satisfy $\boldsymbol{Y}(0) \in \mathrm{Fix}(R)$ where R is the involution $(\boldsymbol{q}, \boldsymbol{p}) \to (\boldsymbol{q}, -\boldsymbol{p})$. It is also true that if, for any solution to any set of reversible, Hamiltonian equations of motion $\boldsymbol{Y}(0) \in \mathrm{Fix}(R)$ then $\boldsymbol{Y}(t)$ is a time

periodic solution (see Marin & Aubry (1996) for further details). The Newton method thus searches for zeros of the map $\mathcal{F} : \mathbb{R}^m \to \mathbb{R}^m$ $\boldsymbol{q}(0) \to \boldsymbol{p}(T)$, where $T = 2\pi/\omega$ is the period of the periodic orbit sought and $\boldsymbol{q}, \boldsymbol{p} \in \mathbb{R}^m$. The numerical accuracy of this method depends on the Newton's method convergence criterion and the accuracy of the numerical integrator used to find $\boldsymbol{Y}(T)$. In this work Matlab, with its IVP solver ode45 is used to compute individual time periodic solutions whilst Auto, which uses an adaptive collocation method to solve the relevant ODEs is used to perform continuation of these periodic solutions.

Newton's method does not work unless we have a good approximation to the solution to start with and so we now explain how this is found. The equations of motion we are studying ($\ddot{\boldsymbol{U}} = \boldsymbol{f}(\boldsymbol{U})$ with $\boldsymbol{f}$ given by (5.2)) are re-written here for convenience:

$$\begin{aligned}
\ddot{U}_1 &= -\lambda U_1 - \frac{1}{\delta}\bar{g}\left(\frac{U_2 - U_1}{\delta}\right) + \frac{1}{\delta}\bar{g}\left(\frac{U_1}{\delta}\right) \\
\ddot{U}_i &= -\lambda U_i - \frac{1}{\delta}\bar{g}\left(\frac{U_{i+1} - U_i}{\delta}\right) + \frac{1}{\delta}\bar{g}\left(\frac{U_i - U_{i-1}}{\delta}\right) \\
\ddot{U}_{N-1} &= -\lambda U_{N-1} - \frac{1}{\delta}\bar{g}\left(\frac{-U_{N-1}}{\delta}\right) + \frac{1}{\delta}\bar{g}\left(\frac{U_{N-1} - U_{N-2}}{\delta}\right)
\end{aligned} \tag{5.12}$$

for $i = 2, \ldots, N-2$. The method of Marin & Aubry (1996) relies on the existence of a nonlinear anti-continuous limit of the lattice equation in question. This is a limit of one of the parameters of the system such that in this limit the equation becomes a set of decoupled *nonlinear* oscillators. A trivial breather at frequency ω_b can be created in this limit: one oscillator oscillating while the others are stationary. This trivial breather is represented by a phase sequence which is a string of $N-1$ phases taken from the set $\{-1, 0, 1\}$ giving the relative phase of the corresponding oscillator displacements in the anticontinuous limit[1]. For example 000000010000000 is the sequence for the simplest breather with $N = 16$. As long as this breather is at a frequency that does not resonate with the linear modes of the system, it can then be numerically continued from this anti-continuous limit to the finite coupling regime to give the required breather. In (5.12) we see that there is no such limit (the limit $\delta \to \infty$ leads to decoupled *linear* oscillators) and so a change of variables is required (Marin & Aubry (1996)) to create a system that will give us breathers via the above method. This change of variables is

$$Y_1 = U_1, \quad Y_i = U_i - U_{i-1} \quad \text{for} \quad i = 1, \ldots, N, \quad Y_N = -U_{N-1}. \tag{5.13}$$

Using this and subtracting (5.12) for $i = j+1$ from (5.12) for $i = j$ we get the following

[1]The condition that, in the anticontinuous limit, all the oscillators are either at rest or oscillate at the frequency ω_b and the condition that $\boldsymbol{p}(0) = \boldsymbol{0}$ leads to the set of admissible phases $\{-1, 0, 1\}$.

equations of motion for the variables Y_j

$$\begin{aligned}
\ddot{Y}_1 &= -\lambda Y_1 + \frac{1}{\delta}\bar{g}\left(\frac{Y_1}{\delta}\right) - \frac{C}{\delta}\bar{g}\left(\frac{Y_2}{\delta}\right) \\
\ddot{Y}_j &= -\lambda Y_j + \frac{2}{\delta}\bar{g}\left(\frac{Y_j}{\delta}\right) - \frac{C}{\delta}\left(\bar{g}\left(\frac{Y_{j+1}}{\delta}\right) + \bar{g}\left(\frac{Y_{j-1}}{\delta}\right)\right) \\
\ddot{Y}_N &= -\lambda Y_N + \frac{1}{\delta}\bar{g}\left(\frac{Y_N}{\delta}\right) - \frac{C}{\delta}\bar{g}\left(\frac{Y_{N-1}}{\delta}\right).
\end{aligned} \tag{5.14}$$

for $j = 2, \ldots, N-1$. Here the continuation parameter C has been introduced so that when $C = 0$ the system decouples into N nonlinear oscillators. Once we have found a breather solution in this lattice equation at $C = 1$ we can recover the original coordinates U_n by using the expression

$$U_n = \sum_{i=1}^{n} Y_i \quad \text{for} \quad n = 1, \ldots, N-1. \tag{5.15}$$

We notice here that the transformation (5.13) introduces an extra degree of freedom to the dynamical system making a total of N, but the underlying dynamics is that of the $N-1$ dimensional system (5.12). We can understand this by considering the following: (5.13) implies that $U_{N-1} = -Y_N$ whilst (5.15) implies $U_{N-1} = \sum_{i=1}^{N-1} Y_i$. This implies that for the dynamical system (5.14)

$$\sum_{i=1}^{N-1} Y_i = -Y_N \quad \text{equivalently} \quad \sum_{i=1}^{N} Y_i = 0. \tag{5.16}$$

Thus the dynamics of (5.14) is restricted to the $N-1$ dimensional manifold given by (5.16).

The final step in this method is to choose the breather frequency ω_b at the anticontinuous limit, $C = 0$, by making use of the nontrivial frequency amplitude dependence of the decoupled nonlinear oscillators. We choose ω_b such that when the trivial breather is continued in the continuation parameter C from $C = 0$ to $C = 1$ its frequency does not collide with the frequency of the linear modes of the system or their sub-multiples; i.e $n\omega_b \neq \omega_i$ for all $n \in \mathbb{N}$ and ω_i in the spectrum of the lattice. The linear spectrum for the differential equations (5.12) was seen in the previous section and the equivalent spectrum for the equations (5.14) is

$$\omega_k^2 = \lambda - \frac{2}{\delta^2} + \frac{2C}{\delta^2}\cos(\theta_k) \quad \Rightarrow \quad \left(\frac{\omega_k}{\sqrt{\lambda}}\right)^2 = 1 + p\frac{1}{2}(C\cos(\theta_k) - 1) \tag{5.17}$$

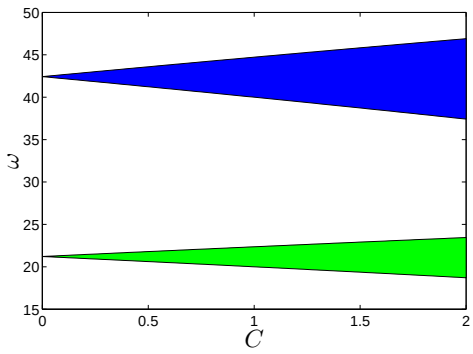

Figure 5.5: *The plot shows how the width of the linear spectrum (upper filled area) changes with the continuation parameter C (equation 5.17) for the parameter values $\lambda = 2000$ and $\delta = 0.1$. The lower filled area shows the area where $\omega = \omega_p/2$ for all ω_p in the main band above.*

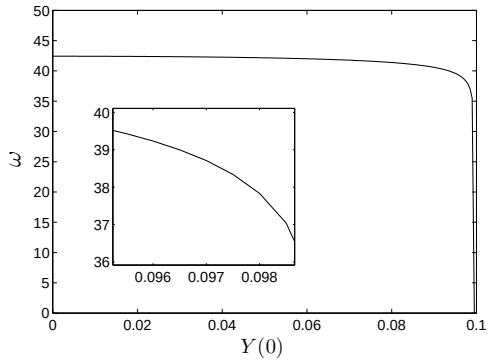

Figure 5.6: *The decoupled nonlinear oscillators found by setting $C = 0$ in (5.14) have the displayed frequency-amplitude dependence. This was calculated via the method described in §5.6.*

with $\theta_k = k\pi/N$ for $k = 1, \ldots, N-1$. The corresponding linear modes, found by transforming the linear solutions in coordinates U_i (5.7) using (5.13) are given by

$$Y_j^{(k)}(t) = 2\cos\left(\frac{n\pi}{N}(j - \tfrac{1}{2})\right)\cos\omega t \tag{5.18}$$

for $j = 1, \ldots, N-1$, $k = 1, \ldots, N-1$. As N becomes large the frequencies ω_k form a dense band and Figure 5.5 shows how the width of this band changes as C is varied. To help illustrate the choice of amplitude in the anticontinuous limit, Figures 5.5 and 5.6 are plotted for the parameter values $\lambda = 2000$ and $\delta = 0.1$ used in the next section (solutions (d) and (g) of Figure 5.7). From these figures we can see that if, for instance, we choose $\omega_b = 38$ we will not enter the bands shown in Figure 5.5 when we continue up to $C = 1$. Figure 5.6 shows the amplitude-frequency relation for the uncoupled nonlinear oscillators (5.14) computed using the method described in Section 5.6, and from this we can see that choosing $Y_k(0) \approx 0.0976$ will lead to an oscillation frequency of 38.

Finally, the work of the previous discussion leads to an approximate breather solution in the anticontinuous limit of equations (5.14) which can be used as a starting solution for Newton's method which will then find a breather solution to a good numerical accuracy. The following approximate breather solution finishes the example started in

	Phase sequence at $C = 0$	λ	δ	N	ω_b
(a)	0000000100000000	4000	1/16	16	52
(d)	00000000000000100000000000000	2000	0.1	29	38
(g)	000000010000000000000(−1)0000000	2000	0.1	29	38

Table 5.1: *Parameter values for the breather solutions shown in Figure 5.7.*

the previous paragraph.

$$\omega_b = 38, \quad \lambda = 2000, \quad \delta = 0.1, \quad N = 29, \quad C = 0.01$$

$$\boldsymbol{p}(0) = \mathbf{0} \in \mathbb{R}^{N-1}$$

$$\boldsymbol{q}(0) = 0.0976(0,0,0,0,0,0,0,0,0,0,0,0,0,0,1,0,0,0,0,0,0,0,0,0,0,0,0,0,0)^{\mathrm{T}}.$$

The result of finding this particular breather solution accurately and continuing it up to $C = 1$ is shown in (d) of Figure 5.7 of the next section.

5.3.2 Breather search: results

To demonstrate that the method described in the previous section is indeed applicable this lattice equation, three breather solutions have been calculated and are shown in Figure 5.7. For each breather solution found, this figure shows the spatial profile at maximum amplitude for the solution at $C = 1$ in the $\boldsymbol{Y}$ coordinates (left) and this solution transformed back into the original coordinates $\boldsymbol{U}$ (centre). The right column shows the time dependence of each of the pivots in the lattice $U_n(t)$ for eight breather periods. The three breather solutions calculated have parameter values shown in Table 5.1. The first, (a), links this section with the work of Chapter 4. We see from the bifurcation diagram of the static equilibrium states (Figure 4.9, p57) that $\lambda = 4000$ is well into the parameter region where the static equilibrium states have a complicated and tangled structure. This complicated structure of static equilibrium states will also be reflected in the dynamic behaviour, one aspect of which is this breather solution. The breather solution (d) is the starting point for the phonobreather search in section 5.4 and demonstrates the simplest type of breather solution in a slightly larger lattice with $N = 29$. Solution (g) demonstrates that not only can simple breather solutions be found in this mechanical lattice but multibreather solutions can too. This particular multibreather appears to be two simple breather solutions oscillating separately on different parts of the lattice.

These solutions are mathematically interesting, but in order to observe them experimentally we require them to be at least linearly stable. This is the subject of the next

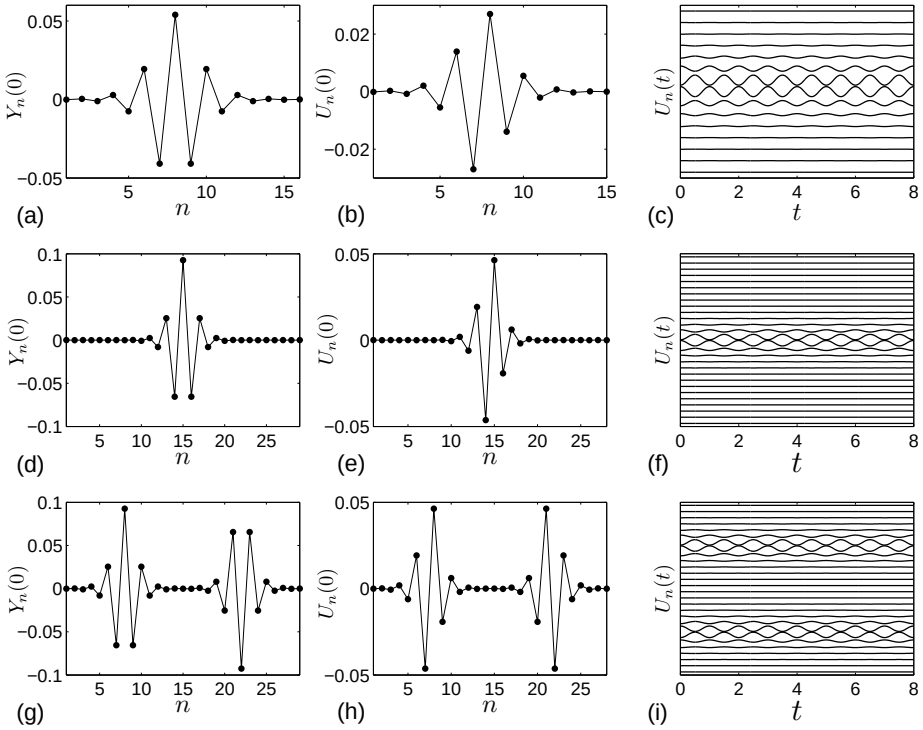

Figure 5.7: *Spatial profile at maximum amplitude for breather solutions the parameter values shown in Table 5.1. The parameter values for the first row correspond to point E in figures 5.10 and 5.11 whilst the second and third rows parameter values are represented by point A in these figures.*

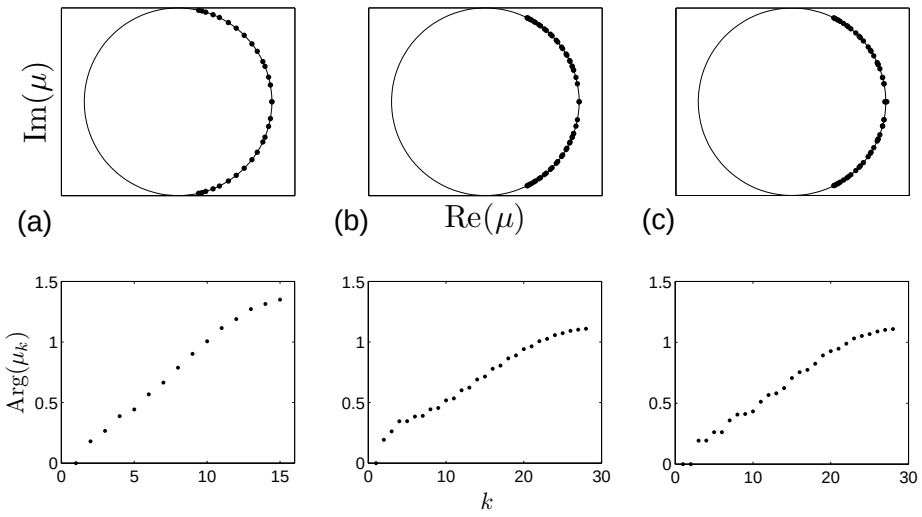

Figure 5.8: *Top: Floquet multipliers for the periodic breather solutions shown in Figure 5.7, shown relative to the unit circle. Bottom: Arguments of the multipliers shown in the corresponding plot above, only the non-negative arguments are shown.*

section.

5.3.3 Breather stability

To determine the linear stability of the periodic breather solutions found in the previous section we compute the Floquet (or characteristic) multipliers for each solution. For a period T periodic solution $\boldsymbol{X}(t)$ to the differential equation $\dot{\boldsymbol{X}} = \boldsymbol{F}(\boldsymbol{X})$ the matrix $M = \partial \boldsymbol{X}(T)/\partial \boldsymbol{X}(0)$ is called the monodromy matrix and its eigenvalues are the Floquet or characteristic multipliers of the periodic solution. Lemma 7 in Section V.E of Meyer & Hall (1992) tells us that for a periodic solution to a set of Hamiltonian equations of motion the characteristic multipliers are given by $1, 1, \mu_3, \ldots, \mu_m$ where in our case $m = 2(N-1)$. Lemma 8 of the same book then gives the eigenvalues of the fixed point of the Poincaré map of the periodic orbit restricted to the relevant level set of the Hamiltonian as $\mu_3, \ldots, \mu_m$. Thus we compute the Floquet multipliers of the periodic orbit and check that there are two unity multipliers and $m-2$ distinct multipliers on the unit circle to verify the solution's linear stability.

The upper plots of Figure 5.8 show the location of the characteristic multipliers relative to the unit circle in the complex plane for the three breather solutions shown in Figure 5.7. These multipliers were computed for the solutions in the original $\boldsymbol{U}$ lattice given by equations (5.12). Columns (a), (b) and (c) of Figure 5.8 correspond to the solutions

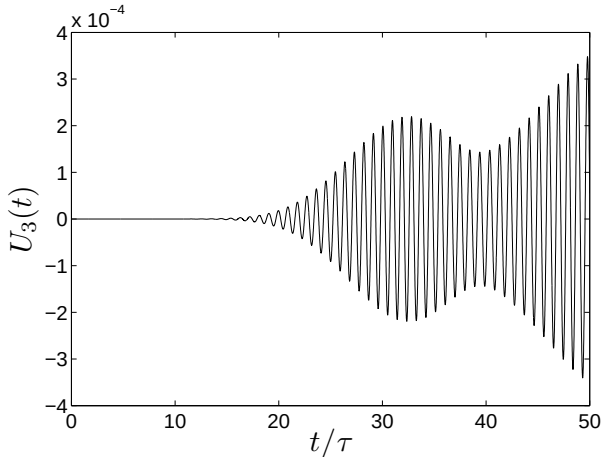

Figure 5.9: *The time evolution $U_3(t)$ for the lattice equations (5.12) for an initial condition close to a breather solution $U(0) = 0.98U_0$ where U_0 is the phase space position of the exact breather solution at maximum amplitude. The breather period is $\tau = 2\pi/\omega_b$.*

in rows (a), (d) and (g) of Figure 5.7. The lower plots of Figure 5.8 show the absolute values of the arguments of the multipliers for the corresponding solution, and since the multipliers come in complex conjugate pairs there are two multipliers for each point in these lower plots. These multipliers were computed using the continuation code Auto. Column (a) shows clearly that there are 14 non-unity distinct multipliers that lie on the unit circle (numerically $\max_k||\mu_k| - 1| \approx 2.3 \times 10^{-6}$) making breather (b) of Figure 5.7 linearly stable. Column (b) again shows that all the multipliers lie on the unit circle (numerically $\max_k||\mu_k| - 1| \approx 1.4 \times 10^{-6}$) but their separation is less clear. To test this numerically the non-unity multipliers with positive argument were ordered so that $\mathrm{Arg}(\lambda_1) \leq \mathrm{Arg}(\lambda_2) \leq \ldots \leq \mathrm{Arg}(\lambda_{(m-2)/2})$. The minimum separation of multipliers can then be calculated $\min_k(\mathrm{Arg}(\lambda_{k+1}) - \mathrm{Arg}(\lambda_k)) \approx 1.4 \times 10^{-3}$. This, although apparently small, is large enough to be classed as separate given the accuracy of these numerical calculations, and so the breather solution of Figure 5.7 row (d) is also linearly stable. The breather solution (g) corresponding to column (c) of Figure 5.8 is, however, unstable. There is a pair of real eigenvalues with $\max_k||\mu_k| - 1| \approx 0.01$ and so this particular multibreather solution is unstable.

This work has demonstrated the existence of linearly stable breather solutions in the mechanical lattice of Figure 3.1. If one was to search for these solutions experimentally it would be useful to have an idea of their lifetime in the fully nonlinear lattice. To investigate this for the breather solution of row (d) of Figure 5.7, the equations of motion (5.12) have been integrated using the Matlab IVP solver ode45 for an initial condition close to the exact breather trajectory: $\boldsymbol{U}(0) = 0.98\boldsymbol{U}_0$ where $\boldsymbol{U}_0$ is the point in phase space where the exact breather solution reaches its maximum amplitude. A result of this integration is shown in Figure 5.9, which shows the time dependence of the third coordinate in the lattice. As time moves forward, nonlinear effects cause a

slow drift away from the exact breather trajectory. Over roughly 20 breather periods energy starts to leak into the tails but this does not immediately destroy the high amplitude breather core and after 50 breather periods the tail amplitude has grown to only 20% of the original breather core amplitude. Thus these solutions have a fairly long life in the fully nonlinear lattice also.

5.4 Phonobreathers

This section first locates phonobreathers in the lattice differential equations (5.12) and then goes on to see that, despite their severe linear instability, there is interesting nonlinear dynamic behaviour close to the exact phonobreather trajectory.

We start by making further use of the continuation software Auto to continue breather solution (e) of Figure 5.7 towards lower values of ω_b, from point A of figures 5.10 and 5.11, down the red, arrowed line to point B. At point B the breather frequency ω_b satisfies $\omega_b = \frac{2}{3}\omega_1$ (numerically this condition was satisfied with a relative error of $1.5 \times 10^{-5}\%$) where w_1 is the frequency of the highest frequency phonon. Also at point B, Auto reports that another branch of solution intersects with this breather branch. This bifurcation scenario is shown in Figure 5.12 where $\|\boldsymbol{U}\|$ denotes the solution norm given by

$$\|\boldsymbol{U}\| = \sqrt{\int_0^1 \sum_{k=1}^{N-1} U_k(t)^2 \, \mathrm{d}t}.$$

If we then switch onto this branch we can see in Figure 5.13 that as we move along the new branch the tails of the breather grow in amplitude in a spatial pattern that is the similar to the highest frequency linear mode. We also find that on this branch the frequency of the new solution is half that of the original breather solution, and so this is a bifurcation in which the period doubles. This type of solution is known as a phonobreather solution (Morgante et al. (2002), Marin & Aubry (1996)). We believe that this is the first observation of a phonobreather solution in a mechanical lattice system.

If the main breather branch is then followed further, towards lower frequencies and point D of Figure 5.12, when ω_b is near $2\omega_2/3$ Auto appears to step onto another branch of phonobreather solutions with twice the period of the original breather solution. As can be seen in Figure 5.12 this appears not to coincide exactly with ω_2; rather, it happens at a slightly lower frequency. These two apparently separate branches are extremely close and are difficult to separate numerically and so the exact bifurcation

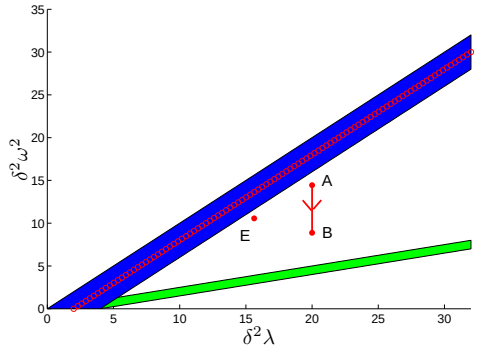

Figure 5.10: *The phonon band width for the equations of motion (5.14) for $C = 1$ (blue) and band half-multiple (green). The red circles show where the spectrum collapses at $C = 0$. The vertical arrow shows the continuation path used in §5.4. Whilst A, B and E mark the parameter space locations of the breathers and phonobreathers found in §5.3 and §5.4.*

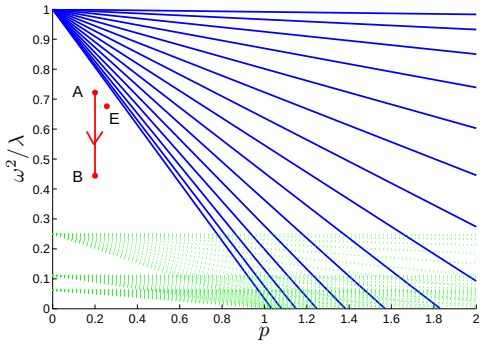

Figure 5.11: *Frequency dependence of each of the linear solutions on the lattice (5.18) in the particular case $N = 16$ (in blue). The lines in red are points in parameter space for which $n\omega_b = \omega_i$ where ω_i is the frequency of the ith linear mode. A, B and E mark the points that correspond to A, B and E in Figure 5.10.*

scenario at D and B is unclear and requires further careful numerical study to see if this behaviour is the same as, or different to, that presented in Morgante et al. (2002).

This raises interesting questions. Although this branch appears to be a resonance between the breather solution and the second highest frequency phonon why does this 'bifurcation' not occur at exactly the resonant frequency value? Also, on this second branch, the frequency-amplitude behaviour is the same as for the first bifurcation, the frequency being essentially independent of the phonobreather tail amplitude. This is surprising as normally when continuing a linear mode in to the nonlinear regime the frequency depends heavily on the amplitude but here the core of the phonobreather appears to reduce or even prevent this change in frequency.

5.4.1 Phonobreather stability

Whilst exact phonobreathers themselves appear to be very unstable (the example at the upper end of the branch starting at B of Figure 5.12 has a pair of real Floquet multipliers off the unit circle one of which $\mu \approx 7.1 \times 10^4$), initial data close to such solutions leads to interesting dynamics which we might expect to observe experimentally. To investigate this we perform a simulation similar to that of the previous section. We start our IVP solver close to the point of peak amplitude for a phonobreather solution and then integrate forward in time. The results for this calculation on the phonobreather

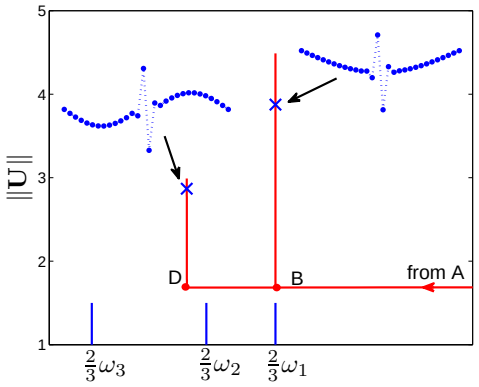

Figure 5.12: *Diagram showing the bifurcation of two phonobreather solutions from the branch of breather solutions given by the vertical arrowed line in Figure 5.10. the lower, vertical, blue lines show $2\omega_i/3$ for $i = 1, 2, 3$.*

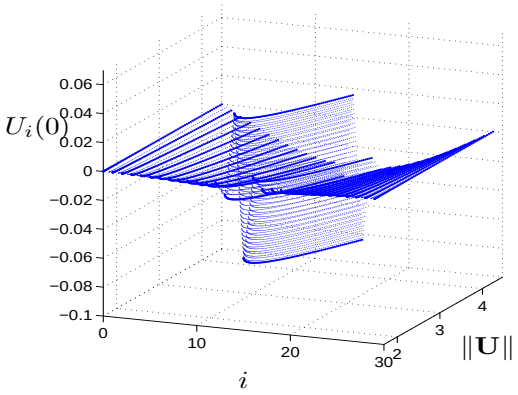

Figure 5.13: *This shows the evolution of the phonobreather solutions up the branch starting at B in Figure 5.12.*

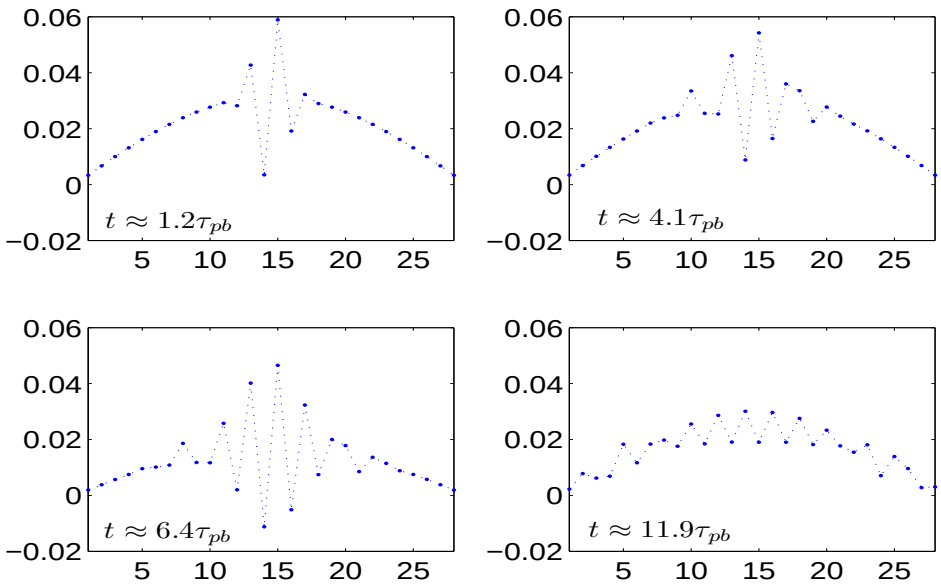

Figure 5.14: *Snapshots of the time evolution of the lattice equation (5.12) with an initial condition close to an exact phonobreather trajectory. The temporal period of the exact phonobreather is τ_{pb}.*

at the upper end of the branch starting at B in Figure 5.12 are summarised in Figure 5.14.

The system stays very close to the exact phonobreather solution for only a short period of time (around one τ_{pb}) but the later dynamics does not head immediately into apparently random oscillation. Qualitatively we can split the spatial profile into the breather core and nonlinear-phonon tails. The simulation shows the breather core losing its neat compact form and the central dynamics becoming less regular. This less regular motion occurs over only a few lattice sites at first and then it slowly expands outwards, encompassing more and more of the stable nonlinear-phonon tails. For the particular case shown in Figure 5.14 where the phonobreather tail has the same spatial wave length as the highest frequency linear mode, it is interesting to note that the less regular motion that causes the breather core to grow appears to be almost entirely composed of a spatial pattern similar to the lowest frequency linear mode. This suggests that the highest and lowest frequency linear modes are more strongly coupled to each other than to the other linear modes.

We estimate the speed of this drift by looking at the time series for each of the lattice nodes in the tail. Before the phonobreather core reaches a particular lattice site labelled by n, $U_n(t)$ oscillates with constant amplitude. We say that the phonobreather core has reached a particular lattice site at time t_c^n when the amplitude of oscillation (i.e. $U_n(t)$ when $\dot{U}_n(t) = 0$) has changed by the relative amount 5×10^{-4}. This motivates the following definition of t_c^n

$$t_c^n = \{\min(t) \text{ such that } \dot{U}_n(t) = 0 \text{ and } \left|\frac{U_n(t) - U_n(0)}{U_n(0)}\right| < 5 \times 10^{-4}\}.$$

Tracking the dependence of t_c^n on n gives us the speed of the phonobreather core's expansion; shown in Figure 5.15 for the left (a) and right (b) phonobreather tails of the IVP solution seen in Figure 5.14. From this figure we can see that the speed of this core drift seems to be constant in time i.e. the core grows linearly with time. The best fit lines in Figure 5.15 have equations

$$\text{Left:} \quad t_c^n = -0.26n + 3.16 \quad \text{Right:} \quad t_c^n = 0.24n - 4.21.$$

Since this system is symmetric about its midpoint we expect the left and right velocities to be the same and the differences are due to the nature of this approximation. Averaging the two drift velocities we get $v \approx 0.25$.

To ensure that this drift is not due to the specific numerical integrator we have used,

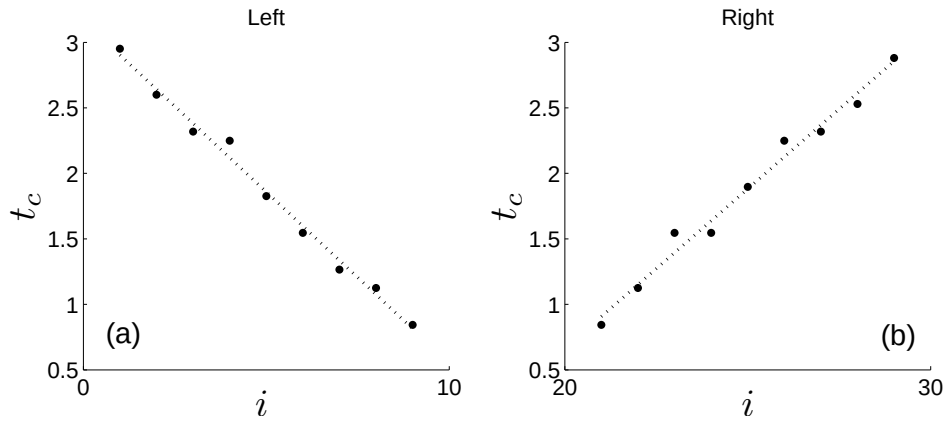

Figure 5.15: *Dependence of t_c^n (see text for the definition) on n showing that width of the phonobreather's core grows linearly with time.*

this analysis has been performed with two numerical integrators. The results just presented were calculated using Matlab's ode45 routine with abstol=1×10^{-8} and reltol= 1×10^{-6}. For comparison we have also done this analysis using a fourth order symplectic integrator (Leimkuhler & Reich 2004, p147) with a step size of $\delta t \approx 6.6 \times 10^{-4}$. Although the individual trajectories from these two integrators vary slightly near the phonobreather core, the behaviour is essentially the same and the mean core edge drift velocity for the symplectic integrator is $v \approx 0.27$.

This drift property tells us that although the exact phonobreather trajectory may be unstable, close to this trajectory in phase space we see interesting dynamical behaviour that has a chance of being observed experimentally.

5.5 Summary

This chapter considered some aspects of the time dependent behaviour of the mechanical lattice with vertical springs only shown in Figure 3.1, p33. This started by looking at the spectrum of small amplitude vibrations about the flat equilibrium state. We saw that the highest frequency linear modes have the longest spatial wavelength (Figure 5.2, p80) and that the frequencies of all the linear modes decrease with increasing load (Figure 5.1, p79). The numerical results of Section 5.2 then suggested that under dead loading conditions (i.e. controlled load p) all of the static equilibrium states found in the previous section are dynamically unstable except the flat equilibrium for $\lambda < \lambda^*_{N-1,N}$, where $\lambda^*_{N-1,N} \approx 4/\delta^2$ for large N. However, studying this mechanical system under rigid loading conditions may have a stabilising effect on some of these

static equilibrium states.

The second part of this chapter used knowledge of the spectrum of small amplitude vibrations of the mechanical lattice and the numerical method of Marin & Aubry (1996) to find spatially localised, time periodic solutions to the lattice's equations of motion. Examples of these solutions, called discrete breathers, that were both stable and unstable were given. Finally, by numerically continuing one of the stable breather solutions towards lower frequency values, phonobreather solutions were found in this lattice. One of these phonobreather solutions was found to be dynamically unstable, but despite this the nonlinear dynamic behaviour close to the exact phonobreather trajectory proved to be interesting and potentially observable in an experiment. This interesting behaviour consisted of a slowly growing spatially disordered phonobreather core which slowly enveloped the sinusoidal tails.

5.6 Appendix: Nonlinear oscillator amplitude frequency relation

In this appendix it is described how the amplitude frequency dependence of a general nonlinear oscillator with Hamiltonian

$$H_1(p,q) = p^2/2 + V(q) \tag{5.19}$$

for some potential function V was calculated in this work. The requirements on V are such that there is a fixed point at the origin of this dynamical system and that $H_1(p,q)$ has closed level sets in some region of this fixed point. First, the Hamiltonian (5.19) is transformed into the action angle, (I,ϕ) coordinate system (see (Arnold 1980, §50)) in which the Hamiltonian takes the simple form $H = H(I)$, and the equations of motion are given by

$$\dot{I} = \frac{\partial H}{\partial \phi} = 0 \quad \text{and} \quad \dot{\phi} = \frac{\partial H}{\partial I}.$$

This immediately gives us the angular frequency of the oscillations $\omega = \dot{\phi}$ with the period T given by $T = 2\pi/\dot{\phi}$.

The dynamical system evolves along level sets $H(p,q) = h$ and the action variable is given by the area enclosed by this level set

$$I(h) = \frac{1}{2\pi} \oint_{H(p,q)=h} p \, \mathrm{d}q$$

The angular frequency is then given by $\dot{\phi} = \frac{\partial H}{\partial I} = \left(\frac{\partial I}{\partial h}\right)^{-1}$. In general the period needs to be calculated numerically. To do this we use the reversibility ($H_1(-p,q) = H_1(p,q)$) of the Hamiltonian (5.19) to write

$$I(h) = \frac{1}{\pi} \int_{-q_1}^{q_2} \sqrt{2(h - V(q))} \, \mathrm{d}q$$

where q_1 and q_2, $q_1 < q_2$ give the coordinates of the intersection of the level set with value h and the q axis. Evaluating this numerically using a suitable quadrature algorithm (such as Matlab's adaptive Simpson quadrature function quad) for a grid of h values and then numerically differentiating gives an approximation to the nonlinear oscillators period.

Chapter 6

Static equilibrium states of a fourth order mechanical system

In the introduction and Chapter 4 we have seen how the static equilibrium states of two similar mechanical lattices behave. One, the system of Domokos & Holmes (1993) ((a) of Figure 1.1), has only torsional springs keeping unloaded equilibrium state flat, the other, the system studied in Chapter 4 ((b) of Figure 1.1) has only vertical springs keeping the unloaded equilibrium state flat. This chapter presents an introductory analysis to the mechanical system shown in Figure 6.1 that is a combination of these two simpler mechanical systems.

This chapter first considers the coordinates used to write down the mathematical model of the system shown in Figure 6.1. In Chapter 3, the simpler mechanical lattice with vertical springs was modelled using the vertical displacements of the pivots as coordinates; this required us to assume that $|\theta_n| < \pi/2$ for all n, where θ_n is the rotation of link n. In the paper by Domokos & Holmes (1993) the mechanical lattice with torsional springs only was modelled using the link angles, θ_n, as coordinates, and this required the restriction that the total end shortening of the system is not equal to the length of the system, i.e. $\mathcal{E} \neq L$. In order to obtain the full behaviour of the more complex mechanical lattice shown in Figure 6.1 we need to remove these restrictions and a mathematical model that allows this is developed in Section 6.1 below.

As just described, the previously considered mathematical models of the two simpler mechanical systems do not capture all of the behaviour of these mechanical lattices. Section 6.2, below, considers the behaviour of the more general mathematical model developed in Section 6.1 in the two limits that cause the more complex mechanical

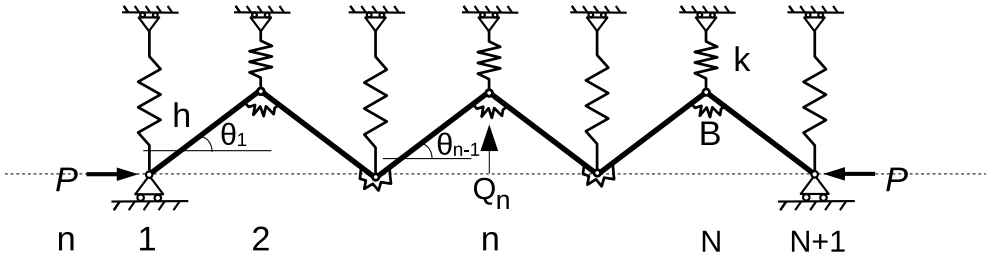

Figure 6.1: *The mechanical system of study in this chapter, with N links of length h, freely pin jointed pivots, vertical and torsional springs both of which act to keep the unloaded equilibrium state fully extended (i.e. length Nh) and flat.*

lattice to coincide with one of the simpler lattices. The limit $k_f = 0$ corresponds to removing the vertical springs and leads to the simpler lattice of Domokos & Holmes (1993) while the limit $k_b = 0$ corresponds to removing the torsional springs and leads to the mechanical lattice studied earlier in this thesis. Section 6.2 shows the additional behaviour that can be modelled using the more general model. We find that in the limit $k_b = 0$ there are a large number of additional equilibrium states that complicate the equilibrium states' bifurcation structure, and this behaviour is described for $N = 4$.

The second half of this chapter is more speculative, and points the way towards a discrete boundary value problem (discrete BVP) formulation for the static equilibrium states of the more complex mechanical lattice. The discrete BVPs that model the two simpler mechanical lattices are based on iterated maps of the plane, the iterated maps that model this more complex system map $\mathbb{R}^4$ to $\mathbb{R}^4$. Section 6.3 discusses the potential of, and pitfalls in extending the theory of discrete mechanics, used in successfully in chapters 3 and 4, to model this more complex lattice. We see that matching all possible lattice boundary constraints, as was seen in Chapter 3, is not straight forward. Despite this difficulty in applying the theory of discrete mechanics, via an ad hoc procedure we do derive a fully nonlinear discrete BVP that gives the static equilibrium states of the more complex mechanical lattice.

To demonstrate the utility of the discrete BVP approach in this more complex lattice, in Section 6.3.1 we consider the linear behaviour of this system and derive another discrete BVP that gives the conditions for bifurcation from the flat equilibrium state. By analogy with the analysis used in Chapter 4 we conjecture, with supporting numerical evidence, that there are $N - 1$ primary bifurcations from the flat equilibrium state, and derive the following analytic expression for the bifurcation loads:

$$p_{m,N} = \frac{2k_b + \frac{k_f}{2} - 4k_b \cos(\frac{m\pi}{N}) + 2k_b \cos^2(\frac{m\pi}{N})}{1 - \cos(\frac{m\pi}{N})}$$

for $m = 1, \ldots, N-1$, where k_f and k_b are the nondimensional stiffnesses of the foundation and torsional springs respectively.

Finally, we motivate further study of this fourth order mechanical lattice by presenting numerical results that demonstrate behaviour that is not observed in either of the two simpler mechanical lattices. The parameter values chosen for these numerical calculations are motivated by a convincing link with experimental values from the granular media literature (Hunt et al. (2009)). The numerical results show how the solutions on the first three, lowest load, primary solution branches behave. We see that the solutions buckle into initially sinusoidal shapes before localising with a localisation length scale between that of the whole system and an individual link. This wavelength appears to be set by the wavelength of the initial sinusoidal buckle. We also see that some of these static equilibrium states exhibit homoclinic snaking, where the load supported by the structure oscillates between two values as the as the end shortening of the structure gradually increases.

Before the work of this chapter is begun, it is important to note that the labelling convention for the pivots of the mechanical system has changed for this chapter. Now, as shown in Figure 6.1, pivot 1 corresponds to first pivot in the lattice and pivot $N+1$ corresponds to the last. Whereas, in previous chapters the first pivot was labelled with 0 and the last pivot with N.

6.1 Modelling

This section starts by writing down a mathematical model of the mechanical system shown in Figure 6.1. As described in the introduction and background sections (chapters 1 and 2) we are studying this system from several points of view; as a mechanical system, with full freedom to assume any link angle displacement, that you could build in the laboratory; as a toy model for more complex mechanical systems such as the lattice work of steel framed buildings or the force chains in granular media; and, as a mathematical exercise following the long tradition that simple mechanical systems have often lead to new and interesting mathematics. For the laboratory structure, we are assuming that our springs behave linearly, that there is no gravity and that the links are rigid. The vertical springs, which we call the foundation springs, always stay vertical and their bases slide horizontally with no friction to achieve this. We also assume that there is no friction in the pins linking the links. These are assumptions that would be impossible to satisfy completely, but could be approximated experimentally to reasonable accuracy.

With these thoughts in mind, we would like our mathematical model to shed light on all of the interpretations just discussed. Thus, below, we model this system initially in terms of the vertical pivot displacements Q_n, because these coordinates allow us to begin an analysis of the linear small displacement behaviour of this system (Section 6.3.1). These Q_n coordinates restrict us to link rotations in the range $(-\pi/2, \pi/2)$ and so we then model the system using the link rotations θ_n as the generalised coordinates to remove the link angle restriction.

We start writing down the potential energy of this system by summing the bending energy stored in the rotational springs U_b and the energy stored in the vertical foundation springs U_f, and subtracting the work done by the load $P\mathcal{E}$ where $\mathcal{E}$ gives the end shortening of the whole system. We do this first by using the vertical displacement coordinates Q_n as done in Chapter 4 to give

$$U_f = \sum_{n=1}^{N+1} \frac{k}{2} Q_n^2, \quad \mathcal{E} = Nh - h \sum_{n=1}^{N} \pm \sqrt{1 - \left(\frac{Q_{n+1} - Q_n}{h} \right)^2}. \tag{6.1}$$

where the $\pm$ arises due to the possibility of the angle θ_n being in either of the two ranges $[-\pi/2, \pi/2]$ or $(\pi/2, \pi) \cup (-\pi/2, \pi)$. The energy, U_b, in terms of the angles, θ_n, is given by

$$U_b = \sum_{n=2}^{N} \frac{B}{2} \Delta\theta_n^2$$

where $\Delta\theta_n = \theta_n - \theta_{n-1}$ for $n = 2, \ldots, N$. To write this in terms of the coordinates Q_n we use the relation $h \sin\theta_n = Q_{n+1} - Q_n$ to give

$$U_b = \sum_{n=2}^{N} \frac{B}{2} \left(\arcsin\left(\frac{Q_{n+1} - Q_n}{h} \right) - \arcsin\left(\frac{Q_n - Q_{n-1}}{h} \right) \right)^2.$$

Using these expressions and neglecting the constant terms we arrive at the potential energy

$$V_4^Q = \sum_{n=2}^{N} \frac{B}{2} \left(\arcsin\left(\frac{Q_{n+1} - Q_n}{h} \right) - \arcsin\left(\frac{Q_n - Q_{n-1}}{h} \right) \right)^2 + \sum_{n=1}^{N+1} \frac{k}{2} Q_n^2 + Ph \sum_{n=1}^{N} \pm \sqrt{1 - \left(\frac{Q_{n+1} - Q_n}{h} \right)^2}. \tag{6.2}$$

The equilibrium equations for this potential,

$$\frac{\partial V_4^Q}{\partial Q_n} = 0 \text{ for } n = 1, \ldots, N+1$$

are determined by the following derivatives of V_4^Q:

$$\begin{aligned}
\frac{\partial V_4^Q}{\partial Q_1} &= \frac{B}{h}\bar{h}(Q_2 - Q_1)\,\Delta_s(Q_1, Q_2, Q_3) + kQ_1 + P\bar{g}(Q_2 - Q_1) \\
\frac{\partial V_4^Q}{\partial Q_2} &= \frac{B}{h}\bar{h}(Q_3 - Q_2)\,\Delta_s(Q_2, Q_3, Q_4) - \frac{B}{h}\left(\bar{h}(Q_3 - Q_2) + \bar{h}(Q_2 - Q_1)\right)\Delta_s(Q_1, Q_2, Q_3) \\
&\quad + kQ_2 - P\bar{g}(Q_2 - Q_1) + P\bar{g}(Q_3 - Q_2) \\
\frac{\partial V_4^Q}{\partial Q_k} &= \frac{B}{h}\bar{h}(Q_k - Q_{k-1})\,\Delta_s(Q_{k-2}, Q_{k-1}, Q_k) \\
&\quad - \frac{B}{h}\left(\bar{h}(Q_{k+1} - Q_k) + \bar{h}(Q_k - Q_{k-1})\right)\Delta_s(Q_{k-1}, Q_k, Q_{k+1}) \\
&\quad + \frac{B}{h}\bar{h}(Q_{k+1} - Q_k)\,\Delta_s(Q_k, Q_{k+1}, Q_{k+2}) + k_f Q_k - P\bar{g}(Q_k - Q_{k-1}) + P\bar{g}(Q_{k+1} - Q_k) \\
\frac{\partial V_4^Q}{\partial Q_N} &= -\frac{B}{h}\left(\bar{h}(Q_{N+1} - Q_N) + \bar{h}(Q_N - Q_{N-1})\right)\Delta_s(Q_{N-1}, Q_N, Q_{N+1}) \\
&\quad + \frac{B}{h}\bar{h}(Q_N - Q_{N-1})\,\Delta_s(Q_{N-2}, Q_{N-1}, Q_N) + kQ_N - P\bar{g}(Q_N - Q_{N-1}) + P\bar{g}(Q_{N+1} - Q_N) \\
\frac{\partial V_4^Q}{\partial Q_{N+1}} &= \frac{B}{h}\bar{h}(Q_{N+1} - Q_N)\,\Delta_s(Q_{N-1}, Q_N, Q_{N+1}) + kQ_{N+1} - P\bar{g}(Q_{N+1} - Q_N).
\end{aligned} \tag{6.3}$$

Where

$$\bar{h}(x) = \left(1 - \left(\frac{x}{h}\right)^2\right)^{-1/2}, \ \bar{g}(x) = \frac{x}{h}\left(1 - \left(\frac{x}{h}\right)^2\right)^{-1/2}$$
$$\text{and } \Delta_s(x, y, z) = \arcsin\left(\frac{z - y}{h}\right) - \arcsin\left(\frac{y - x}{h}\right).$$

As in Chapter 4, we are considering constraints on the end of the lattice so that Q_1 and Q_{N+1} are vertically fixed, i.e $Q_1 = Q_{N+1} = 0$. In the above system, these constraints are are easily implemented by using the Lagrange multipliers μ_1 and μ_2 to give the new function $\bar{V}_4^Q = V_4^Q - \mu_1 Q_1 - \mu_2 Q_{N+1}$. The equilibrium equations for Q_1 and Q_{N+1} then give

$$\begin{aligned}
\frac{\partial \bar{V}_4^Q}{\partial Q_1} = \frac{\partial V_4^Q}{\partial Q_1} - \mu_1 &= 0 \Rightarrow \mu_1 = \frac{\partial V_4^Q}{\partial Q_1} \\
\frac{\partial \bar{V}_4^Q}{\partial Q_{N+1}} = \frac{\partial V_4^Q}{\partial Q_{N+1}} - \mu_2 &= 0 \Rightarrow \mu_2 = \frac{\partial V_4^Q}{\partial Q_{N+1}}.
\end{aligned}$$

Which means that implementing these constraints is equivalent to considering the $N-1$ equilibrium equations $\frac{\partial V_4^Q}{\partial Q_n} = 0$ for $n = 2, \ldots, N$ with the substitutions $Q_1 = Q_{N+1} = 0$.

There are several mathematical issues with the expressions (6.3); there is the unknown sign in the expression for the end shortening (6.1), and the fact that if $\theta_k = \pm\pi/2$ for some k $\partial V_4^Q/\partial Q_i$ is infinite for $i = k-1, k, k+1$ ($\theta_k = \pm\pi/2$ implies that $Q_{k+1} - Q_k = \pm h$ which implies that $h(Q_{k+1} - Q_k) = g(Q_{k+1} - Q_k) = \infty$). This leads us to save these equations for further analysis in Section 6.3.1 and, now, to remove these pathologies by modelling this system in terms of the link angles θ_n.

To find the equilibrium equations equivalent to (6.3) for the angles $\boldsymbol{\theta} = (\theta_1, \ldots, \theta_N)^{\mathrm{T}} \in \mathbb{R}^N$ we first determine the pivot displacements $\boldsymbol{Q} = (Q_1, \ldots, Q_{N+1})^{\mathrm{T}} \in \mathbb{R}^{N+1}$ from the angles $\boldsymbol{\theta}$. To do this there are several choices based on the relation $h \sin\theta_n = Q_{n+1} - Q_n$. Two of these choices calculate Q_n by summing $\sin\theta_n$ from either the left or right end of the system and are given by

$$\text{i) } Q_n = Q_1 + h\sum_{i=1}^{n-1} \sin\theta_i, \quad \text{or} \quad \text{ii) } Q_n = Q_{N+1} - h\sum_{i=n}^{N} \sin\theta_i,$$

where we use the convention that sums for which the upper limit is lower then the lower limit give the value zero. Each of these expressions contains a constant (Q_1 and Q_{N+1} respectively) which are discrete constants of 'integration', actually summation, in going from the N angle or gradient coordinates $\boldsymbol{\theta}$ to the $N+1$ displacement coordinates $\boldsymbol{Q}$. Each of these expressions gives special status to one end of the lattice, the lower end for i) and the upper end for ii). Since there is no such distinction in the physical system the transformation $\mathcal{S} : \mathbb{R}^N \times \mathbb{R} \to \mathbb{R}^{N+1}$ is now defined as a combination of these two expressions so that we retain the physical symmetry in our mathematical formulation:

$$\frac{Q_n}{h} = [\mathcal{S}(\boldsymbol{\theta}, c)]_n \equiv \frac{1}{2}\left(\sum_{i=1}^{n-1} \sin\theta_i - \sum_{i=n}^{N} \sin\theta_i\right) + c \tag{6.4}$$

where, again, we use the convention that sums for which the upper limit is lower then the lower limit give the value zero.

Continuing the modelling procedure now, the length of the system can be written in terms of the $\boldsymbol{\theta}$ coordinates to give

$$L(\boldsymbol{\theta}) = \sum_{n=1}^{N} \cos\theta_n, \tag{6.5}$$

the end shortening is then $\mathcal{E}(\boldsymbol{\theta}) = N - L(\boldsymbol{\theta})$. The potential energy of the mechanical system, neglecting constant terms, can be written in terms of the angle coordinates

thus

$$V_4^{\theta}(\boldsymbol{\theta}, c) = \sum_{n=1}^{N-1} \frac{B}{2}(\theta_{n+1} - \theta_n)^2 + Ph \sum_{n=1}^{N} \cos\theta_n + \frac{kh^2}{2}\mathcal{S}(\boldsymbol{\theta}, c) \cdot \mathcal{S}(\boldsymbol{\theta}, c)$$

where $\cdot$ represents the vector dot product. The end constraints for the mechanical lattice

$$Q_1 = h[\mathcal{S}(\boldsymbol{\theta}, c)]_1 = 0 \quad \text{and} \quad Q_{N+1} = h[\mathcal{S}(\boldsymbol{\theta}, c)]_{N+1} = 0$$

are enforced using the Lagrange multipliers $\bar{\mu}_1$ and $\bar{\mu}_2$ (where the bar tells reminds us that these are the dimensional Lagrange multipliers) to give the new function

$$\bar{\mathcal{L}}(\boldsymbol{\theta}, c, \bar{\mu}_1, \bar{\mu}_2) = \sum_{n=1}^{N-1} \frac{B}{2}(\theta_{n+1} - \theta_n)^2 + Ph \sum_{n=1}^{N} \cos\theta_n + \frac{kh^2}{2}\mathcal{S}(\boldsymbol{\theta}, c) \cdot \mathcal{S}(\boldsymbol{\theta}, c) \\ - \bar{\mu}_1 h[\mathcal{S}(\boldsymbol{\theta}, c)]_1 - \bar{\mu}_2 h[\mathcal{S}(\boldsymbol{\theta}, c)]_{N+1}.$$

Physically these Lagrange multipliers give the unknown vertical reaction forces at the left end support $\bar{\mu}_1$ and right end support $\bar{\mu}_2$ (Maddocks (1984)). To non-dimensionalise the dimensional equations seen so far in this section we have two choices

$$U_n = \frac{Q_n}{h}, \quad k_b = \frac{B}{kh^2}, \quad p = \frac{P}{kh}, \quad \mu_{1,2} = \frac{\bar{\mu}_{1,2}}{kh} \tag{6.6}$$

or

$$U_n = \frac{Q_n}{h}, \quad k_f = \frac{kh^2}{B}, \quad p = \frac{Ph}{B}, \quad \mu_{1,2} = \frac{\bar{\mu}_{1,2}h}{B}. \tag{6.7}$$

The first of these scales the spring constant for the foundation springs to one and leaves two non-dimensional parameters: one for the load, p, and one for the bending stiffness, k_b. The second of these scales the bending spring constant to one and leaves a different two non-dimensional parameters: one for the load, p, and one for the foundation stiffness, k_f. We want to consider both the limits $k_b = 0$ and $k_f = 0$ and so we write this function in non-dimensional form as follows

$$\mathcal{L}(\boldsymbol{\theta}, c, \mu_1, \mu_2) = \sum_{n=1}^{N-1} \frac{k_b}{2}(\theta_{n+1} - \theta_n)^2 + p \sum_{n=1}^{N} \cos\theta_n + \frac{k_f}{2}\mathcal{S}(\boldsymbol{\theta}, c) \cdot \mathcal{S}(\boldsymbol{\theta}, c) \\ - \mu_1[\mathcal{S}(\boldsymbol{\theta}, c)]_1 - \mu_2[\mathcal{S}(\boldsymbol{\theta}, c)]_{N+1}. \tag{6.8}$$

By setting $k_b = 1$ in the above equations we have the nondimensionalisation (6.7), and by setting $k_f = 1$ while allowing k_b and p to vary we have the nondimensionalisation (6.6). In this way we are able to consider the two simpler limits that have already been discussed in this thesis.

The static equilibrium states of the mechanical system are found by solving the $N+3$ equilibrium equations,

$$\frac{\partial \mathcal{L}}{\partial \theta_n} = 0 \quad \text{for} \quad n = 1, \ldots, N, \quad \frac{\partial \mathcal{L}}{\partial c} = 0, \quad \frac{\partial \mathcal{L}}{\partial \mu_1} = 0, \quad \text{and} \quad \frac{\partial \mathcal{L}}{\partial \mu_2} = 0, \tag{6.9}$$

for the $N+3$ unknowns $\{\theta_n\}_{n=1}^N$, c, μ_1 and μ_2 where

$$\begin{aligned}
\frac{\partial \mathcal{L}}{\partial \theta_1} &= -k_b(\theta_2 - \theta_1) - p\sin\theta_1 + k_f \left[\mathcal{S}^{\mathrm{T}} \frac{\partial \mathcal{S}}{\partial \boldsymbol{\theta}}\right]_1 - \mu_1 \frac{\partial [\mathcal{S}]_1}{\partial \theta_1} - \mu_2 \frac{\partial [\mathcal{S}]_{N+1}}{\partial \theta_1} \\
\frac{\partial \mathcal{L}}{\partial \theta_n} &= -k_b(\theta_{n+1} - 2\theta_n + \theta_{n-1}) - p\sin\theta_n + k_f \left[\mathcal{S}^{\mathrm{T}} \frac{\partial \mathcal{S}}{\partial \boldsymbol{\theta}}\right]_n - \mu_1 \frac{\partial [\mathcal{S}]_1}{\partial \theta_n} - \mu_2 \frac{\partial [\mathcal{S}]_{N+1}}{\partial \theta_n} \\
\frac{\partial \mathcal{L}}{\partial \theta_N} &= k_b(\theta_N - \theta_{N-1}) - p\sin\theta_N + k_f \left[\mathcal{S}^{\mathrm{T}} \frac{\partial \mathcal{S}}{\partial \boldsymbol{\theta}}\right]_N - \mu_1 \frac{\partial [\mathcal{S}]_1}{\partial \theta_N} - \mu_2 \frac{\partial [\mathcal{S}]_{N+1}}{\partial \theta_N} \\
\frac{\partial \mathcal{L}}{\partial c} &= k_f \mathcal{S} \cdot \frac{\partial \mathcal{S}}{\partial c} - \mu_1 \frac{\partial [\mathcal{S}]_1}{\partial c} - \mu_2 \frac{\partial [\mathcal{S}]_{N+1}}{\partial c} \\
\frac{\partial \mathcal{L}}{\partial \mu_1} &= -[\mathcal{S}]_1 \\
\frac{\partial \mathcal{L}}{\partial \mu_2} &= -[\mathcal{S}]_{N+1},
\end{aligned} \tag{6.10}$$

for $n = 2, \ldots, N-1$. Some the terms in the above equations involving $\mathcal{S}$ can be written in terms of the angles θ_n and simplified as follows. From the definition of $\mathcal{S}(\boldsymbol{\theta}, c)$, (6.4), we see that

$$\frac{\partial [\mathcal{S}(\boldsymbol{\theta})]_n}{\partial c} = 1 \quad \forall\ n \tag{6.11}$$

$$\frac{\partial [\mathcal{S}(\boldsymbol{\theta})]_n}{\partial \theta_k} = \frac{1}{2} \begin{cases} \cos\theta_k & k \leq n-1 \\ -\cos\theta_k & k \geq n. \end{cases} \tag{6.12}$$

Equations (6.10) above then become

$$\frac{\partial \mathcal{L}}{\partial \theta_1} = -k_b(\theta_2 - \theta_1) - p\sin\theta_1 + k_f \left[\mathcal{S}^{\mathrm{T}} \frac{\partial \mathcal{S}}{\partial \boldsymbol{\theta}}\right]_1 + (\mu_1 - \mu_2)\cos\theta_1 \tag{6.13a}$$

$$\frac{\partial \mathcal{L}}{\partial \theta_n} = -k_b(\theta_{n+1} - 2\theta_n + \theta_{n-1}) - p\sin\theta_n + k_f \left[\mathcal{S}^{\mathrm{T}} \frac{\partial \mathcal{S}}{\partial \boldsymbol{\theta}}\right]_n + (\mu_1 - \mu_2)\cos\theta_n \tag{6.13b}$$

$$\frac{\partial \mathcal{L}}{\partial \theta_N} = k_b(\theta_N - \theta_{N-1}) - p\sin\theta_N + k_f \left[\mathcal{S}^{\mathrm{T}} \frac{\partial \mathcal{S}}{\partial \boldsymbol{\theta}}\right]_N + (\mu_1 - \mu_2)\cos\theta_N \tag{6.13c}$$

$$\frac{\partial \mathcal{L}}{\partial c} = k_f \sum_{i=1}^{N+1} [\mathcal{S}]_i - (\mu_1 + \mu_2) \tag{6.13d}$$

$$\frac{\partial \mathcal{L}}{\partial \mu_1} = -[\mathcal{S}]_1 \tag{6.13e}$$

$$\frac{\partial \mathcal{L}}{\partial \mu_2} = -[\mathcal{S}]_{N+1}. \tag{6.13f}$$

for $n = 2, \ldots, N-1$. The terms that have k_f as a factor in equations (6.13) can be written out in the $\boldsymbol{\theta}$ coordinates using (6.4) and (6.12) to give

$$\left[\mathcal{S}^{\mathrm{T}} \frac{\partial \mathcal{S}}{\partial \boldsymbol{\theta}}\right]_n = \frac{\cos\theta_n}{2} \sum_{k=n+1}^{N+1} \left[\frac{1}{2}\left(\sum_{i=1}^{k-1} \sin\theta_i - \sum_{i=k}^{N} \sin\theta_i\right) + c\right] - \frac{\cos\theta_n}{2} \sum_{k=1}^{n} \left[\frac{1}{2}\left(\sum_{i=1}^{k-1} \sin\theta_i - \sum_{i=k}^{N} \sin\theta_i\right) + c\right]. \tag{6.14}$$

Equations (6.13) will be studied in the remaining sections of this chapter. To connect the solutions to these equations with the physical shape of the lattice we introduce the coordinates X_n and Y_n where X_n gives the horizontal displacement of each lattice point and Y_n gives the vertical displacement:

$$X_1 = 0, \quad X_n = h\sum_{i=1}^{n-1} \cos\theta_n, \quad Y_0 = 0, \quad \text{and} \quad Y_n = h\sum_{i=1}^{n-1} \sin\theta_n. \tag{6.15}$$

As we saw at the end of Chapter 4 mechanical lattice systems have many symmetries that allow us to find groups of related solutions. Some properties and symmetries of equations (6.13) are presented in the next section.

6.1.1 Properties and symmetries

The mechanical system of Figure 6.1 has some symmetries that we expect to be apparent in the equations (6.13). For instance, there are no forces that act to distinguish

between up and down, and so if a particular equilibrium solution is not invariant under reflection about the horizontal load line we expect there to be another solution that is the reflection of the original one. Similarly, there is no distinction between the left and right ends of the system and so we expect to find solutions related under the transformation defined by $R : \mathbb{R}^N \to \mathbb{R}^N$ such that $[R(\boldsymbol{\theta})]_n = \theta_{N+1-n}$. The following list defines several transformations which take a solution to equations (6.13) given by $(\boldsymbol{\theta}, c, \mu_1, \mu_2, k_f, k_b, p)$ and then returns another, distinct solution.

$$\begin{aligned}
S_1 &= (\ \boldsymbol{\theta} \quad\quad\ , \quad c, \quad \mu_1, \quad \mu_2, \quad k_f, \quad k_b, \quad p\ ) \\
T_1 &: S_1 \to (\ \boldsymbol{\theta} \quad\quad\ , \quad c, -\mu_1, -\mu_2, -k_f, -k_b, -p\ ) \\
T_2^{\pm} &: S_1 \to (\ \boldsymbol{\theta} \pm 2\pi, \quad c, \quad \mu_1, \quad \mu_2, \quad k_f, \quad k_b, \quad p\ ) \\
T_3^{\pm} &: S_1 \to (\ \boldsymbol{\theta} \pm \pi\ , \quad c, \quad \mu_1, \quad \mu_2, -k_f, -k_b, \quad p\ ) \\
T_4 &: S_1 \to (\ \pi - \boldsymbol{\theta}\ , -c, \quad \mu_1, \quad \mu_2, \quad k_f, \quad k_b, -p\ ) \\
T_5 &: S_1 \to (\ R(\boldsymbol{\theta})\ , -c, \quad \mu_2, \quad \mu_1, \quad k_f, \quad k_b, \quad p\ )
\end{aligned}$$

We can also combine these operations to create further solutions, and one of the more important compositions is $T_c = T_4 \circ T_3^- \circ T_1$

$$T_c \ : S_1 \to (\ -\boldsymbol{\theta} \quad\quad\ , -c, -\mu_1, -\mu_2, \quad k_f, \quad k_b, \quad p\ ).$$

Proving that the solution S_1 transformed by T_1– T_4 is a solution to equations (6.13) is straight forwardly achieved by substituting the expressions for these transformed solutions into (6.13) and using the fact that S_1 is a solution. To prove $T_5(S_1)$ is a solution we take a different approach, given in the following lemma.

Lemma 6.1. *Assuming the solution S_1, defined above, is a stationary point of the function $\mathcal{L}$ (6.8) then $T_5(S_1)$ is also a stationary point of $\mathcal{L}$.*

Proof. We first prove that $[\mathcal{S}(R(\boldsymbol{\theta}), -c)]_{N+2-m} = -[\mathcal{S}(\boldsymbol{\theta}, c)]_m$. From the definitions of R (above) and $\mathcal{S}$ (6.4) we have

$$[\mathcal{S}(R(\boldsymbol{\theta}), -c)]_n = \frac{1}{2}\left(\sum_{i=1}^{n-1} \sin\theta_{N+1-i} - \sum_{i=n}^{N} \sin\theta_{N+1-i}\right) - c,$$

and letting $k = N + 1 - i$ gives

$$[\mathcal{S}(R(\boldsymbol{\theta}), -c)]_n = \frac{1}{2}\left(\sum_{k=N+2-n}^{N} \sin\theta_k - \sum_{k=1}^{N+1-n} \sin\theta_k\right) - c.$$

Similarly, we now let $m = N + 2 - n$ to leave

$$\begin{aligned}[\mathcal{S}(R(\boldsymbol{\theta}), -c)]_{N+2-m} &= \frac{1}{2}\left(\sum_{k=m}^{N} \sin\theta_k - \sum_{k=1}^{m-1} \sin\theta_k\right) - c \\ &= -[\mathcal{S}(\theta, c)]_m, \end{aligned} \tag{6.16}$$

thus proving that $[\mathcal{S}(R(\boldsymbol{\theta}), -c)]_{N+2-m} = -[\mathcal{S}(\boldsymbol{\theta}, c)]_m$. Now consider $\mathcal{L}(T_5(P))$, where $P = (\boldsymbol{\theta}, c, \mu_1, \mu_2, k_f, k_b, p)$ is not necessarily a stationary point of $\mathcal{L}$ with respect to $\boldsymbol{\theta}$,c, μ_1 and μ_2:

$$\begin{aligned}\mathcal{L}(T_5(P)) = &\sum_{n=1}^{N-1} \frac{k_b}{2}(\theta_{N-n} - \theta_{N+1-n})^2 + p\sum_{n=1}^{N} \cos\theta_{N+1-n} \\ &+ \frac{k_f}{2}\mathcal{S}(R(\boldsymbol{\theta}), -c) \cdot \mathcal{S}(R(\boldsymbol{\theta}), -c) - \mu_2[\mathcal{S}(R(\boldsymbol{\theta}), -c)]_1 - \mu_1[\mathcal{S}(R(\boldsymbol{\theta}), -c)]_{N+1}\end{aligned}$$

letting $k = N - n$ in the first two sums and using the relation (6.16) tells us that

$$\begin{aligned}\mathcal{L}(T_5(P)) &= \sum_{k=1}^{N-1} (\theta_{k+1} - \theta_k)^2 + p\sum_{k=1}^{N} \cos\theta_k + \frac{k_f}{2}\mathcal{S}(\boldsymbol{\theta}, c) \cdot \mathcal{S}(\boldsymbol{\theta}, c) \\ &\qquad - \mu_1[\mathcal{S}(\boldsymbol{\theta}, c)]_1 - \mu_2[\mathcal{S}(\boldsymbol{\theta}, c)]_{N+1} \\ &= \mathcal{L}(P).\end{aligned}$$

Since the Jacobian of the transformation T_5 is non-singular for all P, if the point P is a stationary point of $\mathcal{L}$ then so is $T_5(P)$. □

The symmetries of equations (6.13), just introduced, will be referred to in the next sections and also help to reduce the parameter ranges that need to be considered when calculating bifurcation diagrams for solutions to equations (6.13). We finish this section with the observation that it is possible to solve the equations (6.9) for c, and also to show that all solutions to these equations satisfy

$$\sum_{i=1}^{N} \sin\theta_i = 0. \tag{6.17}$$

To do this we use (6.13e) and (6.13f) with the definition of $\mathcal{S}(\boldsymbol{\theta}, c)$ (6.4) to give

$$\mathcal{S}(\boldsymbol{\theta}) = \frac{1}{2}\left(-\sum_{i=1}^{N} \sin\theta_i\right) + c = 0 \quad \text{and} \quad \mathcal{S}(\boldsymbol{\theta}) = \frac{1}{2}\left(\sum_{i=1}^{N} \sin\theta_i\right) + c = 0.$$

These cannot be simultaneously satisfied with $c \neq 0$, and so $c = 0$, which in turn gives the condition (6.17).

6.1.2 Numerical method

In Chapter 4 the static equilibrium states of a mechanical system were found using a discrete boundary value problem method that enabled the location of all of the static equilibrium states that satisfied $|\theta_n| < \pi/2$ for all n. In this chapter the link angle restriction is lifted, but the search for solutions is now restricted to solutions that lie on branches that are connected to the $\theta_n = 0 \ \forall \ n$ equilibrium state. These solutions are found using the continuation code Auto (Doedel et al. (1997)). To do this we form the function $\boldsymbol{F}(\boldsymbol{\theta}, c, \mu_1, \mu_2; k_b, k_f, p) : \mathbb{R}^{N+3} \times \mathbb{R}^3 \rightarrow \mathbb{R}^{N+3}$ where $\boldsymbol{F} = (f_1, \ldots, f_{N+3})^{\mathrm{T}}$ and

$$f_n = \frac{\partial \mathcal{L}}{\partial \theta_n} \text{ for } n = 1, \ldots, N, \quad f_{N+1} = \frac{\partial \mathcal{L}}{\partial c}, \quad f_{N+2} = \frac{\partial \mathcal{L}}{\partial \mu_1}, \quad \text{and} \quad f_{N+3} = \frac{\partial \mathcal{L}}{\partial \mu_2}. \tag{6.18}$$

We then use Auto to trace the dependence of the solution $(\boldsymbol{\theta}, \mu_1, \mu_2, c)$ on the relevant parameter, either k_b, k_f or p, by using pseudo-arc-length continuation on the solutions to $\boldsymbol{F} = \boldsymbol{0}$. It is straight forward to find a solution from which to start this continuation: we use the zero solution $S_0 = (\boldsymbol{0}, 0, 0, 0, k_f, k_b, p)$.

6.2 Limits $k_f = 0$ and $k_b = 0$

In Section 6.1 we derived the equations (6.13) that give the static equilibrium states of the compound mechanical system of Figure 6.1. Physically, it is clear that the simpler mechanical systems of Domokos & Holmes (1993) and Chapter 4 are limits of this more complex system, and in this section it is shown how, and under what conditions, the mathematical behaviour of these simpler systems relates to that of equations (6.13). We also use the more general formulation of Section 6.1 to investigate the solutions that have been previously excluded in the modelling of the simpler mechanical systems. This allows us to investigate solutions for which $|\theta_n| \geq \pi/2$ in the limit $k_b = 0$, and solutions satisfying $L = 0$, where L is the horizontal distance between the two ends of the system, in the limit $k_f = 0$.

6.2.1 Limit $k_f = 0$

The limit $k_f = 0$ gives the system of Domokos & Holmes (1993) discussed in Section 2.2 and shown in (a) of Figure 1.1. We now see how equations (2.3) are found as a subset of (6.13), and see that equations (6.13) admit extra solutions. The relation of these extra solutions to those analysed in Domokos & Holmes (1993) is then presented. To start, k_f is set to zero in equations (6.13a)–(6.13f) to get

$$\frac{\partial \mathcal{L}}{\partial \theta_1} = -k_b(\theta_2 - \theta_1) - p\sin\theta_1 + (\mu_1 - \mu_2)\cos\theta_1 \tag{6.19a}$$

$$\frac{\partial \mathcal{L}}{\partial \theta_n} = -k_b(\theta_{n+1} - 2\theta_n + \theta_{n-1}) - p\sin\theta_n + (\mu_1 - \mu_2)\cos\theta_n \tag{6.19b}$$

$$\frac{\partial \mathcal{L}}{\partial \theta_N} = k_b(\theta_N - \theta_{N-1}) - p\sin\theta_N + (\mu_1 - \mu_2)\cos\theta_N \tag{6.19c}$$

$$\frac{\partial \mathcal{L}}{\partial c} = -(\mu_1 + \mu_2) \tag{6.19d}$$

$$\frac{\partial \mathcal{L}}{\partial \mu_1} = -[\mathcal{S}]_1 \tag{6.19e}$$

$$\frac{\partial \mathcal{L}}{\partial \mu_2} = -[\mathcal{S}]_{N+1}. \tag{6.19f}$$

The solutions to these equations come in two types (Domokos & Holmes (1993), Maddocks (1984)).

Type I solutions satisfy $\mu_1 = \mu_2 = 0$ and are the solutions considered by Domokos & Holmes (1993).

Type II solutions satisfy $\mu_1 = -\mu_2 \neq 0$ and their behaviour is described below.

We can see that with $\mu_1 = \mu_2 = 0$ equations (6.19a) – (6.19c) reduce to the equations (2.3) of the introduction. The solutions to these equations are of type I and are considered by Domokos & Holmes (1993).

It is also interesting to consider the type II solutions. An argument of Maddocks (1984) tells us that all type II solutions satisfy $L(\boldsymbol{\theta}) = 0$, i.e. $\mu_1 = -\mu_2 \neq 0$ implies $L(\boldsymbol{\theta}) = 0$. Consider the system shown in Figure 6.2; rotational equilibrium about each each of the end pivots leads to the equations $F_1 L(\boldsymbol{\theta}) = 0$ and $F_2 L(\boldsymbol{\theta}) = 0$. Interpreted physically, the Lagrange multipliers μ_1 and μ_2 are proportional to the vertical reaction forces F_1 and F_2 (Maddocks (1984)) and so $\mu_i \neq 0$ implies $F_i \neq 0$ for $i = 1, 2$. These, and the equations for rotation equilibrium just derived, tell us that $\mu_1 \neq 0$ or $\mu_2 \neq 0$ implies

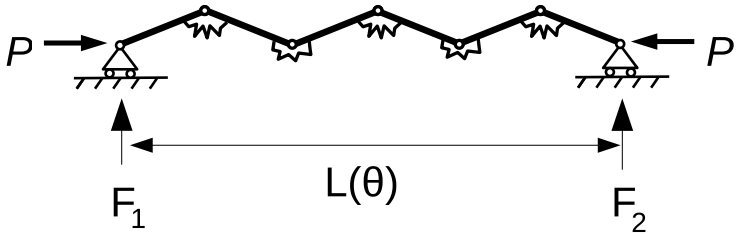

Figure 6.2: *Physically the Lagrange multipliers in equations (6.13) and (6.19) tell us the reaction forces at the supports at the ends of the lattice.*

$L(\boldsymbol{\theta}) = 0$.

If we now consider Figure 6.2 with $L(\boldsymbol{\theta}) = 0$ we can see that, since there are no torsional springs at the end pivots, the system is free to rotate around the, now coincident, end pivots. This implies that there is at least one one parameter family of solutions to equations (6.19), parametrised by the angle of rotation of the whole lattice about the end pivots. In fact, for each solution to equations (6.19) that satisfies $L(\boldsymbol{\theta}) = 0$ there is such a one parameter family of solutions, as shown in the next lemma.

Lemma 6.2. *Assume that there exists a solution to the equations (6.19) of the form* $S_0 = (\boldsymbol{\theta}, c, \mu_1^0, -\mu_1^0, 0, k_b, p^0)$ *with* $L(\boldsymbol{\theta}) = 0$ *then there is a one parameter family of solutions to the equations (6.19) parametrised by the angle* ϕ *given by*

$$S(\phi) = (\boldsymbol{\theta} + \phi, c, \mu_1(\phi), -\mu_1(\phi), 0, k_b, p(\phi)) \quad \textit{where} \tag{6.20}$$

$$\begin{aligned} p(\phi) &= p^0 \cos\phi + 2\mu_1^0 \sin\phi \\ \mu_1(\phi) = -\mu_2(\phi) &= \frac{1}{2}(2\mu_1^0 \cos\phi - p^0 \sin\phi). \end{aligned}$$

Proof. The proof is based on the trigonometric identities

$$\sin(\theta_n + \phi) = \sin\theta_n \cos\phi + \cos\theta_n \sin\phi \quad \text{and} \quad \cos(\theta_n + \phi) = \cos\theta_n \cos\phi - \sin\theta_n \sin\phi.$$

Using these identities we have

$$\begin{aligned} -p^0 \sin(\theta_n + \phi) + 2\mu_1^0 \cos(\theta_n + \phi) & \\ &= -\sin\theta_n (p^0 \cos\phi + 2\mu_1^0 \sin\phi) + \cos\theta_n (2\mu_1^0 \cos\phi - p^0 \sin\phi) \\ &= -p(\phi) \sin\theta_n + 2\mu_1(\phi) \cos\theta_n \end{aligned}$$

This along with $\mu_1 = -\mu_2$ implies that the solution $S(\phi)$ satisfies the first N equations

of the equation group (6.19). The solution clearly satisfies $\mu_1 + \mu_2 = 0$ and so now we consider the final two equations of equation group (6.19), the constraint equations.

$$\begin{aligned} -[\mathcal{S}(\boldsymbol{\theta}, 0)]_1 = [\mathcal{S}(\boldsymbol{\theta}, 0)]_{N+1} &= \frac{1}{2}\sum_{i=1}^{N} \sin\theta_i \\ \Rightarrow [\mathcal{S}(\boldsymbol{\theta} + \phi, 0)]_{N+1} &= \frac{1}{2}\sum_{i=1}^{N} (\sin\theta_i \cos\phi + \cos\theta_i \sin\phi) \\ &= \frac{\cos\phi}{2}\sum_{i=1}^{N} \sin\theta_i + \frac{\sin\phi}{2}\sum_{i=1}^{N} \cos\theta_i \\ &= \cos\phi[\mathcal{S}(\boldsymbol{\theta}, 0)]_{N+1} + \frac{\sin\phi}{2} L(\theta). \end{aligned}$$

Since we assume that S_0 is a solution and that $L(\theta) = 0$, the constraint equations are clearly satisfied, and $S(\phi)$ is a one parameter family of solutions. □

An example of how one of these branches of type II solutions bifurcates from the bifurcation diagram of type I solutions found by Domokos & Holmes (1993) is shown in Figure 6.3. This figure shows all the type I solution branches that are connected to the flat equilibrium state with $k_b = 1$ and $N = 6$ in blue. The red line is a branch of type II solutions that bifurcates from the blue lines at the points marked with black crosses. The solutions on the type II branch at the points indicated by purple circles are shown in Figure 6.4, which plots the solutions on this branch in physical X_n, Y_n where X_n and Y_n are given by (6.15). We can see in Figure 6.4 that along this type II branch the solutions are simply rotations of the same shape about the origin (denoted by $\odot$ in Figure 6.4).

The blue, type one, solution branches of Figure 6.3 demonstrate several symmetries of the equations (6.19) above. Firstly, replacing θ_n with $-\theta_n$ for all n (T_c of Section 6.1.1) leaves these equations unchanged explaining the reflection symmetry of the bifurcation diagram about the $\theta_1 = 0$ axis. Also, if we send $\theta_n \to \theta_n \pm 2\pi$ for all n ($T_2^{\pm}$) the equations are invariant, explaining the horizontal 2π periodicity, and finally, the transformation $\theta_n \to \pi - \theta_n$, $p \to -p$ (T_4) is also an invariant explaining why the diagram is the same under reflection about the $p = 0$ axis and translation horizontally by π.

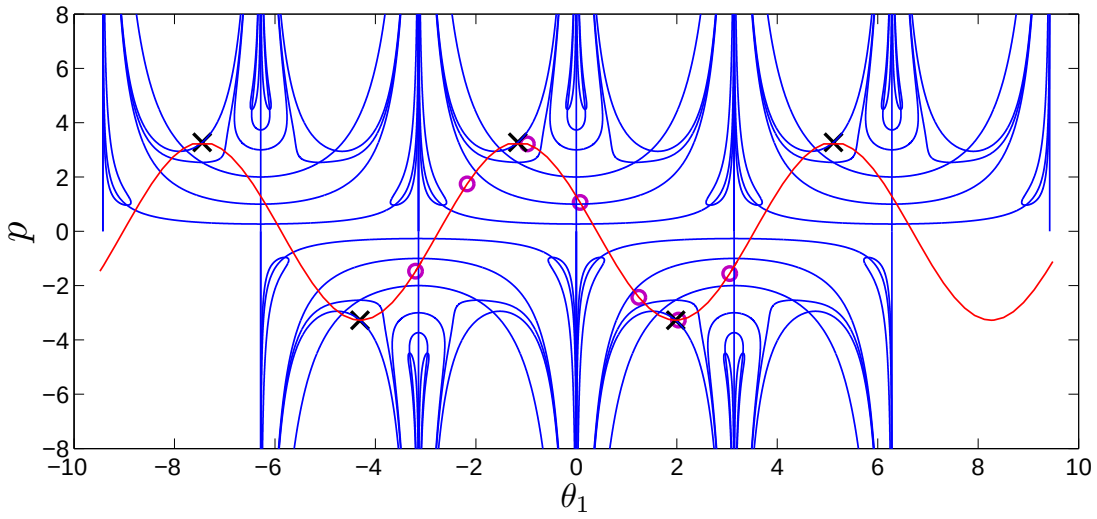

Figure 6.3: *Type one solution branches connected to the flat equilibrium state are shown here in blue. The black crosses show where one branch of type two solutions bifurcates from the type one branches. The purple circles show the locations of the solutions shown in Figure 6.4 on the branch.*

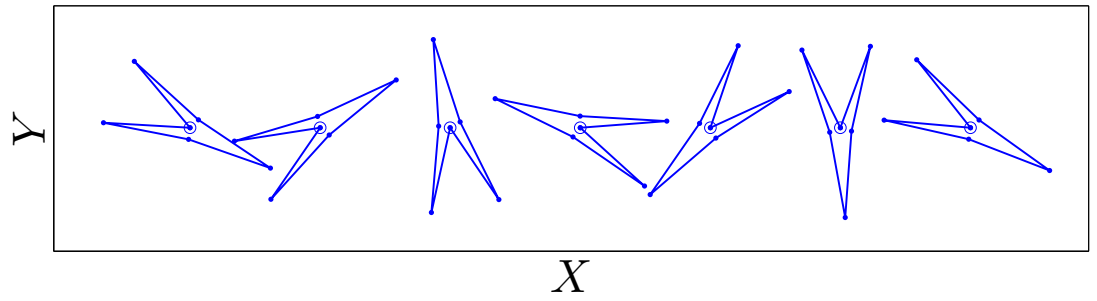

Figure 6.4: *These solutions are the type two solutions at the purple circles shown in Figure 6.3. We can see that this branch simply rotates the same shape about the origin denoted by* $\odot$ *in the above plot.*

6.2.2 Limit $k_b = 0$

The limit $k_b = 0$ of the compound mechanical system shown in Figure 6.1 removes the torsional springs and results in the mechanical system with vertical springs only studied in Chapter 4 ((b) of Figure 1.1). The static equilibrium states of this system were studied, in detail, in Chapter 4 under the assumption that $|\theta_n| > \pi/2$ for all n. In this section we use equations (6.13) to start to understand the behaviour of this mechanical system without this link angle restriction. We see below that the removal of the link angle restriction results in a large number of extra static equilibrium states, and in the next section we ask whether any of these extra static equilibrium states will survive the perturbation caused by non-zero k_b and persist in the more complex mechanical system of Figure 6.1.

First, we show how, by assuming $|\theta_n| < \pi/2$ and taking a nonlinear forward difference of equations (6.13) with $k_b = 0$, we can derive the equilibrium equations for the mechanical system studied in Chapters 3 and 4 from equations (6.13).

Setting $k_b = 0$ in (6.13) gives

$$\begin{aligned}
\frac{\partial \mathcal{L}}{\partial \theta_1} &= -p\sin\theta_1 + k_f\left[\mathcal{S}\frac{\partial \mathcal{S}}{\partial \boldsymbol{\theta}}\right]_1 + \frac{1}{2}(\mu_1 - \mu_2)\cos\theta_1 \\
\frac{\partial \mathcal{L}}{\partial \theta_n} &= -p\sin\theta_n + k_f\left[\mathcal{S}\frac{\partial \mathcal{S}}{\partial \boldsymbol{\theta}}\right]_n + \frac{1}{2}(\mu_1 - \mu_2)\cos\theta_n \\
\frac{\partial \mathcal{L}}{\partial \theta_N} &= -p\sin\theta_N + k_f\left[\mathcal{S}\frac{\partial \mathcal{S}}{\partial \boldsymbol{\theta}}\right]_N + \frac{1}{2}(\mu_1 - \mu_2)\cos\theta_N \\
\frac{\partial \mathcal{L}}{\partial c} &= k_f\mathcal{S}\cdot\frac{\partial \mathcal{S}}{\partial c} - \mu_1 - \mu_2 \\
\frac{\partial \mathcal{L}}{\partial \mu_1} &= -[\mathcal{S}]_1 \\
\frac{\partial \mathcal{L}}{\partial \mu_2} &= -[\mathcal{S}]_{N+1}.
\end{aligned} \tag{6.21}$$

We are going to continue by evaluating the nonlinear forward difference

$$\frac{1}{\cos\theta_{n+1}}\frac{\partial \mathcal{L}}{\partial \theta_{n+1}} - \frac{1}{\cos\theta_n}\frac{\partial \mathcal{L}}{\partial \theta_n} \tag{6.22}$$

for $n = 1, \ldots, N-1$, but first we present a lemma which will be useful in doing this.

Lemma 6.3.

$$\frac{1}{\cos\theta_{n+1}}\left[\mathcal{S}\frac{\partial \mathcal{S}}{\partial \boldsymbol{\theta}}\right]_{n+1} - \frac{1}{\cos\theta_n}\left[\mathcal{S}\frac{\partial \mathcal{S}}{\partial \boldsymbol{\theta}}\right]_n = -[\mathcal{S}(\boldsymbol{\theta}, 0)]_n$$

Proof. From (6.14) we have

$$\frac{1}{\cos\theta_{n+1}}\left[\mathcal{S}\frac{\partial\mathcal{S}}{\partial\boldsymbol{\theta}}\right]_{n+1} - \frac{1}{\cos\theta_n}\left[\mathcal{S}\frac{\partial\mathcal{S}}{\partial\boldsymbol{\theta}}\right]_n =$$
$$\frac{1}{2}\sum_{k=n+2}^{N+1}\left[\frac{1}{2}\left(\sum_{i=1}^{k-1}\sin\theta_i - \sum_{i=k}^{N}\sin\theta_i\right)+c\right] - \frac{1}{2}\sum_{k=1}^{n+1}\left[\frac{1}{2}\left(\sum_{i=1}^{k-1}\sin\theta_i - \sum_{i=k}^{N}\sin\theta_i\right)+c\right]$$
$$-\frac{1}{2}\sum_{k=n+1}^{N+1}\left[\frac{1}{2}\left(\sum_{i=1}^{k-1}\sin\theta_i - \sum_{i=k}^{N}\sin\theta_i\right)+c\right] - \frac{1}{2}\sum_{k=1}^{n}\left[\frac{1}{2}\left(\sum_{i=1}^{k-1}\sin\theta_i - \sum_{i=k}^{N}\sin\theta_i\right)+c\right]$$

$$\begin{aligned}
&= \frac{1}{4}\left[-\sum_{i=1}^{n}\sin\theta_i + \sum_{i=n+1}^{N}\sin\theta_i - \sum_{i=1}^{n}\sin\theta_i + \sum_{i=n+1}^{N}\sin\theta_i\right]\\
&= \frac{-1}{2}\left[\sum_{i=1}^{n}\sin\theta_i - \sum_{i=n+1}^{N}\sin\theta_i\right]\\
&= -[\mathcal{S}(\boldsymbol{\theta},0)]_n,
\end{aligned}$$

where in the last step we have used the definition of $\mathcal{S}$, (6.4). □

If we now assume $|\theta_n| < \pi/2$ we are able to evaluate the nonlinear forward difference (6.22) for $n = 1,\ldots,N-1$ to give

$$-p(\tan\theta_{n+1} - \tan_{\theta_n}) - k_f[\mathcal{S}(\boldsymbol{\theta},0)]_n = 0. \tag{6.23}$$

These are the equilibrium equations of the system studied in chapters 3 and 4 in terms of the link angles θ_n rather than the vertical pivot displacements U_n. To write these equations in terms of the displacements U_n we use the inverse of the transformation $\mathcal{S}$ which is valid only if $|\theta_n| < \pi/2$ for all n (remembering that $c = 0$) given by

$$U_{n+1} - U_n = \sin\theta_n \text{ for } n = 1,\ldots,N-1.$$

With this, equations (6.23) become exactly equations (5.2) of Chapter 5:

$$-p\left(\frac{U_{n+1}-U_n}{\sqrt{1-(U_{n+1}-U_n)^2}} - \frac{U_n - U_{n-1}}{\sqrt{1-(U_n-U_{n-1})^2}}\right) - k_f U_n = 0$$

with $U_1 = U_{N+1} = 0$. As a book-keeping exercise we now examine the constraint equations, the last three equations of (6.21), under the above transformation from the

θ_1	θ_2	θ_3	θ_4
0	0	0	0
0	0	0	π
0	0	π	0
0	0	π	π
0	π	0	0
0	π	0	π
0	π	π	0
0	π	π	π

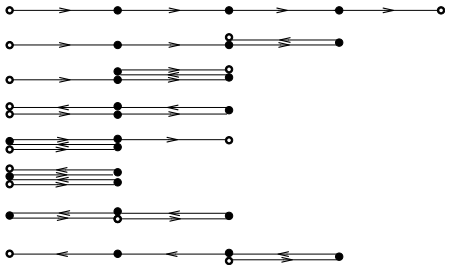

Figure 6.5: *These are the flat equilibria of the mechanical system of Figure 6.1 that are distinct under the transformations T_1-T_5 for $k_b = 0$, $N = 4$. The table gives the θ coordinates and the picture gives a schematic of the physical displacements. The black dots represent internal pivots while the dots with holes represent the end pivots.*

$\boldsymbol{\theta}$ coordinates to the $\boldsymbol{U}$ coordinates. These constraint equations become

$$\begin{aligned} k_f \sum_{n=1}^{N+1} U_n - (\mu_1 + \mu_2) &= 0, \\ U_1 = 0 \text{ and } U_{N+1} &= 0. \end{aligned}$$

The first of these gives the condition that the whole system be in vertical equilibrium and the last two are simply the boundary constraints we have imposed on this system.

We have now seen how the equations used previously to model this mechanical system with $k_b = 0$ arise under the assumption that $|\theta_n| < \pi/2$ for all n; the next part of this section considers the behaviour of equations (6.21), which do not require this assumption.

The first thing we notice is that there are now significantly more flat equilibrium states that exist for all parameter values: from the trivial flat state we are able to rotate any link by π and arrive at another flat equilibrium state. This gives 2^N equilibrium states, however, half of these are related under the transformation T_3 of Section 6.1.1. This gives 2^{N-1} states distinct under the symmetry operations $T_1 - T_4$. These solutions can be represented as $(\{\theta_n\}, 0, 0, 0, k_f, 0, p)$ where $\theta_n \in \{0, \pi\}$ for all n and $k_f, p \in \mathbb{R}$. As an example Figure 6.5 enumerates these states for a system with $N = 4$.

For even N there is another set of static equilibrium states with all of the links vertical. These solutions are given by $\theta_n = s_n \pi/2$ where $s_n = \pm 1$ (independent of n) such that $\sum_n s_n = 0$. Half of these solutions are related by the compound transformation T_{c1} and so there are $N!/\left(2(N/2)!(N/2)!\right)$ transformation distinct ways of writing these solutions. The three solutions for $N = 4$ are

θ_1	θ_2	θ_3	θ_4
$\frac{\pi}{2}$	$\frac{\pi}{2}$	$-\frac{\pi}{2}$	$\frac{\pi}{2}$
$\frac{\pi}{2}$	$-\frac{\pi}{2}$	$\frac{\pi}{2}$	$-\frac{\pi}{2}$
$\frac{\pi}{2}$	$-\frac{\pi}{2}$	$-\frac{\pi}{2}$	$\frac{\pi}{2}$

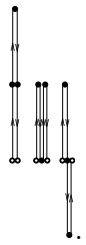

The number of these two types of equilibria present in this mechanical system grows exponentially with N as the following table confirms.

N	2^{N-1}	$N!/\left(2(\frac{N}{2})!(\frac{N}{2})!\right)$
4	8	3
6	32	10
10	512	126
16	32768	6435
50	$\approx 5.63 \times 10^{14}$	$\approx 6.32 \times 10^{13}$
100	$\approx 6.34 \times 10^{29}$	$\approx 5.04 \times 10^{28}$

Clearly, trying to understand the global bifurcation diagram for this system with N large is going to be difficult and so here we present a small sample of the behaviour for small N.

We now look at some of the bifurcation behaviour for this system with $N = 4$. First, we consider the primary branches from the flat $(0, 0, 0, 0)$ state studied in Chapter 4 with the branch range extended to include angles $|\theta_i| \geq \pi/2$. In the spirit of Chapter 4 where the solutions were uniquely specified by $W_0 = \tan\theta_1$ and $\lambda \propto 1/p$ we plot these bifurcation diagrams in the (θ_1, p) plane. Figure 6.6 shows this extended bifurcation diagram. Proposition 4.9 of Chapter 4 tells us that as $p \to 0$ the $\lceil (N-1)/2 \rceil$ highest load primary bifurcations satisfy $\theta_1 \to \pi/2$, which can be seen for branches ① and ②, of Figure 6.6. Figure 6.7 shows some of the solutions on the branches of Figure 6.6 as you move further from the bifurcation with the flat equilibrium state. At $\theta_1 = \pi/2$, since in this example N is even, we reach the equilibrium $(\pi/2, \pi/2, -\pi/2, -\pi/2)$, listed in the table above. The other primary branches now form closed loops in this parameter space and some connect to one of the flat equilibrium states listed in Figure 6.5. We can see from solution three of branch ③ in Figure 6.7 that this branch connects the $(0, 0, 0, 0)$ flat equilibrium with the $(0, \pi, \pi, 0)$ flat equilibrium.

This type of behaviour is also seen as we consider bifurcations from the other flat equilibrium states. For example, Figure 6.8 shows the primary bifurcations from the

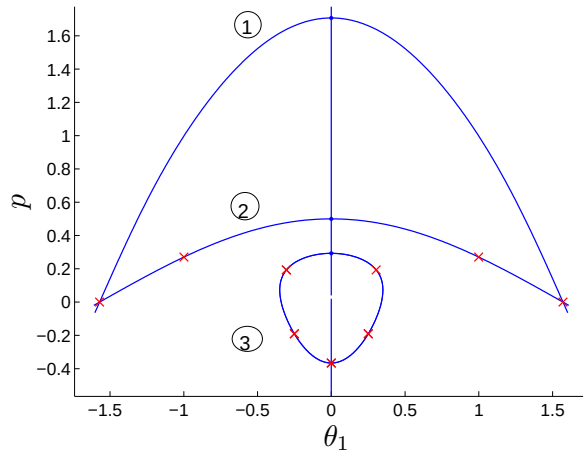

Figure 6.6: *Primary branches that bifurcate, at the points denoted by* $\cdot$ *, from the flat equilibrium state given by* $(0, 0, 0, 0)$*. There are secondary bifurcations at the points marked by* $\times$*.*

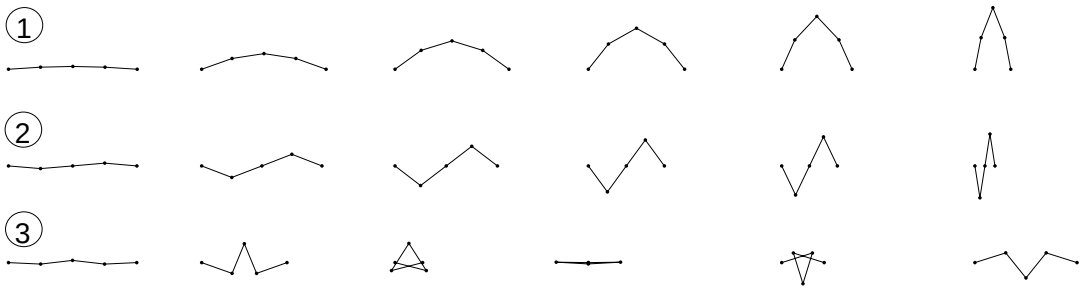

Figure 6.7: *These are the solutions along the branches in shown in Figure 6.6. The left most solutions are on the branches in Figure 6.6 just after bifurcation from the flat state* $\theta_1 = 0$*.*

$(0, 0, 0, \pi)$ flat equilibrium, and Figure 6.9 shows some of the solutions as you move along the bifurcating branches. Again, we see that some of the primary branches at higher loads satisfy $\theta_1 \to \pi/2$ as $p \to 0$ while others (branches ② and ③) form closed loops in parameter space. These closed branches bifurcate onto other branches of flat equilibrium states given by $(0, \pi, 0, \pi)$ in the case of branch ② or a symmetry transformed version of $(0, 0, 0, \pi)$ in the case of branch ③.

In this way, with primary and secondary bifurcations from each flat equilibrium state connecting these states to other flat equilibrium states we can start to understand the bifurcation structure of this system.

6.2.3 Persistence of equilibrium states

In the previous sections the bifurcation diagrams for two limits of the equation system (6.13) were reviewed and extended. In particular, in the limit $k_b = 0$, in Section 6.2.2,

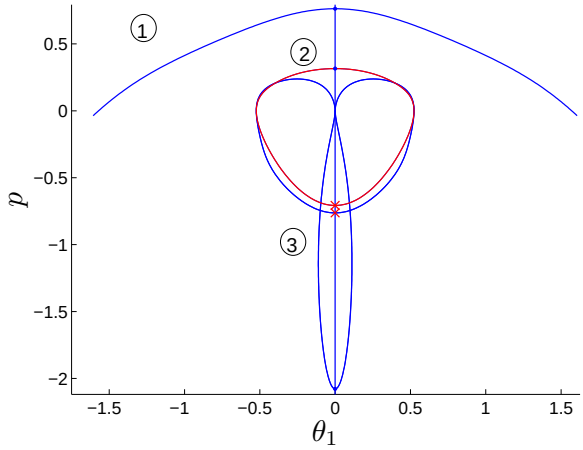

Figure 6.8: *Primary branches that bifurcate, at the points denoted by $\cdot$, from the flat equilibrium state given by $(0, 0, 0, \pi)$. There are secondary bifurcations at the points marked by $\times$.*

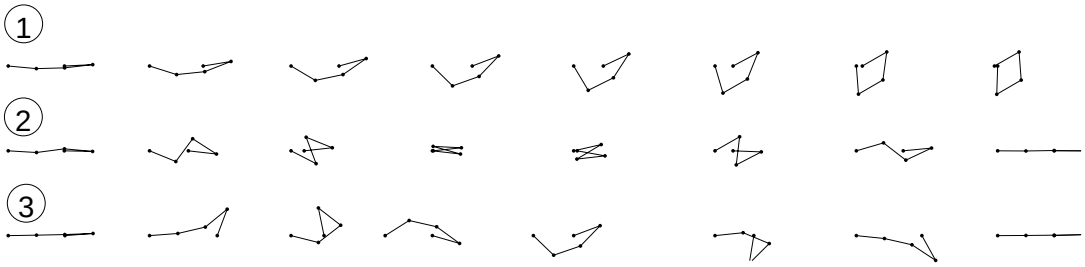

Figure 6.9: *These are the solutions along the branches shown in Figure 6.8. The left most solutions are on the branches in Figure 6.8 just after bifurcation from the flat state $\theta_1 = 0$.*

without the restriction $|\theta_n| < \pi/2$ for all n, many simple static equilibrium states were found, the number growing exponentially with the number of links N. The question now is, what do the limits $k_b = 0$ and $k_f = 0$ tell us about the full system of equations (6.13)? More specifically, do the equilibrium states found in the two limits above persist into regions of non-zero k_f or k_b? We can answer this for small enough k_f or k_b by using the implicit function theorem, and considering the function $\boldsymbol{F}$ defined in Section 6.1.2. If we have a solution to $\boldsymbol{F} = \boldsymbol{0}$ at $k_f = 0$ then the implicit function theorem states that we can parametrise this solution locally in terms of k_f as long as the Jacobian of $\boldsymbol{F}$ at the original solution, when $k_f = 0$, is non-singular i.e. it is a regular point of the corresponding bifurcation diagram.

In Section 6.2.1 we saw that the type II solutions existed on branches of regular points with a countable number of bifurcations onto branches of type I solutions, and in Section 6.2.2 we found that static equilibrium states of the type listed in Figure 6.5 also existed on branches of regular points with a bifurcation structure qualitatively similar to that of the extended flat state. We therefore expect these equilibrium states to persist into regions of non-zero k_f and k_b respectively.

The situation is different for the vertical equilibrium states introduced in Section 6.2.2. We now prove that the Jacobian of F is singular for these vertical equilibrium states and so we do not expect these equilibrium states to survive the perturbation induced by small but non-zero bending stiffness k_b.

To prove this we consider the structure of the Jacobian of $\boldsymbol{F}$. The Jacobian of $\boldsymbol{F}$ has the following structure, where $m = 1, \ldots, N$ is the row index and $n = 1, \ldots, N$ is the column index,

$$\boldsymbol{F}' = \begin{pmatrix} & & \uparrow & \uparrow & \uparrow \\ & \frac{\partial f_m}{\partial \theta_n} & \frac{\partial f_m}{\partial c} & \frac{\partial f_m}{\partial \mu_1} & \frac{\partial f_m}{\partial \mu_2} \\ & & \downarrow & \downarrow & \downarrow \\ \leftarrow & \frac{\partial f_{N+1}}{\partial \theta_n} \rightarrow & \frac{\partial f_{N+1}}{\partial c} & \frac{\partial f_{N+1}}{\partial \mu_1} & \frac{\partial f_{N+1}}{\partial \mu_2} \\ \leftarrow & \frac{\partial f_{N+2}}{\partial \theta_n} \rightarrow & \frac{\partial f_{N+2}}{\partial c} & \frac{\partial f_{N+2}}{\partial \mu_1} & \frac{\partial f_{N+2}}{\partial \mu_2} \\ \leftarrow & \frac{\partial f_{N+3}}{\partial \theta_n} \rightarrow & \frac{\partial f_{N+3}}{\partial c} & \frac{\partial f_{N+3}}{\partial \mu_1} & \frac{\partial f_{N+3}}{\partial \mu_2} \end{pmatrix},$$

where the functions f_m for $m = 1, \ldots, N+3$ are given, in order, by equations (6.13). Using equations (6.13), the definition of $\mathcal{S}(\boldsymbol{\theta}, c)$, (6.4), and equation (6.14) we can

evaluate the last three columns and last three rows of the above Jacobian to give

$$F' = \begin{pmatrix} & & \uparrow & \uparrow & \uparrow \\ & \frac{\partial f_m}{\partial \theta_n} & \frac{1}{2}k_f(N+1-2m)\cos\theta_m & \cos\theta_m & -\cos\theta_m \\ & & \downarrow & \downarrow & \downarrow \\ \leftarrow & \frac{\partial f_{N+1}}{\partial \theta_n} \rightarrow & k_f(N+1) & -1 & -1 \\ \leftarrow & -\frac{1}{2}\cos\theta_n \rightarrow & -1 & 0 & 0 \\ \leftarrow & +\frac{1}{2}\cos\theta_n \rightarrow & -1 & 0 & 0 \end{pmatrix}.$$

If we now consider the type II equilibrium states of the previous section for which $\theta_n = \pm\pi/2$ we can see that since $\cos(\pm\pi/2) = 0$ the last two rows of the above above matrix will be identical and so the matrix is singular. This violates the conditions of the implicit function theorem and so we don't expect these equilibrium states to survive the perturbation of non-zero bending stiffness.

6.3 Discrete boundary value problems

In Chapter 4 the static equilibrium states of a 'simple' mechanical lattice were studied using a discrete boundary value problem. In this section we discuss the possibility of using a discrete boundary value problem to model the static equilibrium states of the more complex mechanical lattice seen in Figure 6.1. Two methods are discussed; the first is an extension of the ideas of discrete mechanics used in Chapter 3, the second method is ad hoc, and an example of a discrete BVP that models the static equilibrium states of the mechanical system of Figure 6.1 is given. Each of these methods has its advantages and disadvantages and these are discussed below.

Higher order discrete mechanics

The authors Sun & Qin (2003) and Benito et al. (2006) develop a higher order analog of the discrete mechanics used in Chapter 3. By 'higher order' we mean that the potential energy function is extended from the form used in Chapter 3,

$$V = \sum_{i=1}^{N-1} L_d(Q_i, Q_{i+1}), \tag{6.24}$$

to have the form

$$V_d = \sum_{i=1}^{N-1} L_d^{(4)}(Q_i, Q_{i+1}, Q_{i+2}). \tag{6.25}$$

Here we say that $L_d^{(4)}$ is a 'second order' discrete Lagrangian by analogy with continuous second order Lagrangians of the form $L(u, \dot{u}, \ddot{u})$. A symplectic map which shares many of the symmetries of our mechanical system can then be derived from the discrete Lagrangian $L_d^{(4)}$, and this symplectic map maps $\mathbb{R}^4$ to $\mathbb{R}^4$. As we saw in Chapter 3, some care had to be taken to get the stationary points of the potential energy of the mechanical lattice to coincide with those of (6.24). These considerations were related to the type of constraints on the end of the mechanical lattice, and all possible end constraints (free and fixed pivots at each end of the lattice) were eventually brought into the form (6.24) by considering some extended potential functions. This procedure becomes more difficult for the more complex mechanical system of this chapter, because there are more end constraints to consider. We have to choose whether the displacement and torque at each end of the lattice is free or fixed. Also, to write the potential energy of this more complex mechanical lattice in the form (6.25) we have to use the pivot displacements Q_n as coordinates (compare the potentials (6.2) and (6.8)) which restricts us to the link angle range $|\theta_n| < \pi/2$. We now illustrate these points.

If we attempt to write the potential energy (6.2) in the form (6.25) we have some choice which we postpone by introducing the extra parameters a_1, a_2, a_3 and b_1, b_2, where $a_1 + a_2 + a_3 = 1$ and $b_1 + b_2 = 1$. This then gives

$$\begin{aligned} V_4^Q = \sum_{n=1}^{N-1} L_d^{(4)}(Q_n, Q_{n+1}, Q_{n+2}) - \frac{k_f}{2}(a_1 Q_{N+1}^2 + a_3 Q_1^2) \\ + Phb_1\sqrt{1 - \left(\frac{Q_2 - Q_1}{h}\right)^2} + Phb_2\sqrt{1 - \left(\frac{Q_{N+1} - Q_N}{h}\right)^2} \end{aligned} \tag{6.26}$$

with

$$\begin{aligned} L_d^{(4)}(Q_n, Q_{n+1}, Q_{n+2}) = \frac{B}{2}\left(\arcsin\left(\frac{Q_{n+2} - Q_{n+1}}{h}\right) - \arcsin\left(\frac{Q_{n+1} - Q_n}{h}\right)\right)^2 \\ + \frac{k_f}{2}\left(a_1 Q_{n+2}^2 + a_2 Q_{n+1}^2 + a_3 Q_n^2\right) \\ + Ph\left(b_1\sqrt{1 - \left(\frac{Q_{n+2} - Q_{n+1}}{h}\right)^2} + b_2\sqrt{1 - \left(\frac{Q_{n+1} - Q_n}{h}\right)^2}\right). \end{aligned}$$

This is where we can determine the restrictions that this formalism imposes. In order

for the stationary points of the functions V_d (6.25) and V_4^Q (6.26) to coincide we require that they only differ by a constant. Comparing (6.26) with (6.25) we can see that the values of the parameters a_1, a_2, a_3, b_1 and b_2 have an impact on the boundary conditions that this formalism can model. These restrictions are summarised in the following table.

Parameter Value	Boundary conditions/restriction
$a_1 \neq 0$	Q_{N+1} – fixed
$a_3 \neq 0$	Q_1 – fixed
$b_1 \neq 0$	Q_1, Q_2 – fixed
$b_2 \neq 0$	Q_{N+1}, Q_N – fixed

In this chapter we are interested in the fixed Q_1 and Q_{N+1} and free Q_N and Q_2 boundary conditions, but from the table above we see that we cannot do this without setting $b_1 = b_2 = 0$ which violates the $b_1 + b_2 = 1$ condition stated above. This shows us that, for this formulation to be able to model the boundary conditions considered in this chapter further work is required. This work might attempt to derive extended potential functions as was done in Chapter 3 that allow all possible boundary constraints to be modelled. Of course, with Q_1, Q_2, Q_N and Q_{N+1} fixed this method could be used now.

Ad hoc method

The method of discrete mechanics described above appears to be fundamentally restricted to consider the behaviour for $|\theta_n| < \pi/2$. If we allow the Lagrange multipliers of equations (6.13) to appear as parameters in our discrete boundary value problem we can lift this restriction and model the boundary conditions shown in Figure 6.1.

If we let

$$\begin{aligned}
x_n^{(1)} &= \theta_n \\
x_n^{(2)} &= [\mathcal{S}(\boldsymbol{\theta}, 0)]_n = \frac{1}{2}\left(\sum_{i=1}^{n-1} \sin x^{(1)} - \sum_{i=n}^{N} \sin x^{(1)}\right) \\
x_n^{(3)} &= \frac{1}{2}\left(\sum_{i=n+1}^{N} x_i^{(2)} - \sum_{i=1}^{n} x_i^{(2)}\right) \\
x_n^{(4)} &= \theta_{n+1} - \theta_n
\end{aligned}$$

then the system of equations (6.13) is equivalent to the following discrete boundary

value problem

$$\boldsymbol{X}_{n+1} = \Phi(\boldsymbol{X}_n) \quad \text{with} \tag{6.27}$$

$$\boldsymbol{X}_1 = \begin{pmatrix} a \\ 0 \\ b \\ 0 \end{pmatrix} \quad \text{and} \quad \boldsymbol{X}_{N+1} = \begin{pmatrix} c \\ 0 \\ d \\ 0 \end{pmatrix} \tag{6.28}$$

$$\tag{6.29}$$

for some $a, b, c, d \in \mathbb{R}$. The map Φ is given by

$$\Phi : \begin{pmatrix} x^{(1)} \\ x^{(2)} \\ x^{(3)} \\ x^{(4)} \end{pmatrix} \to \begin{pmatrix} x^{(1)} + x^{(4)} + \frac{1}{k_b}\left(k_f x^{(3)} \cos x^{(1)} - p \sin x^{(1)}\right) \\ x^{(2)} + \sin x^{(1)} \\ x^{(3)} - (x^{(2)} + \sin x^{(1)}) \\ x^{(4)} + \frac{1}{k_b}\left(k_f x^{(3)} \cos x^{(1)} - p \sin x^{(1)} + (\mu_1 - \mu_2) \cos x^{(1)}\right) \end{pmatrix}. \tag{6.30}$$

The difficulty with this method is that this discrete boundary value problem has to be solved subject to the constraint given by equation (6.13d):

$$\mu_1 + \mu_2 = k_f \sum_{i=1}^{N+1} x_n^{(2)}.$$

We have just seen two potential methods for modelling the fully nonlinear static equilibrium behaviour of the mechanical lattice of Figure 6.1 using a discrete boundary value problem. Considering the fully nonlinear behaviour for all possible link angles and parameter values causes some of the problems described above. In the next section we see that considering the linear behaviour, which is sufficient to determine the bifurcations from the flat equilibrium state, is simpler. Considering this linear behaviour allows us to derive an analytic expression for the load values at which we expect bifurcations from the flat equilibrium.

6.3.1 Linear behaviour

In this section we consider the linear behaviour of the static equilibrium states of the compound mechanical system of Figure 6.1 about the extended, flat, zero equilibrium state. We do this by using the pivot displacements, $\boldsymbol{Q}$, as the generalised coordinates describing the state of the system and then taking a first order approximation of the

nonlinear equilibrium equations (6.3) determined earlier in this chapter. These linear equilibrium are used to derive a linear map $\Phi : \mathbb{R}^4 \to \mathbb{R}^4$, which in turn is then use to define a discrete boundary value problem that gives the linear behaviour of the static equilibrium states. The behaviour of the map Φ is then investigated in the following sections.

To approximate the fully nonlinear equations (6.3) we use the first order approximations

$$\bar{h}(x) = 1 + \mathcal{O}(x^2), \quad \bar{g}(x) = x + \mathcal{O}(x^3)$$

$$\Delta_s(x_1, x_2, x_3) = x_3 - 2x_2 - x_1 + \mathcal{O}((x_3 - x_2)^3) + \mathcal{O}((x_2 - x_1)^3),$$

and solve for the constraints $U_1 = 0$ and $U_{N+1} = 0$ to remove the first and last equations of (6.3) to give the $N - 1$ linear equilibrium equations

$$0 = -k_b(U_3 - 2U_2 + U_1) + k_b(U_4 - 3U_3 + 3U_2 - U_1) + p(U_3 - 2U_2 + U_1) + k_f U_2 \tag{6.31}$$

$$0 = k_b(U_{n+2} - 4U_{n+1} + 6U_n - 4U_{n-1} + U_{n-2}) + p(U_{n+1} - 2U_n + U_{n-1}) + k_f U_n \tag{6.32}$$

$$\begin{aligned} 0 = -k_b(U_{N+1} - 2U_N + U_{N-1}) - k_b(U_{N+1} - 3U_N + 3U_{N-1} - U_{N-2}) \\ + p(U_{N+1} - 2U_N + U_{N-1}) + k_f U_N \end{aligned} \tag{6.33}$$

for $n = 3, \ldots, N - 1$ with $U_1 = 0$ and $U_{N+1} = 0$. We now turn the fourth order difference equation (6.32) into four first order difference equations by defining the new variables x_n^i $i = 1, \ldots, 4$ thus

$$\begin{aligned} x_n^{(1)} &= U_n && \text{for } n = 1, \ldots, N+1 \\ x_n^{(2)} &= U_{n+1} - U_n && \text{for } n = 1, \ldots, N \\ x_n^{(3)} &= U_{n+1} - 2U_n + U_{n-1} && \text{for } n = 2, \ldots, N \\ x_n^{(4)} &= U_{n+2} - 3U_{n+1} + 3U_n - U_{n-1} && \text{for } n = 2, \ldots, N-1. \end{aligned}$$

Rewriting these expressions solely in terms of the variables x_n^i gives

$$\begin{aligned} x_n^{(2)} &= x_{n+1}^{(1)} - x_n^{(1)} && \text{for } n = 1, \ldots, N \\ x_n^{(3)} &= x_n^{(2)} - x_{n-1}^{(2)} && \text{for } n = 2, \ldots, N \\ x_n^{(4)} &= x_{n+1}^{(3)} - x_n^{(3)} && \text{for } n = 2, \ldots, N-1, \end{aligned}$$

and the final map update is given by the difference equation (6.32) above to give

$$\begin{aligned} 0 &= k_b\left(x_n^{(4)} - x_{n-1}^{(4)}\right) + px_n^{(3)} + k_f x_n^{(1)} && \text{or} \\ x_n^{(4)} &= x_{n-1}^{(4)} + \frac{1}{k_b}(k_f x_n^{(1)} + px_n^{(3)}) && \text{for} \quad n = 3, \ldots, N-1. \end{aligned} \tag{6.34}$$

To verify that the boundary constraints, given by equations (6.31) and (6.33) above, are satisfied we notice that $x_1^{(3)} = 0$ implies $x_1^{(4)} = x_2^{(3)}$ and that $x_{N+1}^{(3)} = 0$ implies $x_N^{(4)} = -x_N^{(3)}$. We can then extend the range of validity of (6.34) to include $n = 2$ and $n = N$ with the conditions $x_1^{(3)} = 0$ and $x_{N+1}^{(3)} = 0$. This verifies that the boundary equations, (6.31) and (6.33) written in terms of x_n^i thus

$$\begin{aligned} 0 &= k_b(x_2^{(4)} - x_2^{(3)}) + px_2^{(3)} + k_f x_2^{(1)} \\ 0 &= k_b(-x_N^{(3)} - x_{N-1}^{(4)}) + px_N^{(3)} + k_f x_N^{(1)}, \end{aligned}$$

are satisfied.

This information can now be used to define a discrete boundary value problem that gives the linear behaviour of the system. If we define $\boldsymbol{X_n} = \left(x_n^{(1)}, x_n^{(2)}, x_n^{(3)}, x_n^{(4)}\right)^{\mathrm{T}}$ then $\boldsymbol{X_{n+1}} = \Phi(\boldsymbol{X_n})$ where

$$\Phi = \begin{pmatrix} 1 & 1 & 0 & 0 \\ 0 & 1 & 1 & 1 \\ 0 & 0 & 1 & 1 \\ -\frac{k_f}{k_b} & -\frac{k_f}{k_b} & -\frac{p}{k_b} & 1 - \frac{p}{k_b} \end{pmatrix}. \tag{6.35}$$

To satisfy the boundary constraints we require $\boldsymbol{X_1} = (0, a, 0, b)^{\mathrm{T}}$ and $\boldsymbol{X_{N+1}} = (0, c, 0, d)^{\mathrm{T}}$ for some $a, b, c, d \in \mathbb{R}$. We now go on to use this map to determine the load values of the primary bifurcations from the extended, flat equilibrium.

6.3.2 Primary bifurcations

In this section we determine the bifurcations from the zero equilibrium of the mechanical lattice in Figure 6.1 using a method similar to that used in Section 4.2.2 of Chapter 4. We define a bifurcation problem $g(\boldsymbol{z}; p, k_f, k_b) = 0$ where $\boldsymbol{z}, g \in \mathbb{R}^2$, with

$$g(\boldsymbol{z}; p, k_f, k_b) = P_1 \Phi^N P_2 \boldsymbol{z} \tag{6.36}$$

and Φ is defined in the previous section (6.35) and

$$P_1 = \begin{pmatrix} 1 & 0 & 0 & 0 \\ 0 & 0 & 1 & 0 \end{pmatrix} \quad P_2 = \begin{pmatrix} 0 & 0 \\ 1 & 0 \\ 0 & 0 \\ 0 & 1 \end{pmatrix}.$$

Bifurcation points from the zero solution $\boldsymbol{z} = \mathbf{0}$ are then parameter values for which the matrix

$$\left.\frac{\partial g}{\partial \boldsymbol{z}}\right|_{\boldsymbol{z}=\mathbf{0}}$$

is singular. Physically, we are interested in the buckling process that occurs as p is increased at fixed k_f and k_b, thus p is the relevant bifurcation parameter. We do not give proofs of when $\mathrm{d}g/\mathrm{d}z = 0$, but by analogy with the second order example of Chapter 4 we conjecture that this occurs at point where the eigenvalues of the matrix Φ pass through roots of unity. We give numerical evidence in the next section that this is indeed the case.

We now look for the p values at which we can write one of the eigenvalues of Φ in the form $\lambda = \exp(i\theta)$ where $\theta = m\pi/N$ for $m = 1, \ldots, N-1$. The characteristic polynomial of the matrix Φ is given by

$$k_b\lambda^4 + \lambda^3(p - 4k_b) + \lambda^2(6k_b - 2p + k_f) + \lambda(p - 4k_b) + k_b = 0, \tag{6.37}$$

and if we substitute the ansatz $\lambda = \exp(\mathrm{i}\theta)$ into this expression we get

$$\begin{aligned} k_b\left(\mathrm{e}^{2\mathrm{i}\theta} + \mathrm{e}^{-2\mathrm{i}\theta}\right) + \left(\mathrm{e}^{\mathrm{i}\theta} + \mathrm{e}^{-\mathrm{i}\theta}\right)(p - 4k_b) + 6k_b - 2p + k_f &= 0 \\ \Rightarrow \cos^2\theta + \cos\theta\left(\frac{p}{2k_b} - 2\right) + 1 - \frac{p}{2k_b} + \frac{k_f}{2k_b} &= 0 \end{aligned}$$

$$\text{which implies} \quad p_{m,N} = \frac{2k_b + \frac{k_f}{2} - 4k_b\cos(\frac{m\pi}{N}) + 2k_b\cos^2(\frac{m\pi}{N})}{1 - \cos(\frac{m\pi}{N})}. \tag{6.38}$$

Figure 6.10 compares the predictions of this expression with numerical results found in the next section. We can see in this figure that, for a typical set of parameters for this mechanical lattice, the solution that bifurcates at the lowest buckling load has neither the highest, nor the lowest spatial wavelength. This is due to the compound nature of this mechanical system; the simpler system with torsional springs only first buckles into the longest wavelength mode, whilst the simpler mechanical system with vertical springs only (Chapter 4) buckles into the lowest spatial wavelength mode first.

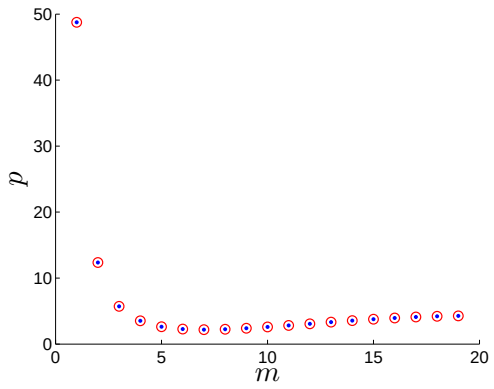

Figure 6.10: *A comparison of the p values at which there are bifurcations from the zero solution computed by Auto (see Section 6.1.2), denoted by circles, and the conjectured p bifurcation values computed using (6.38) (dots). These results are for parameter set ①: $k_b = 1$, $k_f = 1.2$ and $N = 20$.*

The behaviour of this more complex system is determined by the ratio of these two competing effects which is in turn determined by the values of k_b and k_f.

6.3.3 Numerical evidence

Here we present numerical results that confirm that the expression (6.38), derived in the previous section, does indeed give the load values at which there are bifurcations from the flat equilibrium state of the mechanical lattice of Figure 6.1. To do this Auto has been used (see Section 6.1.2 for details) to compute the p values for the bifurcations from the zero equilibrium up to $p = 50$ with an accuracy of 10^{-7} and a resolution of 5×10^{-5} (i.e. this is the minimum bifurcation point separation in p that the code is able to distinguish). These are then compared with the bifurcation values computed using equation (6.38) above.

We can see in Figure 6.10 that, for parameter set ① below, expression (6.38) predicts all the bifurcation points up to $p = 50$. The agreement between the numerical results and expression (6.38) for parameter sets ② and ③ is equally as good (see the table below) and so these results have not been plotted. The parameter sets in the following table have been chosen to give a reasonable selection of parameter values whilst trying to avoid potential special cases in the parameters.

①	$k_b = 1$	$k_f = 1.2$	$N = 20$
②	$k_b = 1$	$k_f = 8.2$	$N = 13$
③	$k_b = 1$	$k_f = 20.2$	$N = 8$

For each of these parameter sets the following values have been computed.

$\max |p_m^* - p_{m,N}|$**:** Here p_m^* is the Auto computed bifurcation load closest to $p_{m,N}$, the expression for which is given above (6.38).

$\max_{m \in H} |\det(\mathrm{d}g/\mathrm{d}x)|$**:** This expression checks the validity of the above discrete BVP formulation of the bifurcations from the zero solution. The maximum is computed over a subset of all the bifurcations because numerically computing Φ^N is challenging when Φ has large modulus real eigenvalues as these cause numerical errors to be greatly exaggerated. The set H is chosen using the fact that since $\det(\Phi) = 1$ we must have $\det(\Phi^N) = 0$. Thus the set H is given by $H = \{m : |\det(\Phi_m^N) - 1| < 10^{-3}\}$ where $\det(\Phi_m^N)$ is the numerically computed value of this quantity for the p value $p = p_{m,N}$.

The result of these computations are summarised in the following table. These numeri-

Parameter set	$\max_m \lvert p_m^* - p_{m,N} \rvert$	$\max_{m \in H} \lvert \det(\mathrm{d}g/\mathrm{d}x) \rvert$
①	1.8×10^{-8}	7.9×10^{-13}
②	5.8×10^{-8}	4.4×10^{-8}
③	3.3×10^{-9}	3.1×10^{-6}

cal results, computed for three points in parameter space, add weight to the conjecture that equation (6.38) gives the p values for all of the bifurcations from the extended, flat equilibrium for the fourth order mechanical system of Figure (6.1).

6.3.4 Eigenvalue behaviour

In this section we understand the buckling behaviour determined in the previous section in terms of the behaviour of the eigenvalues of the linear map Φ, equation (6.35). This points the way to the type of iterated map bifurcations that we can expect in fully nonlinear the discrete BVPs discussed in Section (6.3). It also allows us to derive values regions in k_f and k_b parameter space where the linear buckling behaviour of this compound mechanical system (Figure 6.1) becomes like that of the simpler mechanical systems previously studied.

In Section 6.1, earlier in this chapter, we saw that the parameters k_f and k_b are not independent free parameters. In fact there are two different nondimensionalisations of the physical system that are given by $k_b = 1$ and $k_f \in \mathbb{R}^+$, or $k_f = 1$ and $k_b \in \mathbb{R}^+$. Figure 6.12 shows these two slices though parameter space and the behaviour of the

eigenvalues of Φ in these parameter planes. This figure shows the curves on which there are repeated eigenvalues (solid lines) or where the eigenvalues have zero real part (dotted lines). Schematic representations of the eigenvalue locations in the complex plane for the the regions ⓐ-ⓘ are given in Figure 6.11. The mathematical definitions of these regions and their derivations are given in the appendix to this chapter, Section 6.6.

From these figures we can see that all possible eigenvalue behaviour can be seen in this system. However, we are primarily interested in the paths in parameter space that correspond to the physical system buckling under increasing load. These paths are paths in the plots of Figure 6.12 that move at constant k_f or k_b towards higher values of the load p.

We found in Section 6.3.3 above that the mechanical system buckles, as the load p is increased, as the eigenvalues of Φ move around the unit circle and pass through the roots of unity, $z_{m,N} = \exp \pi m/N$ for $m = 1, \ldots, N-1$. By considering the left pane of Figure 6.12 we can see that when $p = 0$ the eigenvalues of Φ come in two complex conjugate pairs. As p increases, eventually, as long as $k_f < 16k_b$, the eigenvalues hit the unit circle in the complex plane. For $k_f \ll 16k_b$ this collision with the unit circle happens close to $\lambda = 1$ and the first root of unity reached is $z_{1,m}$ and lowest load bifurcation is into the solution with the longest spatial wavelength. However, for $k_f < 16k_b$ with $k_f \approx k_b$ the first root of unity reached will be close to $z_{N-1,N}$ and the lowest load buckling bifurcation will be into a solution with a very short spatial wavelength. For $k_f > 16k_b$, as the load p is increased, the eigenvalues move onto the negative real axis before they hit the unit circle, and so in this parameter region we can expect the behaviour to be almost exactly as that determined in Chapter 4. In this case the lowest load bifurcation is into the solution with the shortest spatial wavelength for any value of N.

6.4 Localisation

For the final section of this chapter we look at some of the behaviour of the fourth order mechanical system of Figure 6.1 for intermediate parameter values away from the two limits already mentioned in sections 6.2.1 and 6.2.2. As we have seen, the behaviour of the two, simpler, limits of this system is complicated and becomes more so as the links are able to rotate through angles of greater than $\pi/2$. Therefore, this section takes a physically motivated view of the, undoubtedly, very complex behaviour for intermediate parameter values. It has been recently suggested (Hunt et al. (2009),

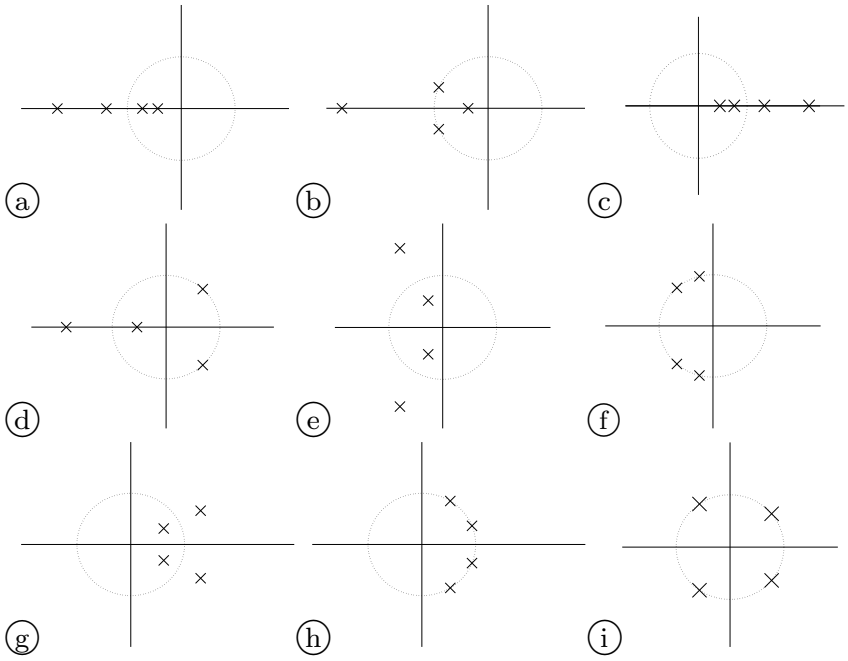

Figure 6.11: *This shows the quadrant, and position relative to the unit circle in the complex plane, of the eigenvalues in regions ⓐ-ⓘ of the plots in Figure (6.12).*

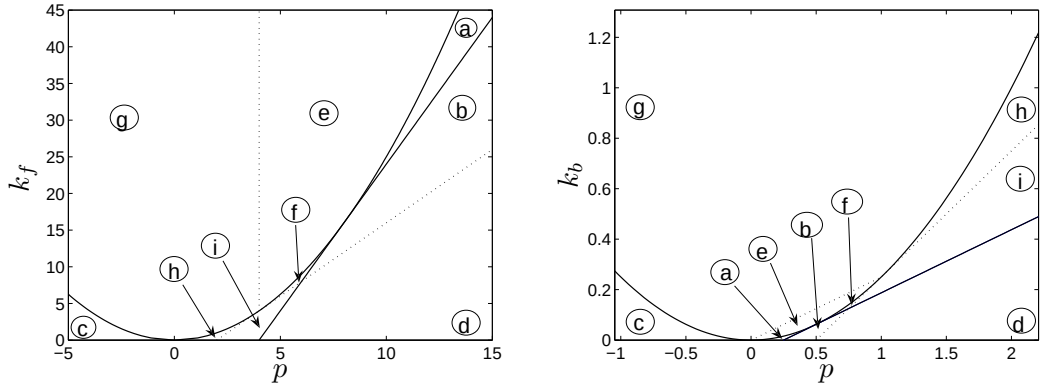

Figure 6.12: *These show the behaviour of the eigenvalues of* Φ *(6.35) as we vary* p *and* k_f *at* $k_b = 1$ *(left plot) and varying* p *and* k_b *at* $k_f = 1$ *(right plot). Figure 6.11 shows where the eigenvalues lie in the complex plane relative to the unit circle for the regions ⓐ-ⓘ.*

Tordesillas & Muthuswamy (2009)) that fourth order lattice models, similar to the one studied here, model important buckling behaviour in the force chains of granular media. The load is applied and eventually the system 'buckles' and then moves into a localised state, for instance a kink-band. In these situations the equilibrium solutions that are of interest are often the solutions that sit nearest the origin when you plot the solutions load against its end shortening (as discussed in Section 4.2.2 of Chapter 4). Thus we present here some numerical results on this system showing the behaviour of the solutions on the primary branches that bifurcate at the lowest loads from the zero equilibrium. These results will also appear in Hunt et al. (2009).

The top left pane of Figure 6.13 shows the bifurcations from the lowest load primary branch in the compound mechanical lattice of this chapter with $N = 101$, $k_b = 1$ and $k_f = 0.2$. The solutions labelled ①–④ and ⓐ–ⓔ show examples of the solutions on the branches at the points marked in the bifurcation diagram. The relatively low value of k_f causes the lowest load bifurcation to be into a linear mode ① with a fairly low spatial wavelength. This low value of k_f also allows the system to do work into the foundation and we see on the secondary branches that, as p nears zero, the vertical displacement of each solution localises at one or more points in the lattice. We can also see that this lattice is selecting a localisation length that is neither that of the whole lattice, nor the individual link and appears to be close to that of the original sinusoidal buckle pattern. This could be a potentially important localisation length selection mechanism in physical systems, such as granular media.

Figure 6.14 shows the behaviour of the three lowest load primary branches for $N = 101$, $k_b = 1$ and $k_f = 4.0$ (①–③). This value of k_f is relatively high, causing the solutions on the primary branches to localise fairly quickly and reduce the work done into the foundation. As the load reaches zero, on branches ② and ③ some interesting behaviour is observed which is shown in more detail for branch ② in the bottom two panes of Figure 6.14. The solutions along this branch consist of a flat central section three 'layers' thick where the mechanical system overlaps itself. There are then two regions of high curvature that resolves this situation before the lattice reaches the end supports. This is shown in ⓒ and ⓓ of Figure 6.14 where the solutions are plotted in the physical space (X_i, Y_i), where X_i and Y_i are given in terms of $\boldsymbol{\theta}$ in equation (6.15). Here, as the end shortening increases the load required to support this solution oscillates between two values as extra links join the inverted central section of the lattice. This is a discrete example of homoclinic snaking seen in some continuum strut models (Hunt et al. (2000)).

These results demonstrate some of the unique and interesting behaviour exhibited by

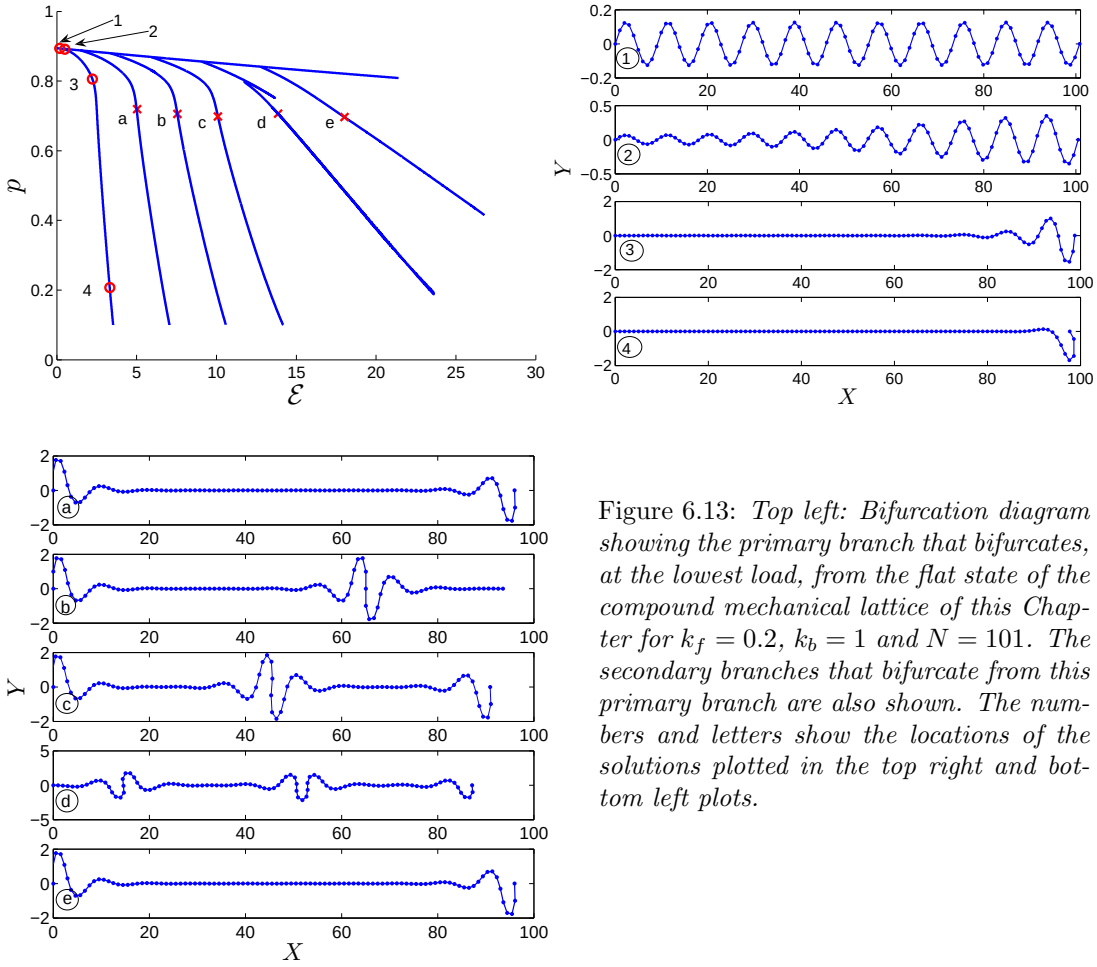

Figure 6.13: *Top left: Bifurcation diagram showing the primary branch that bifurcates, at the lowest load, from the flat state of the compound mechanical lattice of this Chapter for* $k_f = 0.2$, $k_b = 1$ *and* $N = 101$. *The secondary branches that bifurcate from this primary branch are also shown. The numbers and letters show the locations of the solutions plotted in the top right and bottom left plots.*

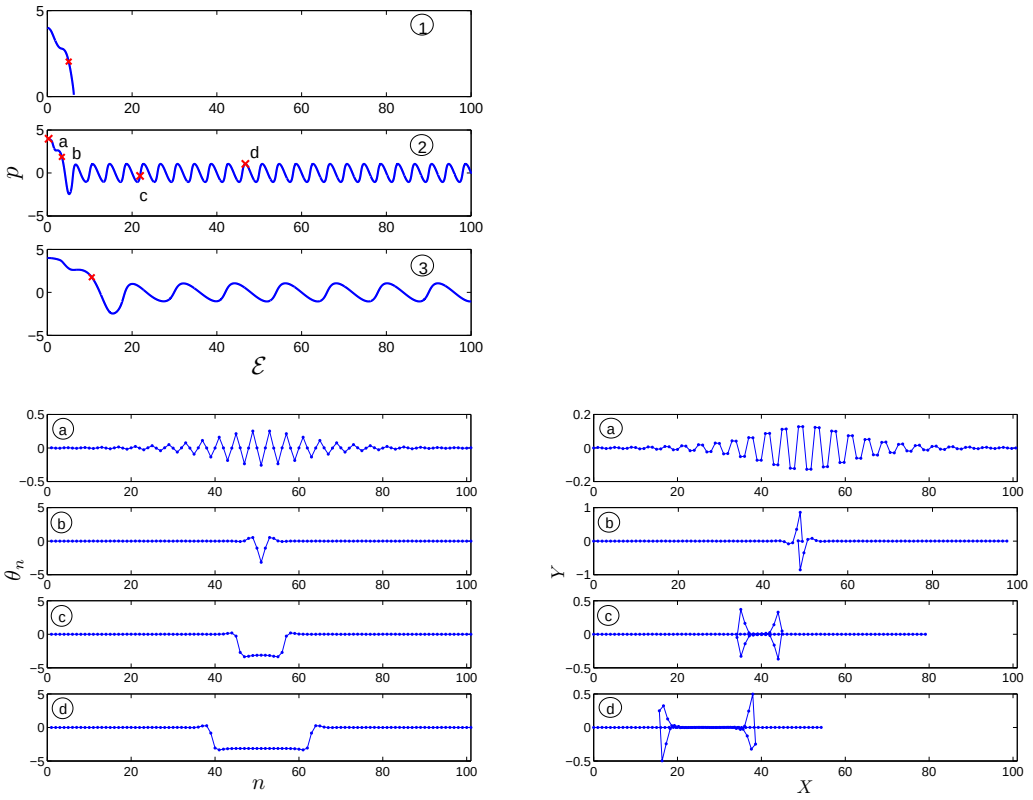

Figure 6.14: *Top left: Load end-shortening plots for the solution branches that are created in the three lowest load bifurcations from the flat equilibrium state of the compound mechanical lattice of this Chapter, for* $K_f = 4$, $k_b = 1$ *and* $N = 101$. *Plots* ⓐ–ⓓ *show examples of the solutions on branch* ②. *The bottom left plots shows* θ_n *as a function of* n, *whilst the bottom right plots show the physical shape of the lattice, with* X_n *and* Y_n *calculated from* $\boldsymbol{\theta}$ *using equations (6.15).*

the fourth order mechanical lattice model of this chapter, and have already helped motivate further work into the link between fourth-order mechanical lattice models and force chain buckling in granular media, Tordesillas et al. (2009).

6.5 Summary

In this chapter the new mechanical lattice shown in Figure 6.1 has been introduced and then studied. This lattice is a combination of two previously studied mechanical lattices; one, with vertical springs only, was studied in detail in Chapter 4 and the other, with torsional springs only, was studied in detail by Domokos & Holmes (1993). In Section 6.1 we saw how, under the assumption that the link rotations, θ_n, satisfy $|\theta_n| < \pi/2$ for all n the static equilibrium states of this mechanical system can be described by a nonlinear fourth order difference equation. This restriction was then lifted to derive another set of equations that model the fully nonlinear behaviour of this lattice. In sections 6.2.1 and 6.2.2 we then saw how the behaviour of two simpler mechanical lattices is seen in this compound lattice in the parameter limits $k_f = 0$ and $k_b = 0$. It was also seen that the more general mathematical model derived in Section 6.1 permitted additional mechanical equilibrium states that were not seen in the previous studies on the simpler systems, and the behaviour of these additional equilibria was studied.

In Chapter 4 and the work of Domokos & Holmes (1993) it is shown how useful describing the static equilibrium states of a mechanical system by the solutions to a discrete boundary value problem can be. In Section 6.3 two potential methods for describing the static equilibrium states of the compound mechanical lattice of Figure 6.1 in terms of a discrete boundary value problem based on a map $\Phi : \mathbb{R}^4 \to \mathbb{R}^4$ (rather than a map from $\mathbb{R}^2$ to $\mathbb{R}^2$ as with the two simpler mechanical lattices) were discussed. These two methods both had their disadvantages and so further study on the fully nonlinear case was left to further work. However, studying the linear behaviour of this mechanical lattice using a discrete BVP is more straightforward and this was done in Section 6.3.1. The work of this section conjectured, with supporting numerical evidence, that there are primary bifurcations from the flat equilibrium state of this mechanical lattice at the load values

$$p_{m,N} = \frac{2k_b + \frac{k_f}{2} - 4k_b\cos(\frac{m\pi}{N}) + 2k_b\cos^2(\frac{m\pi}{N})}{1 - \cos(\frac{m\pi}{N})}$$

for $m = 1, \ldots, N-1$. Further properties of the linear discrete boundary value problem were discussed in the following sections.

Finally, some numerical results demonstrating some interesting behaviour in the fully nonlinear lattice equations derived in Section 6.1 were presented in Section 6.4. We saw that on the primary branches that bifurcate from the flat states at the lowest loads the solutions localise for lower and higher values of the foundation stiffness k_f. For lower values of k_f this displacement localisation presented its self at several points in the lattice as seen in Figure 6.13. For higher values of k_f interesting snaking behaviour was observed as the load oscillates between two distinct values and the localised response grows in width as the end shortening of the lattice increases. This work has raised interesting questions for the behaviour of force chain buckling in granular media which is being investigated further (Tordesillas et al. (2009)).

6.6 Appendix: Eigenvalue results and derivations

In this section we present and prove the results summarised in figures 6.11 and 6.12, on the eigenvalues of the linear map Φ, equation (6.35). We divide up the p, k_b and k_f parameter space into regions which are shown in Figure 6.12. These regions are separated by curves (or surfaces) on which there are repeated eigenvalues or where one or more eigenvalues has zero real part. The regions are denoted by a circled letter, e.g. ⓐ, and the boundary between two regions, for instance regions ⓐ and ⓑ, is denoted by ⓐ|ⓑ. We consider two ranges for p; first we consider $p^2 \leq 4k_fk_b$ and then $p^2 > 4k_fk_b$. The following tables summarise the behaviour of the eigenvalues which is then proved.

	Parameter region			Eigenvalue relations	Region/Boundary
i)	$p^2 < 4k_fk_b$	&	$p = 4k_b$	$\mathrm{Re}(\lambda_i) = 0$ for $i = 1, 2, 3, 4$	ⓖ|ⓔ
ii)	$p^2 = 4k_fk_b$	&	$k_f < 16k_b$	$\lambda_1 = \lambda_3 = \lambda_2^* = \lambda_4^*$	ⓖ|ⓗ & ⓔ|ⓕ
			$k_f = 16k_b$	$\lambda_i = -1$ for $i = 1, 2, 3, 4$	
			$k_f > 16k_b$	$\mathrm{Im}(\lambda_i) = 0\ \forall\ i$, $\lambda_1 = \lambda_3$,	
				$\lambda_2 = \lambda_4$ and $\lambda_1^2 = 1/\lambda_2^2$	ⓔ|ⓐ

Before we summarise the behaviour for $p^2 > 4k_fk_b$ we define the following functions:

$$\alpha_+(k_f, k_b) = \begin{cases} 4k_b + k_f/4 & : \quad k_f \geq 16k_b \\ 2\sqrt{k_fk_b} & : \quad k_f < 16k_b \end{cases} \qquad \beta_+(k_f, k_b) = \begin{cases} 2k_b + k_f/2 & : \quad k_f \geq 4k_b \\ 2\sqrt{k_fk_b} & : \quad k_f < 4k_b \end{cases}$$

$$\alpha_-(k_f, k_b) = \begin{cases} 2\sqrt{k_fk_b} & : \quad k_f \geq 16k_b \\ 4k_b + k_f/4 & : \quad k_f < 16k_b \end{cases} \qquad \beta_-(k_f, k_b) = \begin{cases} 2\sqrt{k_fk_b} & : \quad k_f \geq 4k_b \\ 2k_b + k_f/2 & : \quad k_f < 4k_b. \end{cases}$$

To help visualise these functions and the behaviour described below Figure 6.15 shows the curves $p = \alpha_\pm(k_f, k_b)$ and $p = \beta_\pm(k_f, k_b)$ in the $k_f = 1$ and $k_b = 1$ parameter planes. These parameter planes are the same as those shown in Figure 6.12 of Section 6.3.4.

The following table summarises the behaviour for $p^2 > 4k_fk_b$ with $p > 0$ which is summarised graphically in Figure 6.12.

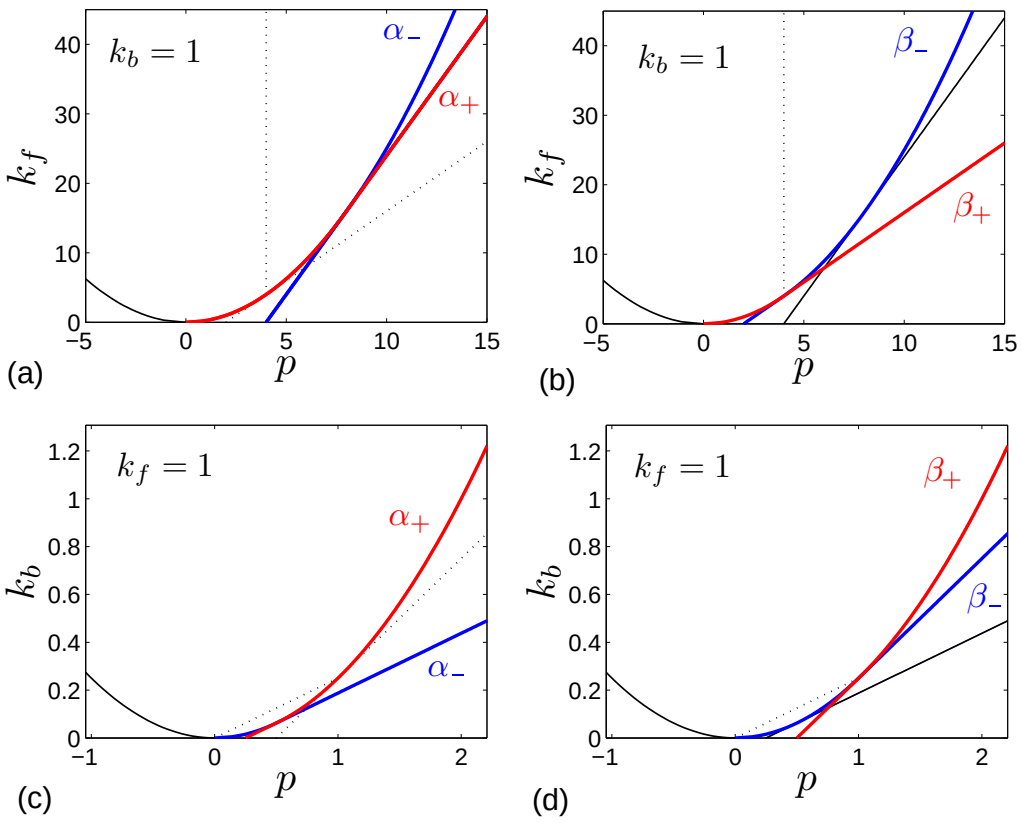

Figure 6.15: *Plots of the functions* $p = \alpha_\pm(k_f, k_b)$ *and* $p = \beta_\pm(k_f, k_b)$ *in the* $k_f = 1$ *and* $k_b = 1$ *parameter planes. Specifically: (a)* $p = \alpha_-(k_f, 1)$ *(blue) and* $p = \alpha_+(k_f, 1)$ *(red); (b)* $p = \beta_-(k_f, 1)$ *(blue) and* $p = \beta_+(k_f, 1)$ *(red); (c)* $p = \alpha_-(1, k_b)$ *(blue) and* $p = \alpha_+(1, k_b)$ *(red); (d)* $p = \beta_-(1, k_b)$ *(blue) and* $p = \beta_+(1, k_b)$ *(red).*

	p	k_f, k_b	Eigenvalue relations	Region/Boundary
(iii)	$\beta_+ < p < \beta_-$	$k_f < 4k_b$	$\lvert\lambda_{1,2}\rvert = 1$, $\mathrm{Re}(\lambda_{1,2}) > 0$	ⓗ
	$p = \beta_-$	$k_f < 4k_b$	$\lvert\lambda_{1,2}\rvert = 1$, $\mathrm{Re}(\lambda_{1,2}) = 0$	ⓗ|ⓘ
	$\beta_- < p < \alpha_-$	$k_f < 16k_b$	$\lvert\lambda_{1,2}\rvert = 1$, $\mathrm{Re}(\lambda_{1,2}) < 0$	ⓘ & ⓕ
	$p > \alpha_-$	$k_f > 0$ $k_b > 0$	$\mathrm{Im}(\lambda_{1,2}) = 0$	ⓐ & ⓑ & ⓓ
(iv)	$p > \beta_+$	$k_f > 0$ $k_b > 0$	$\lvert\lambda_{3,4}\rvert = 1$, $\mathrm{Re}(\lambda_{3,4}) > 0$	ⓗ & ⓘ & ⓓ
	$p = \beta^+$	$k_f > 4k_b$	$\lvert\lambda_{3,4}\rvert = 1$, $\mathrm{Re}(\lambda_{3,4}) = 0$	ⓕ|ⓘ & ⓑ|ⓓ
	$\alpha_+ < p < \beta_+$	$k_f > 4k_b$	$\lvert\lambda_{3,4}\rvert = 1$, $\mathrm{Re}(\lambda_{3,4}) < 0$	ⓕ & ⓑ
	$\alpha_- < p < \alpha_+$	$k_f > 16k_b$	$\mathrm{Im}(\lambda_{3,4}) = 0$	ⓐ

We now move on to the derivation of the above results. These results are derived from expressions generated by the computer algebra package Maple for the eigenvalues of Φ. If we define the following functions

$$a(p, k_b, k_f) = p^2 - 4k_bk_f, \quad b(p, k_b, k_f) = p^2 - 4k_bp - 2k_bk_f, \quad c(p, k_b) = 4k_b - p$$

these eigenvalues can be written

$$\lambda_1 = \frac{1}{4k_b}\left(c + \sqrt{a} + \sqrt{2}\sqrt{b + c\sqrt{a}}\right) \tag{6.39}$$

$$\lambda_2 = \frac{1}{4k_b}\left(c + \sqrt{a} - \sqrt{2}\sqrt{b + c\sqrt{a}}\right) \tag{6.40}$$

$$\lambda_3 = \frac{1}{4k_b}\left(c - \sqrt{a} + \sqrt{2}\sqrt{b + c\sqrt{a}}\right) \tag{6.41}$$

$$\lambda_4 = \frac{1}{4k_b}\left(c - \sqrt{a} - \sqrt{2}\sqrt{b + c\sqrt{a}}\right). \tag{6.42}$$

It is first useful to note some properties of the functions a, b and c. The surfaces in (p, k_f, k_b) parameter space on which $b(p, k_f, k_b) = 0$ and $a(p, k_f, k_b) = 0$ are shown in Figure 6.16 and the intersections of these surfaces with the parameter planes $k_f = 1$ and $k_b = 1$ are shown in Figure 6.17. The next lemma gives the lines in parameter space on which both $a = 0$ and $b = 0$.

Lemma 6.4. *$a(p, k_f, k_b) = 0$ and $b(p, k_f, k_b) = 0$ on the following three lines in pa-*

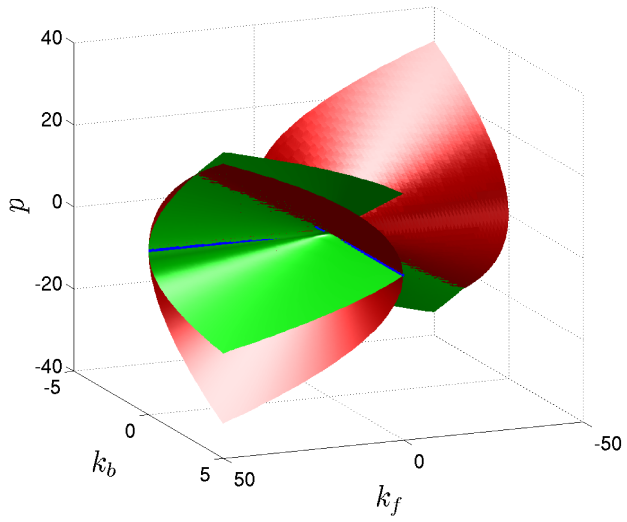

Figure 6.16: *Surfaces in parameter space on which the functions* $a(p, k_f, k_b)$ *(red) and* $b(p, k_f, k_b)$ *(green) equal zero. The blue lines show the intersections where both* a *and* b *are zero.*

rameter space

$$\begin{aligned} L_1: &\quad p = 0, &\quad k_f = 0, &\quad k_b \in \mathbb{R} \\ L_2: &\quad p = 8k_b, &\quad k_f = 16k_b, &\quad k_b \in \mathbb{R} \\ L_3: &\quad p = 0, &\quad k_b = 0, &\quad k_f \in \mathbb{R} \end{aligned}$$

Proof. We start by considering a thus: $a(p, k_f, k_b) = 0 \Rightarrow p^2/2 = 2k_b k_f$, then this, along with $b(p, k_f, k_b) = 0$, implies $p(p - 8k_b) = 0$ we now have two cases

Case 1:

$$p = 0 \text{ and } a = 0 \Rightarrow \begin{cases} k_f = 0,\ k_b \in \mathbb{R}, & (L_1) \text{ or} \\ k_b = 0,\ k_f \in \mathbb{R} & (L_3) \end{cases}$$

Case 2:

$$p = 8k_b \text{ and } a = 0 \quad \Rightarrow \quad k_f = 16k_b,\ k_b \in \mathbb{R}, \quad (L_2).$$

□

The next lemma gives some further results that will be required when deriving the regions in parameter space on which we have repeated eigenvalues.

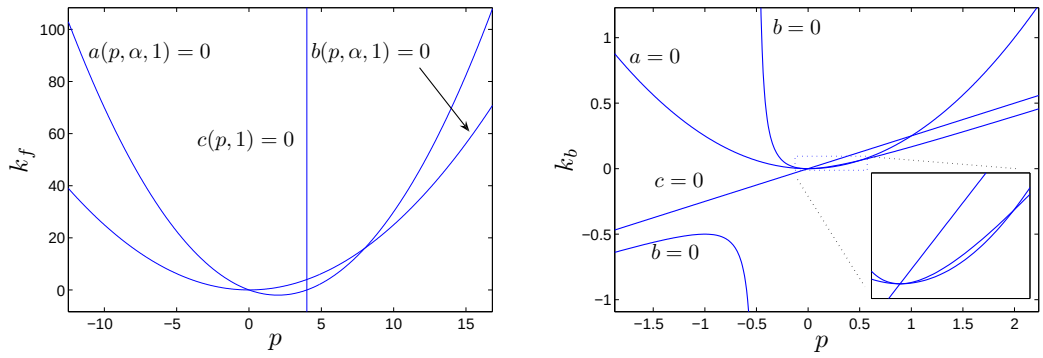

Figure 6.17: *Curves on which the functions $a(p,k_f,k_b)$, $b(p,k_f,k_b)$ and $c(p,k_b)$ zero. For $k_b=1$, left and $k_f=1$, right.*

Lemma 6.5. *Assume $a(p,k_f,k_b)>0$, then the following statements hold.*

$$\begin{aligned} \textit{i) If } p=4k_b+\frac{k_f}{4} \textit{ and } k_f<16k_b \textit{ then } (b-c\sqrt{a})(p,k_f,k_b) &= 0 \textit{ and if} \\ k_f>16k_b \textit{ then } (b+c\sqrt{a})(p,k_f,k_b) &= 0. \end{aligned}$$

$$\begin{aligned} \textit{ii) If } p=2k_b+\frac{k_f}{2} \textit{ and } k_f<4k_b \textit{ then } (c-\sqrt{a})(p,k_f,k_b) &= 0 \textit{ and if} \\ k_f>4k_b \textit{ then } (c+\sqrt{a})(p,k_f,k_b) &= 0. \end{aligned}$$

Proof. Substituting the p value from i) above into $b-c\sqrt{a}$ gives

$$\begin{aligned} (b\pm c\sqrt{a})(p,k_f,k_b) &= p^3-2k_bk_f-4k_bp\pm(4k_b-p)\sqrt{p^2-4k_bk_f} \\ &= \left(4k_b+\frac{k_f}{4}\right)^2-4k_b\left(4k_b+\frac{k_f}{4}-2k_bk_f\right) \\ &\qquad \pm\left(4k_b-4k_b-\frac{k_f}{4}\right)\sqrt{\left(4k_b+\frac{k_f}{4}\right)^2-4k_bk_f} \\ &= \frac{-k_f}{4}\left(\left(4k_b-\frac{k_f}{4}\right)\pm\sqrt{\left(4k_b-\frac{k_f}{4}\right)^2}\right). \end{aligned}$$

From this we see $k_f<16k_b$ implies $4k_b-k_f/4>0$ and $(b-c\sqrt{a})(p,k_f,k_b)=0$ and

$k_f > 16k_b$ implies $4k_b - k_f/4 < 0$ and $(b + c\sqrt{a})(p, k_f, k_b) = 0$. Similarly for ii) we have

$$\begin{aligned}(c \pm \sqrt{a})(p, k_f, k_b) &= 4k_b - \left(2k_b - \frac{k_f}{2}\right) \pm \sqrt{\left(2k_b - \frac{k_f}{2}\right)^2 - 4k_b k_f} \\ &= 2k_b - \frac{k_f}{2} \pm \sqrt{\left(2k_b - \frac{k_f}{2}\right)^2}.\end{aligned}$$

From this we see that $k_f < 4k_b$ implies $2k_b - k_f/2 > 0$ and $(c - \sqrt{a})(p, k_f, k_b) = 0$ and $k_f > 4k_b$ implies $2k_b - k_f/2 < 0$ and $(c + \sqrt{a})(p, k_f, k_b) = 0$. □

Using lemmas 6.4 and 6.5 and the eigenvalue expressions (6.39)–(6.42) we now derive the eigenvalue relations presented in Section 6.3.4.

(i): For $p^2 \leq 4k_f k_b$ $a(p, k_f, k_b) \leq 0$ and so $\sqrt{a(p, k_f, k_b)}$ is purely imaginary or zero. If $p = 4k_b$ then $c(p, k_b) = 0$ and since $b(4k_b, k_f, k_b) = -2k_f k_b$ is always negative from (6.39)-(6.42) we can see that $\mathrm{Re}(\lambda_i) = 0$ for $i = 1, 2, 3, 4$.

(ii): Now consider $p^2 = 4k_f k_b$. Substituting $p = \pm 2\sqrt{k_f k_b}$ into equations (6.39)-(6.42) and noting that when $p^2 = 4k_f k_b$ $a(p, k_f, kj_b) = 0$ gives

$$\lambda_1 = \lambda_3 = \frac{1}{4k_b}\left(c\left(\pm 2\sqrt{k_f k_b}, k_b\right) + \sqrt{2}\sqrt{b\left(\pm 2\sqrt{k_f k_b}, k_f, k_b\right)}\right)$$
$$\lambda_2 = \lambda_4 = \frac{1}{4k_b}\left(c\left(\pm 2\sqrt{k_f k_b}, k_b\right) - \sqrt{2}\sqrt{b\left(\pm 2\sqrt{k_f k_b}, k_f, k_b\right)}\right)$$

We can see from these expressions that the behaviour of these eigenvalues depends on the value of $b(\pm\sqrt{k_f k_b}, k_f, k_b)$.
For $b(\pm 2\sqrt{k_f k_b}, k_f, k_b) < 0$ we have $\lambda_{1,3} = \lambda^*_{2,4}$, and for $b(\pm 2\sqrt{k_f k_b}, k_f, k_b) = 0$ we have $\lambda_1 = \lambda_2 = \lambda_3 = \lambda_4$.
For $b(\pm 2\sqrt{k_f k_b}, k_f, k_b) > 0$ we have two repeated real eigenvalues with $\lambda_{1,3} = 1/\lambda_{2,3}$.

(iii) & (iv): In these cases we have $p^2 > 4k_f k_b$ and so $\sqrt{a(p, k_f, k_b)}$ is real and greater then zero. Thus when $b + c\sqrt{a} = 0$ we have $\lambda_1 = \lambda_2$ and when $b - c\sqrt{a} = 0$ we have $\lambda_3 = \lambda_4$. When $b - c\sqrt{a} < 0$ the real parts of λ_1 and λ_2 are given by $(c + \sqrt{a})/(2k_b)$ and so are zero when $c + \sqrt{a} = 0$. Similarly for $b + c\sqrt{a} < 0$ $\mathrm{Re}(\lambda_{2,4}) = 0$ when $c - \sqrt{a} = 0$. This, along with the results of lemma 6.5, gives the results of Section 6.3.4.

Chapter 7

Summary and conclusions

This thesis has contributed to the understanding of mechanical lattices, such as those in Figure 7.1 below, and to the understanding of how to model such mechanical lattices using discrete boundary value problems. Chapter 3 presented a method for modelling the static equilibrium states of a general lattice, where the potential energy can be written in the form

$$V(Q_0, \ldots, Q_N) = h \sum_{n=0}^{N} v(Q_n) + h \sum_{n=0}^{N-1} w\left(\frac{Q_{n+1} - Q_n}{h}\right)$$

(expression (3.1)), using a discrete boundary value problem. This method used ideas from discrete mechanics (Marsden & West (2001)) to derive discrete boundary value problems that model the lattice with either free or fixed coordinates at each end of the lattice.

Chapter 4 then applied the general results from Chapter 3 to the specific mechanical lattice shown in (b) of Figure 7.1. This lead to a detailed study of the multitude of static equilibrium states that exist in this mechanical lattice. This study was partly motivated by the many static equilibrium states found in mechanical lattice (a) of Figure 7.1 by Domokos & Holmes (1993), and because of this we now present a brief comparison between the behaviour of these two mechanical lattices.

Figures 7.2 and 7.3 show examples of the bifurcation diagrams for the static equilibrium states of mechanical lattices (a) and (b) of Figure 7.1 with six links ($N = 6$). Perhaps the most significant physical difference between these two systems is the point noted by Thompson & Hunt (1973): that the post-buckling stiffness of the two systems has different signs. In figure 7.2 we can see that, after the initial buckling from the zero

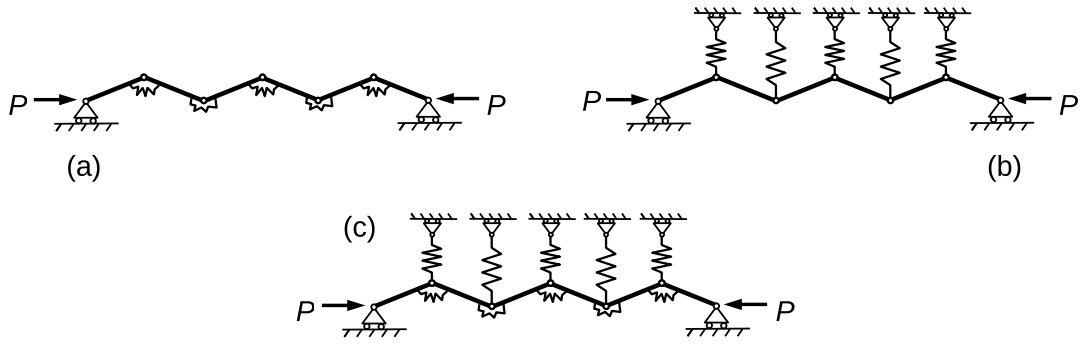

Figure 7.1: *Mechanical lattices (b) and (c) are the subjects of this thesis, (a) has been previously studied in detail by Domokos & Holmes (1993). This figure reproduces Figure 1.1 of the introduction.*

equilibrium, the load on all of the branches of primary equilibria increases with increasing end-shortening indicating a positive post-buckling stiffness, whereas, in Figure 7.3 the opposite is the case, and the load the solutions can support falls with increasing end-shortening. The work of Chapter 4 shows that this negative post-buckling stiffness persists throughout the whole bifurcation diagram of the static equilibrium states of lattice (b) (Figure 7.3).

Another interesting difference between the static equilibrium state bifurcation diagrams for lattices (a) and (b) is that for $N = 6$ lattice (a) appears to have a much larger explosion of equilibrium states, as the end-shortening increases, than lattice (b). This can be understood by considering the behaviour of the iterated map underlying the behaviour of the discrete BVP that models the equilibrium states of these systems. The explosion of static equilibrium states is caused, largely, by homoclinic tangling about one or more hyperbolic fixed points in the relevant iterated map (Domokos & Holmes (1993), Hunt et al. (1997)). The map of lattice (a) has two fixed points, one that is hyperbolic for all p and one that is hyperbolic for $p > 4$. This leads to the possibility of two homoclinic tangles and a greater number of static equilibrium states than lattice (b), which has only one fixed point that is hyperbolic for $p < 1$.

We saw in Section 6.2.2 of Chapter 6 that removing the link angle restriction $|\theta_n| < \pi/2$ for all n on the lattice (b) of Figure 7.1 greatly increases the number of static equilibrium states in this mechanical lattice. This leads to a more physical interpretation to the difference in the number of static equilibrium states between mechanical lattices (a) and (b): it is the fact that the links in each mechanical system are able to overlap, allowing link angles of greater than $\pi/2$, that helps to cause the huge explosion in static equilibrium states seen in lattice (a). The red circles in Figure 7.2 show the few

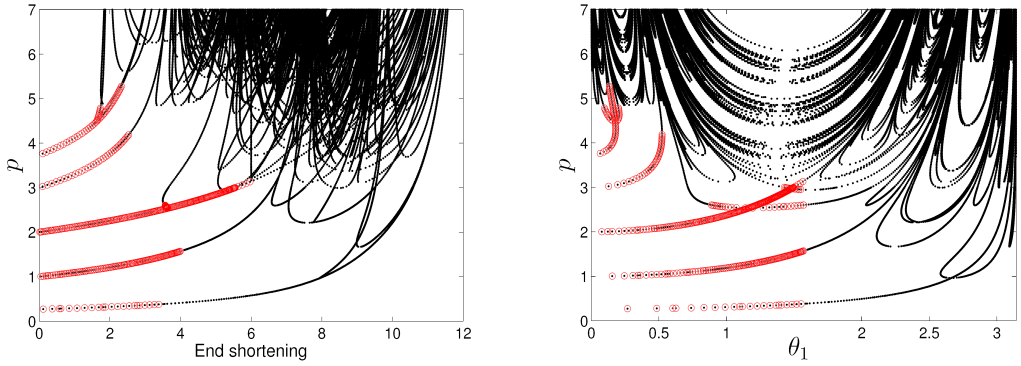

Figure 7.2: *This shows the bifurcation diagrams for system (b) of Figure 7.1 with torsional springs only and six links ($N = 6$). On the left we see how the non-dimensional load varies with the overall end-shortening of the system, whilst the right plot shows how the solutions, uniquely represented by the nondimensional load p and the angle of link one, bifurcate. The red circles show the solutions that satisfy $|\theta_n| < \pi/2$ for all n. This system was studied in detail in Domokos & Holmes (1993).*

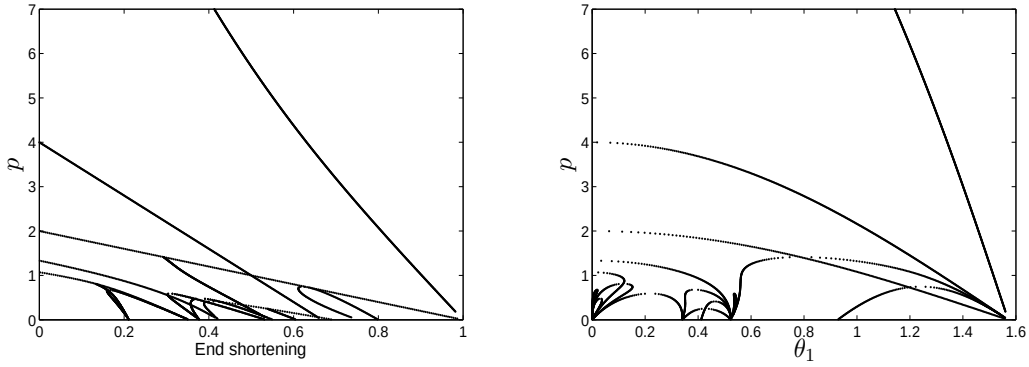

Figure 7.3: *This shows the bifurcation diagrams for the vertical springs only limit of the mechanical system of Figure with six links ($N = 6$). These are found and analysed in Chapter 4.*

solutions in lattice (a) that satisfy $|\theta_n| < \pi/2$ for all n.

Chapter 6 considered the more complex mechanical system that results from using both the vertical springs seen in lattice (b) and the torsional springs of lattice (a). This is the mechanical system shown in (c) of Figure 7.1. The combination of these two spring types causes the complexity of the system to increase dramatically. Firstly, the map underlying any discrete BVP that models the static equilibrium states of this system is now not a map from $\mathbb{R}^2$ to $\mathbb{R}^2$, but a map from $\mathbb{R}^4$ to $\mathbb{R}^4$ increasing the complexity of behaviour and difficulty of analysis. Also, in this system the primary branch that buckles at the lowest load is now no longer the branch with the longest spatial wavelength (as with lattice (a)) or the shortest wavelength (as with lattice (b)) but an intermediate wavelength. In Section 6.4 we sew that this may be the selection method for the localisation length scale of the lattice when it eventually localises.

Chapter 5 demonstrated, numerically, the existence of linearly stable time periodic spatially localised, discrete breather, solutions in the nonlinear time evolution equations for mechanical lattice (b). This is believed to be the first observation of discrete breathers in a mechanical lattice system. Also found were solutions called phonobreathers (Marin & Aubry (1996), Morgante et al. (2002)) which appear to be a breather solution superimposed on a background that sinusoidally oscillates both spatially and temporally. Although this solution was found to be linearly unstable, the nonlinear dynamics close to the exact phonobreather trajectory was interesting. This consisted of a slowly growing core of apparently spatially disordered oscillation which slowly envelops the sinusoidal tails.

Bibliography

Abramowitz, M. & Stegun, I. A. (1964), *Handbook of Mathematical Functions with Formulas, Graphs, and Mathematical Tables*, Dover, New York. Ninth Dover printing, tenth GPO printing.

Allgower, E. L. (1975), On a discretization of $y'' + ay^k = 0$, *in* J. H. Miller, ed., 'Topics in Numerical Analysis 2', Vol. 2, The Royal Irish Academy, The Royal Irish Academy, Academic Press, New York, pp. 1–15.

Arnold, V. I. (1980), *Mathematical Methods of Classical Mechanics*, Graduate Texts in Mathematics, 2nd edn, Springer-Verlag.

Aubry, S. (1997), 'Breathers in nonlinear lattices: Existence, linear stability and quantization', *Physica D: Nonlinear Phenomena* **103**(1-4), 201–250.

Aubry, S. (2006), 'Discrete breathers: Localization and transfer of energy in discrete Hamiltonian nonlinear systems', *Physica D: Nonlinear Phenomena* **216**(1), 1–30.

Aubry, S., Kopidakis, G. & Kadelburg, V. (2001), 'Variational proof for hard discrete breathers in some classes of Hamiltonian dynamical systems', *Discrete and Continuous Dynamical Systems - Series B* **1**, 271–298.

Benito, R., de León, M. & Martin de Diego, D. (2006), 'Higher-order discrete Lagrangian mechanics', *International Journal of Geometric Methods in Modern Physics* **3**(3), 421–436.

Beyn, W. J. & Lorenz, J. (1982), 'Spurious solutions for discrete superlinear boundary value problems', *Computing* **28**, 43–51.

Brillouin, L. (1946), *Wave Propagation in Periodic Structures*, 2nd edn, Courier Dover Publications.

Carr, J. & Eilbeck, J. C. (1985), 'Stability of stationary solutions of the discrete self-trapping equation', *Physics Letters A* **109**(5), 201–204.

Champneys, A. R. & Toland, J. F. (1993), 'Bifurcation of a plethora of multi-modal homoclinic orbits for autonomous Hamiltonian systems', *Nonlinearity* **6**, 665–722.

Ciocci, M.-C. (2004), Bifurcation of periodic orbits and persistence of quasi periodic orbits in families of reversible systems., PhD thesis, University of Ghent.

Doedel, E. J., Champneys, A. R., Fairgrieve, T. F., Kuznetsov, Y. A., Sandstede, B. & Wang, X. (1997), Auto97: Continuation and bifurcation software for ordinary differential equations (with HomCont). Technical Report, Concordia University.

Domokos, G. & Holmes, P. (1993), 'Euler's problem, Euler's method, and the standard map; or, the discrete charm of buckling', *Journal of Nonlinear Science* **3**, 109–151.

Eilbeck, J. C. & Johansson, M. (2003), The discrete nonlinear schrdinger equation - 20 years on, *in* L. Vazquez, R. S. Mackay & M. P. Zorzano, eds, 'Proceedings of the Third Conference on Localization and Energy Transfer in Nonlinear Systems, June 17th-21st 2002', pp. 44–67.

Eilbeck, J. C., Lomdahl, P. S. & Scott, A. C. (1984), 'Soliton structure in crystalline acetanilide', *Physical Review B* **30**(8), 4703–4712.

Eilbeck, J. C., Lomdahl, P. & Scott, A. (1985), 'The discrete self-trapping equation', *Physica D: Nonlinear Phenomena* **16**(3), 318–338.

Fermi, E., Pasta, J. & Ulam, S. (1955), 'Studies of non linear problems'. Los Alamos Report LA-1940 since published in 'The Collected Papers of Enrico Fermi, Vol II (USA 1939-1954)', University of Chicago Press, 1965, p978.

Feynman, R. P., Leighton, R. B. & Sands, M. (1963), *The Feynman Lectures on Physics*, Vol. II, Addison Wesley.

Flach, S. & Gorbach, A. V. (2008), 'Discrete breathers — Advances in theory and applications', *Physics Reports* **467**, 1116.

Flach, S. & Willis, C. R. (1998), 'Discrete breathers', *Physics Reports* **295**, 181–264.

Hairer, E., Lubich, C. & Wanner, G. (2002), *Geometric Numerical Integration*, Springer Series in Computational Mathematics, Springer.

Holmes, P. & Williams, R. F. (1985), 'Knotted periodic orbits in suspensions of Smale's horseshoe: torus knots and bifurcation sequences', *Archive for Rational Mechanics and Analysis* **90**(2), 115–194.

Hunt, G. W., Bolt, H. M. & Thompson, J. M. (1989), 'Structural localization phenomena and the dynamical phase-space analogy', *Proceedings of the Royal Society of London. A. Mathematical and Physical Sciences* **425**, 245–267.

Hunt, G. W., Lawther, R. & Providencia E Costa, P. (1997), 'Finite element modelling of spatially chaotic structures', *International Journal for Numerical Methods in Engineering* **40**, 2237–2256.

Hunt, G. W., Peletier, M. A., Champneys, A. R., Woods, P. D., Wadee, M. A., Budd, C. J. & Lord, G. . (2000), 'Cellular buckling in long structures', *Nonlinear Dynamics* **21**, 3–29.

Hunt, G. W., Tordesillas, A., Green, S. C. & Shi, J. (2009), Force-chain buckling in granular media: a structural mechanics perspective. To be published in the Philosophical Transactions of the Royal Society A.

Hunt, G. W., Wadee, M. K. & Shiacolas, N. (1993), 'Localized elasticae for the strut on the linear foundation', *Journal of Applied Mechanics* **60**, 1033–1038.

James, G. (2003), 'Centre manifold reduction for quasilinear discrete systems', *Journal of Nonlinear Science* **13**(1), 27–63.

Keller, H. B. (1977), Numerical solution of bifurcation and nonlinear eigenvalue problems, *in* P. H. Rabinowitz, ed., 'Applications of Bifurcation Theory', Proceedings of an Advanced Seminar Conducted by the Mathematics Research Center, University of Wisconsin at Madison, Academic Press, pp. 359–384.

Kocsis, A. & Kaárolyi, G. (2006), 'Conservative spatial chaos of buckled elastic linkages', *Chaos* **16**(3), 033111.

Leimkuhler, B. & Reich, S. (2004), *Simulating Hamiltonian Dynamics*, Vol. 14 of *Cambridge Monographs on Applied and Computational Mathematics*, Cambridge University Press.

MacKay, R. S. & Aubry, S. (1994), 'Proof of existence of breathers for time-reversible or Hamiltonian networks of weakly coupled oscillators', *Nonlinearity* **7**, 1623–1643.

Maddocks, J. H. (1984), 'Stability of nonlinearly elastic rods', *Archive for Rational Mechanics and Analysis* **85**(4), 311–354.

Marin, J. L. & Aubry, S. (1996), 'Breathers in nonlinear lattices: Numerical calculation from the anticontinuous limit', *Nonlinearity* **9**, 1501–1528.

Marsden, J. E. & West, M. (2001), 'Discrete mechanics and variational integrators', *Acta Numerica* **10**(-1), 357–514.

Meyer, K. R. (1970), 'Generic bifurcation of periodic points', *Transactions of the American Mathematical Society* **149**(1), 95–107.

Meyer, K. R. & Hall, G. R. (1992), *Introducion to Hamiltonian Dynamical Systems and the N-Body Problem*, Springer-Verlag.

Mingaleev, S. F., Gaididei, Y. B., Christiansen, P. L. & Kivshar, Y. S. (2002), 'Nonlinearity-induced conformational instability and dynamics of biopolymers', *Europhysics Letters* **59**(3), 403.

Morgante, A. M., Johansson, M., Aubry, S. & Kopidakis, G. (2002), 'Breather-phonon resonances in finite-size lattices: 'phantom breathers'?', *Journal of Physics A: Mathematical and General* **35**, 4999–5021.

Newton, I. (1687), *Philosophi Naturalis Principia Mathematica*, Vol. II.

Peitgen, H. O., Saupe, D. & Schmitt, K. (1981), 'Nonlinear elliptic boundary value problems versus their finite difference approximations: Numerically irrelevant solutions', *Journal fr die Reine und Angewandte Mathematik* **322**, 74–117.

Peletier, M. A. (2001), 'Sequential buckling: A variational analysis', *SIAM Journal on Mathematical Analysis* **32**, 1142–1168.

Reinhall, P. G., Caughey, T. K. & Storti, D. W. (1989), 'Order and chaos in a discrete duffing oscillator: Implications on numerical integration', *Journal of Applied Mechanics* **56**, 162–167.

Rink, B. (2003), 'Symmetric invariant manifolds in the Fermi-Pasta-Ulam lattice', *Physica D: Nonlinear Phenomena* **175**, 31–42.

Russell, F. M., Zolotaryuk, Y. & Eilbeck, J. C. (1997), 'Moving breathers in a chain of magnetic pendulums', *Physical Review B* **55**(10), 6304–6308.

Saad, Y. (2003), *Iterative Methods for Sparse Linear Systems*, Society for Industrial and Applied Mathematics, Philadelphia, PA, USA. The result is in the exercises at the end of Chapter 4.

Sandstede, B. (1997), 'Instability of localized buckling modes in a one-dimensional strut model', *Philosophical Transactions of the Royal Society of London. Series A: Mathematical, Physical and Engineering Sciences* **355**(1732), 2083–2097.

Scott, A. C. & Macneil, L. (1983), 'Binding energy versus nonlinearity for a "small" stationary soliton', *Physics Letters A* **98**(3), 87–88.

Sievers, A. J. & Takeno, S. (1988), 'Intrinsic localised modes in anharmonic crystals', *Physical Review Letters* **61**(8), 970–973.

Sun, Y. J. & Qin, M. Z. (2003), 'Variational integrators for higher order differential equations', *Journal of Computational Mathematics* **21**(2), 135–144.

Thompson, J. M. T. & Hunt, G. W. (1973), *A General Theory of Elastic Stability*, Wiley, London.

Thompson, J. M. T. & Hunt, G. W. (1984), *Elastic Instability Phenomena*, Wiley-Interscience publication, Wiley.

Thompson, J. M. T. & Stewart, H. B. (2002), *Nonlinear Dynamics and Chaos*, 2nd edn, Wiley.

Tordesillas, A. & Muthuswamy, M. (2009), 'On the modeling of confined buckling of force chains', *Journal of the Mechanics and Physics of Solids* **57**(4), 706 – 727.

Tordesillas, A., Shi, J., Hunt, G. W. & Hammond, J. (2009), Structural evolution of force chains. In progress.

Wadee, M. K. (2005), 'Stability of localized solutions under rigid loading in a heuristic buckling model', *IMA Journal of Applied Mathematics* **0**, 1–11.

Woods, P. D. & Champneys, A. R. (1999), 'Heteroclinic tangles and homoclinic snaking in the unfolding of a degenerate reversible Hamiltonian-Hopf bifurcation', *Physica D: Nonlinear Phenomena* **129**, 147–170.